

Highly-Correlated Electron Behavior in Niobium and Niobium Compound Thin Films

Melissa R. Beebe

Chesapeake, Virginia

Master of Science, College of William & Mary, 2014

Bachelor of Science, Old Dominion University, 2012

Bachelor of Arts, Old Dominion University, 2012

A Dissertation presented to the Graduate Faculty  
of The College of William & Mary in Candidacy for the Degree of  
Doctor of Philosophy

Department of Physics

College of William & Mary

May 2017

©2017  
Melissa R. Beebe  
All rights reserved.

## APPROVAL PAGE

This Dissertation is submitted in partial fulfillment of  
the requirements for the degree of

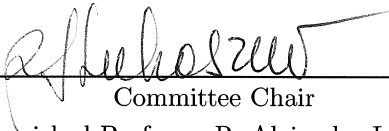
Doctor of Philosophy



---

Melissa R. Beebe

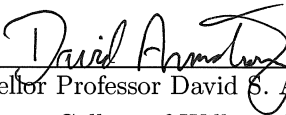
Approved by the Committee, March, 2017



---

Committee Chair

VMEC Distinguished Professor R. Alejandra Lukaszew, Physics  
College of William & Mary



---

Chancellor Professor David S. Armstrong, Physics  
College of William & Mary



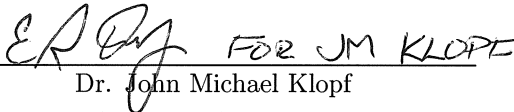
---

Associate Professor Seth A. Aubin, Physics  
College of William & Mary



---

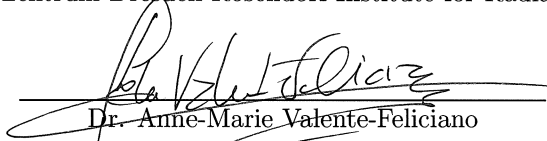
Associate Professor Irina Novikova, Physics  
College of William & Mary



---

Dr. John Michael Klopff

Helmholtz-Zentrum Dresden-Rosendorf Institute for Radiation Physics



---

Dr. Anne-Marie Valente-Feliciano

Jefferson Lab Institute for SRF Science and Technology

## ABSTRACT

Electron correlations are the root of many interesting phenomena in materials, including phase transitions such as superconductivity and insulator-to-metal transitions, which are of great interest both for scientific understanding and for many applications. Such phase transitions can often be tailored in thin films, in which the geometry of the material is limited in one dimension. By studying how the physical structure of a thin film affects its correlated electron response, it is possible to obtain useful insight into both the nature of the electron correlations present in the material and how to control them for various applications. Niobium, an elemental superconductor, has the highest critical temperature and lower critical field of the naturally-occurring superconductors, making it attractive for many applications, particularly in the superconducting radio frequency (SRF) community. Several niobium-based compounds are also superconductors of interest; while the bulk materials are fairly well-understood, there is still a great deal to learn regarding the effects of the microstructure of thin films of these materials on their superconducting properties. Another niobium compound, niobium dioxide, exhibits a phase transition from a room-temperature insulating state to a high-temperature metallic state. Such insulator-to-metal transitions are not well-understood, even in bulk, and there is a great deal of debate over the mechanism that drives them. Experimental studies on niobium dioxide thin films are still somewhat rare and thus have the potential to contribute a great deal to the understanding of the mechanisms behind the transition. This dissertation presents structure-property correlation studies on niobium and niobium compound superconducting thin films such as those discussed above, and also reports on the first experimental studies of the light-induced insulator-to-metal transition in niobium dioxide.

# TABLE OF CONTENTS

Acknowledgments . . . . .	v
Dedication . . . . .	vi
List of Tables . . . . .	vii
List of Figures . . . . .	viii
CHAPTER . . . . .	1
1 Introduction . . . . .	1
1.1 Superconducting Niobium and Niobium Compound Thin Films . . . . .	3
1.1.1 Bulk SRF Cavities . . . . .	3
1.1.2 Thin Film-Coated SRF Cavities . . . . .	5
1.2 Insulator-to-Metal Transition in Niobium Dioxide Thin Films . . . . .	8
1.3 Scope of Dissertation . . . . .	9
2 Electron Behavior in Materials . . . . .	10
2.1 Early Theories of Electrons in Metals . . . . .	10
2.2 Theory of Superconductivity . . . . .	13
2.2.1 London Theory . . . . .	16
2.2.2 London Two-Fluid Model . . . . .	19
2.2.3 BCS Theory . . . . .	21
2.2.4 Ginzburg-Landau Theory . . . . .	23
2.3 Insulator-to-Metal Transitions . . . . .	26
2.3.1 Peierls vs Mott Transitions . . . . .	26

3	Experimental Methods . . . . .	28
3.1	Thin Film Deposition . . . . .	28
3.1.1	Thin Film Structure . . . . .	29
3.1.2	Deposition Methods . . . . .	30
3.2	X-Ray Diffraction and Reflectometry . . . . .	34
3.2.1	X-Ray Diffraction (XRD) . . . . .	35
3.2.2	X-Ray Reflectometry (XRR) . . . . .	38
3.3	SQUID Magnetometry . . . . .	39
3.3.1	$T_C$ Measurements in Superconducting Thin Films . . . . .	41
3.3.2	Critical Field Measurements in Superconducting Thin Films . . . . .	42
3.4	Ultrafast Lasers in Pump-Probe Configuration . . . . .	44
3.4.1	Generation of Ultrafast Pulses . . . . .	44
3.4.2	Experimental Setup . . . . .	46
4	Superconductivity in Niobium and Niobium Compound Thin Films . . . . .	49
4.1	Temperature and Microstructural Effects on the Superconducting Properties of Niobium Thin Films . . . . .	49
4.1.1	Introduction . . . . .	49
4.1.2	Experimental Methods and Results . . . . .	50
4.1.3	Conclusions . . . . .	59
4.2	Correlation Between Microstructure and Electronic Properties of Niobium Thin Films . . . . .	59
4.2.1	Introduction . . . . .	59
4.2.2	Sample Characterization . . . . .	60
4.2.3	Superconducting Gap Calculations . . . . .	60
4.2.4	Structure-Property Correlations . . . . .	61

4.2.5	Conclusions . . . . .	62
4.3	Comparison of $H_{C1}$ Measurements on Superconducting Niobium Thin Films . . . . .	64
4.3.1	Introduction . . . . .	64
4.3.2	Experimental Details and Methods . . . . .	65
4.3.3	Results and Discussion . . . . .	66
4.3.4	Conclusions . . . . .	69
4.4	Stoichiometry and Thickness Dependence of Superconducting Properties of Niobium Nitride Thin Films . . . . .	70
4.4.1	Introduction . . . . .	70
4.4.2	Film Growth and Characterization . . . . .	71
4.4.3	Results and Discussion . . . . .	72
4.4.4	Conclusions . . . . .	76
4.5	Correlation Between Microstructure and Electronic Properties of Niobium Nitride Thin Films . . . . .	77
4.5.1	Introduction . . . . .	77
4.5.2	Four Point Probe Measurements and Calculations . . . . .	77
4.5.3	Results and Discussion . . . . .	78
4.5.4	Conclusions . . . . .	80
5	Insulator-to-Metal Transitions in Niobium Compound Thin Films . . . . .	82
5.1	Optically-Induced Insulator-to-Metal Transition in Niobium Dioxide and Vanadium Dioxide Thin Films . . . . .	82
5.1.1	Introduction . . . . .	82
5.1.2	Experimental Details . . . . .	84
5.1.3	Results and Discussion . . . . .	85

5.1.4	Conclusions . . . . .	92
5.2	Reflection and Transmission of Niobium Dioxide Thin Films During the Insulator-to-Metal Transition . . . . .	94
5.2.1	Introduction . . . . .	94
5.2.2	Results and Discussion . . . . .	94
5.2.3	Conclusions . . . . .	97
6	Conclusion and Outlook . . . . .	98
APPENDIX		
	Pump-Probe Measurement Details . . . . .	100
	Bibliography . . . . .	101

## ACKNOWLEDGMENTS

I would first like to thank my advisor, Ale Lukaszew, for her unfailing support over the last several years. Ale, your drive and determination have made me not just a better scientist but also a better person, and for that I am eternally grateful. While our kind of science *does* actually flourish in a vacuum, scientists do not, so thank you also to many past and present members of the Lukaszew research group - Doug Beringer, Matt Burton, Jason Creeden, Mike Klopff, Zhaozhu Li, Scott Madaras, Jon Skuza, Lei Wang, and Kaida Yang - for your guidance, insight, support, and friendship. I would be remiss to not acknowledge José Riso, whose considerable technical knowledge is certainly missed, but not nearly as much as his presence.

To Dan Salmon, Perry Nerem, Scott Barcus, Kurtis Bartlett, Catie Crain, and Aria Johansen - the hours may have been long, but the company was the best. Thank you as well to the countless other people who have come into my life as a result of physics, and to my friends from outside physics who have always supported me, even when I disappear from their lives for months or years at a time.

Most importantly, I must thank my family, both by blood and by choice, for their constant love and encouragement. Granny and Pop-Pop, the early math lessons on the chalkboard and the flights of imagination in the backyard have stayed with me, long after you were gone. To my father, who didn't so much as bat an eye when told him I wanted to study physics, and to my stepfather, who made us a family again - thank you. And to my mother, who always has my back - I can never thank you enough for everything you have done and continue to do for me. I love you.

This research was made possible by financial support from the Defense Threat Reduction Agency (DTRA) (HDTRA1-10-1-0072), the National Science Foundation (NSF) (DMR-1006013), the Virginia Microelectronics Consortium (VMEC), a Jefferson Science Association (JSA) Graduate Research Fellowship, and a Virginia Space Grant Consortium (VSGC) Graduate Research Fellowship. I am also grateful to the American Vacuum Society Thin Film Division for selecting me as a 2016 Graduate Student Award winner and a 2016 James Harper Award finalist, as well as to the AVS Mid-Atlantic Chapter for several awards and their continuing support over the past three years.

For Pop-Pop, just like I promised.

## LIST OF TABLES

1.1	Bulk superconducting properties of Nb and several Nb-based compounds. . . . .	2
4.1	Substrate and film reflections seen in high-angle $2\theta$ - $\omega$ scans for each sample. . . . .	52
4.2	Lattice parameters and lower critical field values for the Nb films studied here, as well as the corresponding bulk values. . . . .	52
4.3	Zero-field superconducting gap values calculated using Equations 4.4 and 4.3. . . . .	62
4.4	$H_{C1}$ values for Sample 134 as measured at the College of William & Mary. . . . .	67
4.5	$H_{C1}$ values for Sample 124 as measured at the College of William & Mary. . . . .	67
4.6	Thickness, microstructural information, and superconducting properties of the films studied here, as well as the corresponding bulk values. . . . .	73
4.7	Electronic properties for the five films studied here. . . . .	79
5.1	Fit parameters for the scans shown in Figures 5.2, 5.4, and 5.5. The two highlighted columns correspond to the plots shown in Figure 5.6. . . . .	89
5.2	Results of the sensitivity study on Equation 5.1, showing the percent change in the RMS value of the fit after changing the given parameter by $\pm 10\%$ . . . . .	92
.1	Scan parameters for all pump-probe measurements discussed in Chapter 5. . . . .	100

## LIST OF FIGURES

1.1	Simplified picture of the magnetic field geometry in an SRF cavity. . . . .	4
1.2	Representative plot showing cavity Q as a function of accelerating field. . .	6
1.3	Schematic of proposed SIS cavity coating. . . . .	7
2.1	Resistance as a function of temperature for normal and superconducting materials. . . . .	13
2.2	Behavior of an externally-applied magnetic field in a superconductor in the normal state (top) and the superconducting, or Meissner, state (bottom) .	14
2.3	Simple representation of magnetic vortices in a Type II superconductor in the mixed phase. . . . .	15
2.4	Magnetization M of (a) Type I and (b) Type II superconductors plotted against applied field H. . . . .	16
2.5	Representation of the Peierls distortion in a lattice. . . . .	27
3.1	Three possible types of heteroepitaxy: (a) tensile and (b) compressive strain, and (c) relaxed compressive strain. . . . .	30
3.2	Extended structure zone diagram showing the effect of film thickness $t^*$ , growth temperature $T^*$ , and deposition energy $E^*$ on film structure. . . . .	31
3.3	Illustration of a magnetron sputtering system. . . . .	32
3.4	Schematic illustrating a reactive magnetron sputtering process. . . . .	33
3.5	Schematic of the simple X-ray scattering used in XRD. . . . .	35
3.6	Angles accessible with a four-circle goniometer. . . . .	37
3.7	Representative XRR scan. . . . .	38
3.8	DC SQUID. . . . .	40
3.9	Geometry of the SQUID MPMS pickup coils. . . . .	41
3.10	Representative $T_C$ measurement showing sample magnetization as a function of temperature. . . . .	42
3.11	Some possible modes that can exist in a laser cavity. . . . .	45
3.12	Schematic of the ultrafast pump-probe setup used for the reflection studies contained in this dissertation. . . . .	46
4.1	High-angle $2\theta$ - $\omega$ scans for Nb/Cu (top) and Nb/r-Al <sub>2</sub> O <sub>3</sub> (bottom) films. . .	51
4.2	$H_{C1}$ values as a function of temperature for each Nb sample studied. . . .	54

4.3	Correlation between $T_C$ and (a) lattice parameter, (b) average out-of-plane grain size, and (c) mosaicity. . . . .	56
4.4	Correlation between $H_{C1}(0)$ and (a) lattice parameter, (b) average out-of-plane grain size, and (c) mosaicity. . . . .	57
4.5	Correlation between $H_{C2}(0)$ and (a) lattice parameter, (b) average out-of-plane grain size, and (c) mosaicity. . . . .	58
4.6	Correlation between $\Delta(0)$ with zero applied field and (a) lattice parameter, (b) average out-of-plane grain size, and (c) mosaicity. . . . .	63
4.7	M-H curves for (a) Sample 134 and (b) Sample 124 as measured at the College of William & Mary. . . . .	66
4.8	Comparison of VSM/SQUID data from the University of Geneva (thick solid line) and SQUID data via the (a) traditional M-H method (solid dots) and (b) trapped field method (right axis, circles with centered dots) from the College of William & Mary. . . . .	69
4.9	High-angle $2\theta$ - $\omega$ scan for the 80 nm NbN sample on MgO(100). . . . .	72
4.10	(a) Calculated predicted lower critical field ( $H_{C1}$ ) enhancement for NbN thin films, with a coherence length of $\xi = 4$ nm. (b) Actual $H_{C1}$ values for the films considered here, with the theoretical curve shifted to show that the films fit the trend. . . . .	74
4.11	Critical temperature, $T_C$ , as a function of (a) lattice constant and (b) thickness. . . . .	75
4.12	(a) Critical field, $H_{C1}$ and (b) critical temperature, $T_C$ as a function of grain size. . . . .	76
4.13	Sheet resistance $R_S$ of the five films studied here as a function of thickness. The light gray dashed line is the $H_{C1}$ enhancement shown in Figure 4.10, shifted to indicate the similar trend appearing here. . . . .	79
4.14	Conductivity $\sigma$ of the five films studied as a function of (a) grain size and (b) mosaicity. . . . .	80
5.1	High-angle $2\theta$ - $\omega$ scans of the NbO <sub>2</sub> (top) and VO <sub>2</sub> (bottom) samples studied. . . . .	84
5.2	Pump-probe measurements and fits for the lowest fluence at which the IMT was seen in each material. . . . .	86
5.3	Pump-probe measurements at a pump fluence of 70.0 mJ/cm <sup>2</sup> , when the structural transition begins in the VO <sub>2</sub> film, causing the signal to become larger than that of the NbO <sub>2</sub> film. . . . .	87
5.4	Scans of NbO <sub>2</sub> with pump fluences ranging from 8.8 mJ/cm <sup>2</sup> to 422 mJ/cm <sup>2</sup> . . . . .	88
5.5	Scan of fully-transitioned VO <sub>2</sub> . . . . .	89

5.6	Normalized scans of NbO <sub>2</sub> and VO <sub>2</sub> at 422 mJ/cm <sup>2</sup> , the highest fluence achieved without damaging the samples. . . . .	90
5.7	Scans of NbO <sub>2</sub> and VO <sub>2</sub> at the highest fluence achieved without sample damage. . . . .	95
5.8	Scans of NbO <sub>2</sub> in reflection (teal) and transmission (black) geometries at two fluences, (a) 2.2 mJ/cm <sup>2</sup> and (b) 35 mJ/cm <sup>2</sup> . . . . .	95
5.9	Scans of NbO <sub>2</sub> at the highest fluence at which the transition was observed in both reflection and transmission geometries. . . . .	96

# CHAPTER 1

## Introduction

Electron interactions are responsible for a number of interesting behaviors in materials, including both conventional and high-temperature superconductivity, magnetism, and insulator-to-metal transitions, several of which manifest themselves in niobium and various of its compounds. Niobium (Nb) itself is a Type II superconductor, with the highest critical temperature ( $T_C$ ) and the highest lower critical field ( $H_{C1}$ ) of the naturally-occurring elemental superconductors [1]; many niobium-based compounds also exhibit Type II superconductivity [2], including (but certainly not limited to) niobium nitride (NbN), niobium titanium (NbTi), niobium titanium nitride (NbTiN), niobium tin (Nb<sub>3</sub>Sn), and, interestingly, niobium monoxide (NbO) [3, 4]. Various properties of these superconductors, which will be defined in Chapter 2, are summarized in Table 1.1; several of these materials will be discussed in more detail in Chapter 4.

NbO is only one of several oxides that elemental Nb may form. The most common of these, niobium pentoxide (Nb<sub>2</sub>O<sub>5</sub>), is a very good dielectric and is often used in capacitors [9], but a less common niobium oxide is of potentially even greater interest. Niobium dioxide (NbO<sub>2</sub>) is what is known as a *highly correlated material*; in such materials, the

TABLE 1.1: Bulk superconducting properties of Nb and several Nb-based compounds. Values listed are taken from [2, 3, 5–10]; those left blank have not been reported.

Material	$T_C$ K	$H_{C1}(0)$ Oe	$H_C$ Oe	$H_{sh}$ Oe	$H_{C2}(0)$ Oe	$\lambda_L$ nm	$\xi$ nm
Nb	9.23	1800	2000	2100	4000	50	22
NbN	16.2	200	2300	1600	150,000	200	4
NbTi	9.5		148,000				
NbTiN	17.5	300			150,000	151	
Nb <sub>3</sub> Sn	18	500	5400	4100	300,000	111	4.2
NbO	1.6	140					

standard non-interacting approaches (e.g. the free electron approximation or mean field theory) do not adequately describe the properties of the materials, which are determined by electron interactions. In particular, NbO<sub>2</sub> is one of several highly correlated materials that exhibits an insulator-to-metal transition (IMT), with changes to both the electronic and the crystal lattice structure. The most extensively studied<sup>1</sup> of these, vanadium dioxide (VO<sub>2</sub>), will often be used as a point of comparison in this dissertation, as the two materials are structurally quite similar and display many of the same properties [11]. The most interesting difference, though, is the temperature at which the IMT occurs: in bulk VO<sub>2</sub>, the transition occurs at 340 K, while in NbO<sub>2</sub> it does not occur until 1080 K, possibly indicating other advantageous differences from VO<sub>2</sub> [11].

While all of the above information is given for bulk materials, the work presented in this dissertation deals with thin films. The simplest definition of a thin film is a material that is constrained in one dimension; this physical constraint often leads to unique properties, and the process by which a thin film is created provides the ability to modify many of these properties. Thin films are therefore useful for understanding how a material's

<sup>1</sup>A Google Scholar search for “VO<sub>2</sub>” and “vanadium dioxide” returns 8,820 and 7,780 articles, respectively, from 2016 alone.

structure affects its properties, and in many cases are of great interest for application. The following sections discuss such scientific and application-based interest in Nb and several Nb compound thin films, both those that exhibit superconductivity and those that undergo an insulator-to-metal transition.

## 1.1 Superconducting Niobium and Niobium Compound Thin Films

Nb and related thin films are of great interest for many applications, particularly in the superconducting radio frequency (SRF) community for use in particle accelerators [12–15]. In order to understand the interest in such thin films, however, an understanding of the current state of SRF cavity technology must be developed.

Before the 1960s, early particle accelerators used radio frequency (RF) cavities made of a conventional conductor, often copper (Cu) [16]. While such cavities have good thermal conductivity - which is important to dissipate the heat generated by the RF power in the cavity before it can damage the cavity interior - they also have a not-insignificant surface resistance, which contributes to heating effects. Such cavities were cooled with water, but as liquid helium and liquid helium-cooled superconductors became more commonplace, research into SRF cavities began. The first SRF cavity was a Cu cavity electroplated with superconducting lead ( $T_C = 7.19$  K); now, bulk Nb is the preferred material [16].

### 1.1.1 Bulk SRF Cavities

The primary advantage of an SRF cavity over a traditional conducting cavity is a dramatically improved *quality (Q) factor*. The Q factor, a common method for quantifying the quality of an RF cavity, is the ratio of energy stored in the cavity to the energy lost

in one RF period, and is inversely proportional to the surface resistance of the cavity material. Traditional Cu cavities have a Q value of  $\sim 10^4$ ; the RF surface resistance of a superconducting cavity is on the order of 5 orders of magnitude lower than that of a conventional conductor, resulting in typical Q factors of  $\sim 10^9$  for SRF cavities<sup>2</sup> [16]. This results in more RF power to the accelerating field of an SRF cavity, leading to increased performance over a traditional RF cavity.

A simplified schematic of the magnetic field geometry inside an SRF cavity is shown in Figure 1.1. In the primary accelerating mode ( $TM_{010}$ ), the magnetic field is parallel to and at its maximum at the interior cavity surface. Therefore, the fundamental limitation on SRF cavities is determined by the superheating field,  $H_{sh}$ , of the surface material used. This superheating field limit in turn determines the maximum accelerating field gradient that the cavity can sustain.

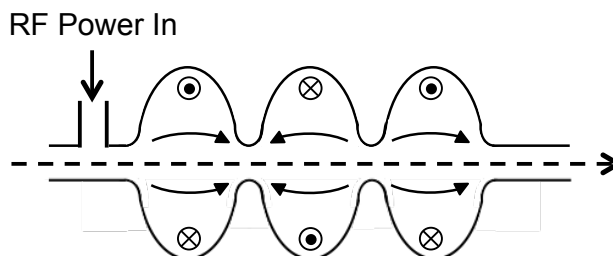


FIG. 1.1: Simplified picture of the magnetic field geometry in an SRF cavity. Arrows represent the direction of the electric field, while  $\otimes$  and  $\odot$  represent the direction of the magnetic field (into and out of the plane depicted, respectively). The dotted line through the center of the cavity is the path traveled by the particles being accelerated.

Nb is an excellent material for use in bulk SRF cavities - it is fairly abundant, and as noted above, it has the highest critical temperature ( $T_C = 9.23$  K) and the highest lower critical field ( $H_{C1} = 1800$  Oe) of the elemental superconductors. Additionally, Nb is com-

<sup>2</sup>Although not used in accelerators, cavities with a Q factor greater than  $10^{11}$  have been reported [17].

paratively easy to refine and machine, although the preparation of SRF cavities requires a highly specialized process, which is thoroughly explained in Chapter 6 of Reference [16]. The SRF community has steadily improved the quality of bulk Nb cavities, which are now very near the theoretical limit of  $E_{acc} \approx 50$  MV/m [18]. Because this field gradient can no longer be significantly increased by further improvements in bulk Nb cavities, the next generation of SRF cavities being considered use thin film coatings on the interior surface of a cavity. There are two main proposed schemes for such coatings, both discussed below.

### 1.1.2 Thin Film-Coated SRF Cavities

The first coating method being considered is to use a single thick layer ( $\sim 1 \mu\text{m}$ ) of a superconducting film over a traditional Cu RF cavity. This scheme would allow accelerators to take advantage of copper’s good thermal conductivity while still utilizing the benefits of a superconducting inner surface in the cavity, and also reduces the material cost of cavity production [16, 19]. Using a superconducting coating also provides greater freedom in the choice of superconductor: Nb can certainly be used, but other superconductors with higher  $T_C$  that are not necessarily feasible in bulk may be used as well [19]. Work on coated cavities has been ongoing since 1980, when CERN first sputter-coated a Cu cavity with Nb; while great improvements have been made since then, all coated cavities have displayed what is termed a *Q-slope* [19]. As depicted in Figure 1.2, the Q-slope is the strong field dependence of a cavity’s Q factor, which limits cavity performance at high fields. Another issue with thin film coatings is surface quality: sharp surface features or surface contamination can act as RF antennae, creating thermal effects that can ultimately lead to quenching (sudden, complete expulsion from the superconducting state) [16].

A second coating method, proposed in 2006, uses stacks of alternating superconducting-insulating-superconducting (SIS) thin films to “shield” a bulk Nb cavity, effectively increas-

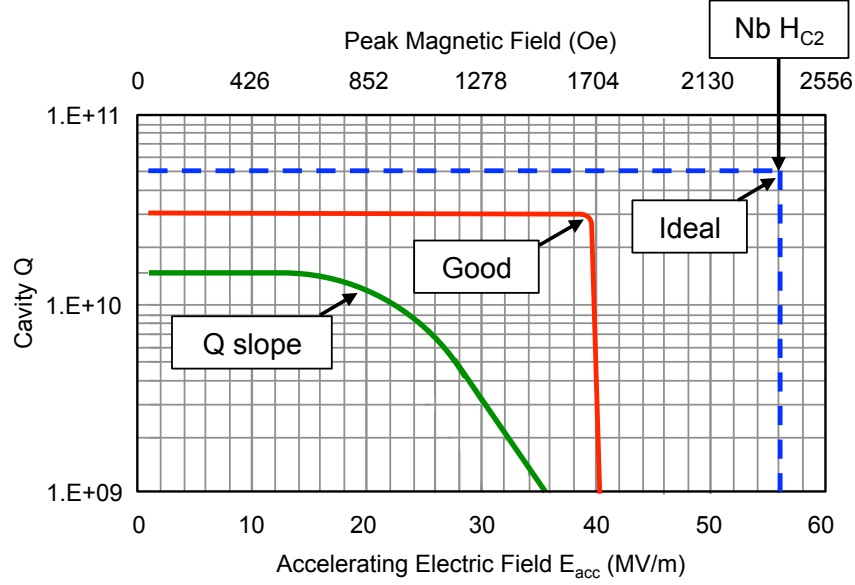


FIG. 1.2: Representative plot showing cavity  $Q$  as a function of accelerating field.

ing the maximum field gradient that the cavity can sustain, and theoretically flattening the  $Q$ -slope of the cavity, thereby lessening the drop in cavity performance at high fields [20]. This SIS model, a schematic of which is shown in Figure 1.3, uses thin layers of a superconducting thin film with  $T_C$  and  $H_{C1}$  higher than that of Nb to attenuate the magnetic field before it reaches the bulk cavity; the even thinner insulating layers ( $\sim 2$  nm) effectively pin any magnetic vortices that form in the superconducting layer above them, preventing that magnetic flux from penetrating the next superconducting layer. The thickness of the superconducting layers is determined by the *London penetration depth*,  $\lambda_L$ , of the material; as discussed further in Chapters 2 and 4, superconducting thin films that are thinner than this fundamental material property exhibit an enhancement in their lower critical field when in a parallel field geometry, such as in an SRF cavity [20].

Several of the materials listed in Table 1.1, such as NbN, NbTiN, and Nb<sub>3</sub>Sn, are

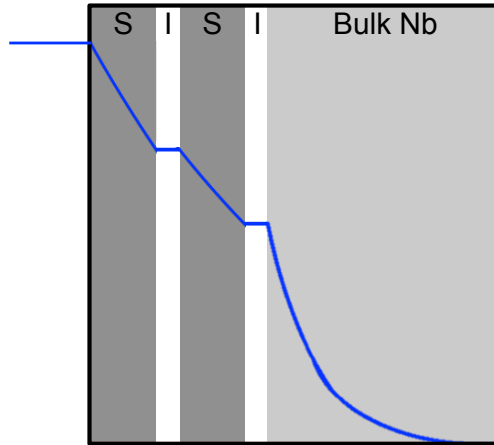


FIG. 1.3: Schematic of proposed SIS cavity coating. The solid blue line represents the magnetic field strength as it passes from the interior of the SRF cavity, through the SIS structures, and into the bulk SRF cavity.

possible candidates for the superconducting layers, as are non-Nb-based superconductors, such as  $\text{MgB}_2$ . The enhancement in  $H_{C1}$  necessary for the SIS model has been experimentally seen in single-layer  $\text{MgB}_2$  films [21], and  $\text{NbN}/\text{MgO}/\text{Nb}/\text{MgO}$  multilayers have been seen to provide some magnetic shielding beyond the  $H_{C1}$  of Nb [22]. As discussed above, controlling the surface of the film coating is crucial for good SRF performance; when dealing with multilayered structures, however, this becomes more of a challenge, as the underlying layers influence the surface morphology of the top layer [22].

Both methods described here require an understanding of how the surface morphology and microstructure of thin films affects their superconducting performance, and then careful control of the microstructure during the growth process. A great deal of information can be obtained from studying the structure of small samples and their resulting properties, which can then be translated to full cavity coating deposition systems. In many cases, such systems are also capable of growing *witness samples*, which are a more convenient size and geometry for characterization, to allow confirmation of the microstructure and superconducting performance from a given set of deposition conditions.

## 1.2 Insulator-to-Metal Transition in Niobium Dioxide Thin Films

Despite their name, many transition-metal oxides (so named due to the metals' position in the periodic table) are in fact insulators at room temperature [23]; such unusual behavior was attributed to the strong Coulomb repulsion present in the partially-filled  $d$  band of the oxides [24]. This strong correlation between electrons gave rise to the name "highly correlated materials" now used to describe such materials and many others. It was later shown that many of these oxides exhibit an insulator-to-metal transition (IMT) that can be induced by heat, voltage, pressure, or ultrashort light pulses [25–27]. Of these, vanadium dioxide ( $\text{VO}_2$ ) has long been the material of greatest interest - the relatively low transition temperature (340 K) makes it easy to transition for experimental studies, as well as very attractive for a number of applications, including ultrafast switches and sensors [28–30].

Despite decades of research into the IMT of  $\text{VO}_2$ , there remains a great deal of debate over which mechanism - structural (Peierls) or electronic (Mott) - actually drives the transition [31, 32]. Despite time resolution on the time scale of electron interactions (as compared to the longer phonon interactions that are part of the structural transformation), even ultrafast pump-probe studies - first attempted in 1971 [26] and continuing to the present day [33–40] - have failed to definitively resolve this debate. Theoretical investigation into  $\text{VO}_2$  has also been unable to identify the driving mechanism of the IMT [41], leading to recent interest in related materials, such as  $\text{NbO}_2$  [27, 31].

Based on Nb, which is a  $4d$  transition metal rather than a  $3d$  transition metal like V,  $\text{NbO}_2$  should have slightly weaker electron correlations than  $\text{VO}_2$ , making theoretical calculations comparatively more manageable [27]. Further, the much higher transition

temperature of NbO<sub>2</sub> (1080 K) may allow for separate resolution of the electronic response and the structural (often thermally-induced) response in ultrafast studies of the IMT. This higher transition temperature is also potentially useful for applications in which device operating temperatures are higher than the transition temperature of VO<sub>2</sub> [42]. Despite the advantages to studying NbO<sub>2</sub>, however, there are only a few studies available in literature [9, 42–46], and, until recently [11], no sub-picosecond-resolution investigations; there is therefore a great deal of information that could be obtained through further experimental work.

### 1.3 Scope of Dissertation

This dissertation presents experimental studies on the effects of electron correlations and the resulting phase transitions - from the normal to the superconducting or from the low-temperature insulating to the high-temperature metallic state - in Nb and Nb compound thin films. Chapter 2 discusses electron behavior in materials and the resulting phase transitions of interest, while Chapter 3 introduces the primary experimental methods used to grow and characterize the thin films studied; later chapters focus on each individual type of phase transition. Chapter 4 presents results from structure-property correlation studies on several series of superconducting thin films, two of which have already been published in peer-reviewed journals [5, 15]. Chapter 5 discusses insulator-to-metal transitions and presents studies - the first of their kind - on the ultrafast light-induced transition in NbO<sub>2</sub> thin films, as well as comparisons to VO<sub>2</sub>. Additional work related to the superconducting thin films can be found in References [47] and [48], while Reference [49] provides an in-depth study of the light-induced IMT in VO<sub>2</sub> and suggests a direction for continuing the work presented here on NbO<sub>2</sub>.

# CHAPTER 2

## Electron Behavior in Materials

### 2.1 Early Theories of Electrons in Metals

Prior to the turn of the 20th century, there was no good explanation for the properties of solid materials. The discovery of the electron by J. J. Thomson in 1897 [50], though, initiated the development of increasingly accurate theoretical descriptions of solids.

In 1900, P. Drude adapted the highly-successful kinetic theory of gases to metals with one necessary change [51–53]. In the existing theory, all of the molecules were assumed to be identical; with the discovery of the electron, this was clearly not the case in metals. Drude assumed metals to be comprised of two kinds of particles - the negatively-charged electrons and some other type of particle with the positive charge needed to cancel the electron charge and make the metal electrically neutral [51]. He further assumed that the positive charges were stationary, predictive of the crystal lattices first seen in 1913 by W. H. and W. L. Bragg [54]; the electrons could therefore be treated as a free electron gas [51].

In the Drude model, electrons are treated as largely non-interacting, both with other

electrons and with the positively charged ions. The only time the electrons interact with another particle is when they collide. As in the kinetic gas theory, electron collisions are instantaneous, but contrary to collisions in a gas, the electrons do not collide with like particles; rather, they only interact with the positive ions in the metal [51].

Even this highly simplistic model shows good agreement with many experimental results, particularly for DC and AC electrical conductivity, among other material properties<sup>1</sup>. The model fails, however, to handle some thermodynamic properties of metals, especially the specific heat, which caused concern about the accuracy of the Drude model for a quarter of a century [51]; it would require quantum mechanics and resulting concepts to resolve this issue.

The Pauli exclusion principle - a purely quantum mechanical concept - was proposed in 1925 to account for electron behavior that was not yet understood [55]. This new classification of electrons as fermions led, three years later, to A. Sommerfeld's application of the resulting Fermi-Dirac statistics to Drude's free electron model (which uses the Maxwell-Boltzmann statistics that worked so well for the kinetic theory of gases) for metals [56]. This resolved the worst of the thermal problems from the Drude model, but there were still a number of properties of metals that free electron models could not account for, including the temperature-dependence of DC conductivity and why some materials are metals and others are not [51].

The following year, in an attempt to answer these questions, F. Bloch began studying the motion of electrons in a periodic crystal lattice, such as those found in metallic solids [57], with a periodicity of  $\mathbf{R}$ , i.e.

$$\mathbf{r} + \mathbf{R} = \mathbf{r} . \tag{2.1}$$

---

<sup>1</sup>While full derivation of all material properties described by the models discussed here is far too lengthy for this dissertation, a partial derivation of concepts relevant to the work presented will be included in the following sections. Interested readers may consult [51] or a similar text for other derivations.

Such a lattice can be treated as a periodic potential

$$U(\mathbf{r} + \mathbf{R}) = U(\mathbf{r}), \quad (2.2)$$

and Bloch considered each electron in a material as obeying a single-electron Schrödinger equation for such a potential [51]. Bloch's Theorem states that the solutions to this equation - the eigenstates of the electron - can be chosen to have the same periodicity as the underlying lattice,

$$\psi_{n\mathbf{k}}(\mathbf{r}) = e^{i\mathbf{k}\cdot\mathbf{r}} u_{n\mathbf{k}}(\mathbf{r}), \quad u_{n\mathbf{k}}(\mathbf{r} + \mathbf{R}) = u_{n\mathbf{k}}(\mathbf{r}), \quad (2.3)$$

where  $\mathbf{k}$  is the wave vector of the electron. Substituting this wavefunction into the Schrödinger equation yields a set of discrete energies,  $\epsilon_{n\mathbf{k}}$ ; the energies for a given  $n$  are called the *bands* of the material [51].

The Bloch treatment of electrons accounts for the temperature-dependence of DC conductivity that the Sommerfeld theory could not explain [58], and also explains the difference between metals and non-metals [59]. In metals, some electronic bands are only partially filled, while in non-metals, all bands are either completely filled or completely empty. This is the root of the *band gap* in insulators - there is some energy gap between the filled and unfilled energy bands; in metals, the partially-filled bands overlap, so there is no gap in the energy levels [51]. The difference between the highest and lowest occupied energy levels or quantum states is called the *Fermi energy*; this energy level lies in the band gap of insulators, but is within the overlapping bands in a metal [51].

It is important to note here that Bloch electrons are not completely independent, although their wavefunctions are. In this approximation, the major interactions between electrons are absorbed into the choice of periodic potential, implying that the electrons

themselves exhibit some sort of periodic behavior [51]. This then gives the first hint at the importance of electron correlations to material properties, which will be discussed in the following sections in greater detail for two specific types of materials: conventional superconductors, and those materials that exhibit an insulator-to-metal transition. While the theory and understanding of these classes of materials proceeded somewhat in parallel, the discovery of superconductivity occurred first, making it a natural starting point for the following discussions.

## 2.2 Theory of Superconductivity

As stated above, the conductivity (and therefore the resistivity) of a metal displays some temperature dependence; as shown in Figure 2.1, a normal metal will always have some inherent resistance, even at absolute zero. Superconductors, however, display a sharp decrease in resistance at some critical temperature  $T_C$ , below which the material has no resistance (i.e. infinite, “super” conductance). This phenomenon, first observed by H. K. Onnes in 1911 [60], did not match any known theory at the time.

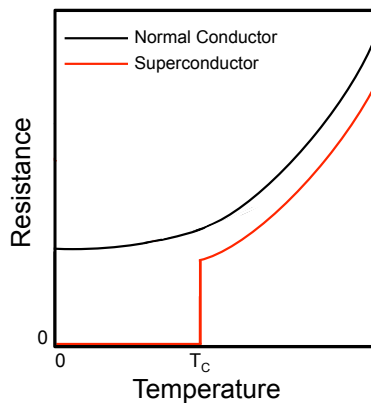


FIG. 2.1: Resistance as a function of temperature for normal and superconducting materials.

Two decades later, in 1933, W. Meissner and R. Ochensfeld observed the magnetic field of superconductors and found that, as the material transitioned from the normal state to the superconducting state, any applied magnetic field was expelled [61]. This behavior, shown in Figure 2.2, is now known as the Meissner effect and indicates that superconductors are not simply ideal conductors; as such, their magnetic response is not completely described by classical electrodynamics.

In the simplest case, when a superconductor is in the superconducting state and in the presence of an applied magnetic field, it creates surface currents and thus a magnetic field to cancel the applied field. This continues as the applied field increases up to some critical field value  $H_C$ .<sup>2</sup> Above this point, however, the material returns to the normal state, despite still being at a temperature below the superconducting transition temperature  $T_C$  [16].

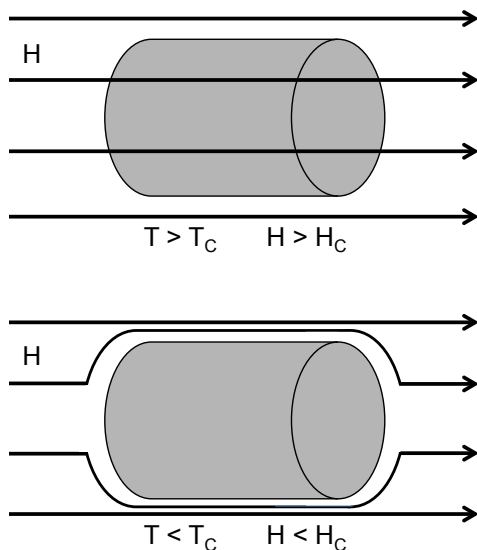


FIG. 2.2: Behavior of an externally-applied magnetic field in a superconductor in the normal state (top) and the superconducting, or Meissner, state (bottom) .

<sup>2</sup> $H$  and  $B = \mu H$  are used somewhat interchangeably - both here and in the greater superconductivity community - as superconductors are treated as perfect diamagnets, i.e.  $|H| = |B|$ .

In reality, superconductors respond in one of two ways to an externally-applied magnetic field, leading to a practical way of classifying a superconducting material. Superconductors that behave as described above - a linear increase in magnetic response to counter the applied field (Meissner state), and then a sharp return to the normal state above some critical field  $H_C$  - are classified as Type I superconductors [16]. Type II superconductors, such as the materials discussed in this dissertation, display a so-called “mixed phase” between the Meissner and normal states. In a Type II superconductor, the magnetic behavior of the material at low fields is the same as that of a Type I superconductor; this linear response continues until the externally-applied magnetic field reaches the lower critical field value,  $H_{C1}$  [16]. As the applied magnetic field is increased above  $H_{C1}$ , magnetic flux begins to penetrate the material, forming magnetic vortices (see Figure 2.3) [16]. This

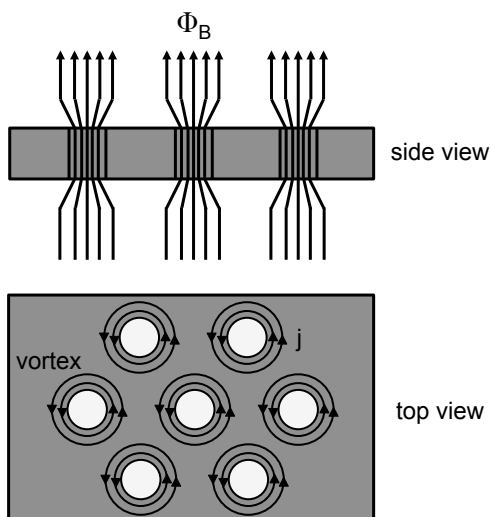


FIG. 2.3: Simple representation of magnetic vortices in a Type II superconductor in the mixed phase.

mixed phase persists, with increased flux penetration as the applied field increases, until the upper critical field  $H_{C2}$  is reached. Above this field, the material returns to the normal

state<sup>3</sup> [16]. The behavior of both types of superconductors is shown in Figure 2.4.

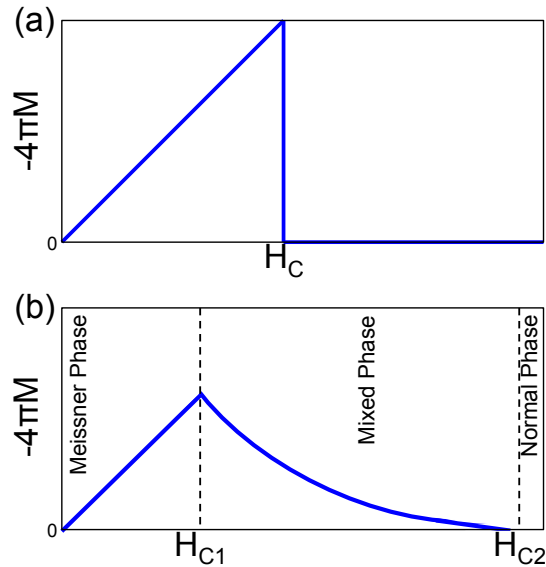


FIG. 2.4: Magnetization  $M$  of (a) Type I and (b) Type II superconductors plotted against applied field  $H$ .

### 2.2.1 London Theory

Two years after the discovery of the Meissner effect, a mathematical description of superconductivity was developed by F. and H. London. Their equations, now known as the London equations, give a classically electromagnetic description of the two superconducting phenomena observed to that point - zero DC resistance and the Meissner effect. To do this, they considered the superconducting charge carriers to be free charges - analogous to electrons in a perfect conductor - that experience uniform Lorentz forces when in the presence of externally-applied electric and magnetic fields [51].

<sup>3</sup>It is important to note that Type II superconductors do have a critical field ( $H_C$ ) value, as shown in Table 1.1, associated with them. This value is often used to compare between superconductors, but does not correspond directly to any change in the material's magnetic response.

As discussed in Section 2.1, the Drude model of free electrons successfully predicts the DC conductivity for perfect conductors. In such a material, electrons in an electric field  $\mathbf{E}$  see an acceleration of

$$m_e \frac{\partial \mathbf{v}}{\partial t} = -e\mathbf{E} \quad (2.4)$$

and have a current density of

$$\mathbf{j} = -nev, \quad (2.5)$$

where  $m_e$  is the mass of a single electron,  $\mathbf{v}$  is the velocity of the electrons,  $e$  is the electronic charge, and  $n$  is the number of electrons [51]. Writing the superconducting current density as

$$\mathbf{j}_s = -n_s e\mathbf{v} \quad (2.6)$$

thus gives an equation for the infinite conductivity seen in superconductors, which is known as the first London equation [51]:

$$\frac{\partial \mathbf{j}_s}{\partial t} = \frac{n_s e^2}{m_e} \mathbf{E}. \quad (2.7)$$

Using the Maxwell-Faraday equation

$$\nabla \times \mathbf{E} = -\frac{\partial \mathbf{B}}{\partial t} \quad (2.8)$$

relates the current density and magnetic field [51]:

$$\frac{\partial}{\partial t} \left( \nabla \times \mathbf{j}_s + \frac{n_s e^2}{m_e} \mathbf{B} \right) = 0. \quad (2.9)$$

While this holds for an perfect conductor, it is not restrictive enough to explain the Meissner effect seen in superconductors. To do so, it is required that

$$\nabla \times \mathbf{j}_s + \frac{n_s e^2}{m_e} \mathbf{B} = 0, \quad (2.10)$$

rather than simply time-independent; this restriction is the second London equation [51].

To determine the magnetic field and current density inside a superconductor, one can apply Ampère's Law,

$$\nabla \times \mathbf{B} = \mu_0 \mathbf{j}_s, \quad (2.11)$$

which yields

$$\nabla^2 \mathbf{B} = \frac{1}{\lambda_L^2} \mathbf{B} \quad \text{and} \quad \nabla^2 \mathbf{j}_s = \frac{1}{\lambda_L^2} \mathbf{j}_s, \quad (2.12)$$

respectively, where

$$\lambda_L \equiv \sqrt{\frac{m_e}{\mu_0 n_s e^2}} \quad (2.13)$$

is the *London penetration depth*, which is the depth from the surface of a superconductor in which superconducting currents and magnetic fields exist [16, 51].

These equations can be solved for the simple case in which the surface of a superconductor is a plane perpendicular to the  $x$ -axis and the magnetic field points in the  $z$  direction

[16]. In this geometry, the magnetic field and the superconducting current density are

$$B_z = B_0 e^{-\frac{x}{\lambda_L}} \quad (2.14)$$

and

$$j_y = -\frac{1}{\lambda_L} B_0 e^{-\frac{x}{\lambda_L}}. \quad (2.15)$$

This is particularly interesting in the case of thin films, as the London penetration depth in common superconductors is typically a few tens to a few hundreds of nanometers [3, 62]. If a superconducting thin film is thinner than its London penetration depth,  $x$  is necessarily smaller than  $\lambda_L$ ; Equation 2.14 thus predicts a magnetic field that is enhanced when compared to that of the magnetic field in a bulk superconductor.

### 2.2.2 London Two-Fluid Model

Because thin films are often dominated by surface effects, it is important to understand the surface resistance  $R_{surf}$  of a superconducting film; this is particularly true for the superconducting radio frequency (SRF) cavity applications discussed in Chapter 1, in which  $R_{surf}$  partially determines the quality factor of the cavity in question [16].

To determine the surface resistance of a superconductor, one must consider the two different fluids of charge carriers, the normal-state electrons and the superconducting electrons. In the presence of a time-dependent electric field  $\mathbf{E} = E_0 e^{i\omega t}$ , the normal-state electrons have a current density of

$$j_n = \sigma_n E_0 e^{i\omega t}, \quad (2.16)$$

where  $\sigma_n$  is the normal-state conductivity of the material [16].

If we assume the superconducting current in the presence of a time-dependent electric field is also time-dependent, i.e.  $j_s = j_{s0}e^{i\omega t}$ , we can apply the first London equation (Equation 2.7) to obtain a parallel expression for the superconducting current density:

$$j_s = -i\sigma_s E_0 e^{i\omega t}, \quad (2.17)$$

where

$$\sigma_s = \frac{1}{\mu_0 \lambda_L^2 \omega} = \frac{n_s e^2}{m_e \omega} \quad (2.18)$$

is the superconducting “conductivity” [16].

The total current density inside a superconductor is thus given by

$$j = j_n + j_s = \sigma E_0 e^{i\omega t} \quad (2.19)$$

with complex conductivity

$$\sigma = \sigma_n - i\sigma_s. \quad (2.20)$$

The surface impedance of a normal conductor is given by  $Z = 1/(\delta\sigma_n)$ , where  $\delta$  is the skin depth; analogously, the surface impedance of a superconductor is given by

$$Z_{surf} = \frac{1}{\lambda_L(\sigma_n - i\sigma_s)}. \quad (2.21)$$

The surface resistance  $R_{surf}$  is the real part of the complex surface impedance,

$$R_{surf} = \frac{1}{\lambda_L} \frac{\sigma_n}{\sigma_n^2 + \sigma_s^2}, \quad (2.22)$$

but we know that the conductivity of the superconducting electrons is much higher than that of the normal-state electrons, i.e.  $\sigma_s \gg \sigma_n$ , which leads to the approximation

$$R_{surf} \approx \frac{1}{\lambda_L} \frac{\sigma_n}{\sigma_s^2}, \quad (2.23)$$

which in turn leads to

$$R_{surf} = \frac{1}{2} \sigma_n \omega^2 \mu_0^2 \lambda_L^3 \quad (2.24)$$

and the somewhat counter-intuitive result that the surface resistance of a superconductor is proportional to the *normal-state* conductivity of the material [16].

### 2.2.3 BCS Theory

While the London description of superconductivity describes the macroscopic behavior of superconductors in terms of classical electromagnetism, it does not address the quantum mechanical behavior of superconductors, nor does it explain the origin of superconductivity. Such a description of superconductivity would not arise until 1957, some 22 years after the London theory, when J. Barden, L. N. Cooper, and J. R. Schrieffer developed the microscopic theory of superconductivity now known as BCS theory [63, 64]. This theory proposes that superconductivity is the result of the pairing of electrons near the Fermi surface (the momentum-space equivalent to the Fermi energy) into *Cooper pairs*<sup>4</sup>. Such

---

<sup>4</sup>It is worth noting that the London penetration depth (Equation 2.13) is invariant under Cooper pairing, i.e. under  $n_s \rightarrow n_s/2$  and  $m_e \rightarrow 2m_e$ , thus the two formulations are not contradictory; they in

pairing of course requires a net attraction between two electrons, which seems to directly contradict the basics of electrostatics; the motion of ions in a lattice (which is required to explain the isotope effect in elements) can, however, effectively screen out the Coulomb repulsion between electrons, leading to such a net attraction. In BCS theory, there is no minimum requirement for this attractive strength - any arbitrarily small attraction between two electrons is enough to cause the pairing. Qualitatively, the formation of a Cooper pair can be visualized by imagining the motion of an electron through a superconductor. As the electron moves, it slightly attracts the lattice, creating a very small region of net positive charge. This positively-charged portion of the lattice then attracts the second electron, and the lattice distortion creates a phonon, which mediates the pairing between the two electrons [51].

When the electrons pair off into the quasi-bosonic Cooper pairs, they occupy the same quantum state. This opens a temperature-dependent energy gap  $2\Delta$  around the Fermi energy; at 0 K, it is given by [51]

$$\Delta(0) = 1.76k_B T_C . \quad (2.25)$$

It is also possible to approximate the superconducting energy gap at temperatures close to the critical temperature  $T_C$  by

$$\frac{\Delta(T)}{\Delta(0)} = \left(1 - \frac{T}{T_C}\right) , \quad T \approx T_C . \quad (2.26)$$

BCS theory also gives a similar approximation for the relationship of the critical field (or, in Type II superconductors, the lower critical field) at some temperature  $T$  to the 0 K

---

fact complement each other quite well.

critical field [51]:

$$\frac{H_C(T)}{H_C(0)} \approx 1 - \left(\frac{T}{T_C}\right)^2. \quad (2.27)$$

## 2.2.4 Ginzburg-Landau Theory

Such a quantum mechanical treatment of superconductivity leads once again to the question of how to classify superconductors. The Type I/Type II classification arose from the classical electromagnetic response of the materials, but is there such a distinction in BCS theory? The answer to this lies in the Ginzburg-Landau theory, which uses two characteristic superconducting lengths to distinguish between the two types of magnetic responses seen in superconductors. The Ginzburg-Landau parameter,  $\kappa$ , is defined to be

$$\kappa = \frac{\lambda_L}{\xi}, \quad (2.28)$$

where  $\lambda_L$  is the London penetration depth (which, as noted previously, is invariant under the transformation from London to BCS theories) and  $\xi$  is the *coherence length*, which, in BCS theory, is given by<sup>5</sup>

$$\xi = \frac{\hbar v_F}{\pi \Delta}, \quad (2.29)$$

where  $v_F$  is the Fermi velocity of the electrons in a Cooper pair [51]. This coherence length is the “size” of the Cooper pairs in a superconductor, i.e. the length over which the electron pairing is coherent. In Type I superconductors, the coherence length is larger than the London penetration depth, such that  $\kappa > 1/\sqrt{2}$ , while in Type II superconductors, the reverse is true, such that  $\kappa < 1/\sqrt{2}$  [51].

---

<sup>5</sup>For temperatures near  $T_C$ , the coherence length can also be approximated by  $\xi \propto (1 - T/T_C)^{-1}$ .

A further addition of Ginzburg-Landau theory to BCS theory is the quantization of magnetic flux. The Ginzburg-Landau theory requires that the current in a superconductor follow the quantum mechanical formulation of current due to a particle with mass  $2m_e$  and charge  $2e$ , i.e. a Cooper pair [51]. Applying Stokes' theorem to such a current ultimately leads to the conclusion that magnetic flux in a superconductor must be quantized in integer multiples of the magnetic flux quantum,

$$\Phi_0 = \frac{h}{2e} = 2.0678 \times 10^{-15} \text{ Wb}. \quad (2.30)$$

This quantization of magnetic flux is the principle behind SQUIDs, which are discussed in Chapter 3; additionally, in Type II superconductors, each vortex present in the mixed state contains exactly one magnetic flux quantum, further supporting the quantum mechanical nature of superconductivity [51].

By combining the above theories, the theoretical values for  $H_C$ ,  $H_{C1}$ , and  $H_{C2}$  can be written purely in terms of characteristic quantum mechanical values [48]:

$$H_C = \frac{\Phi_0}{2\sqrt{2}\pi\lambda_L\xi}, \quad (2.31)$$

$$H_{C1} = \frac{\Phi_0}{4\pi\lambda_L^2} \ln\left(\frac{\lambda_L}{\xi}\right), \text{ and} \quad (2.32)$$

$$H_{C2} = \frac{\Phi_0}{2\pi\xi^2}. \quad (2.33)$$

These *thermodynamic fields* are for superconductors in the absence of an external magnetic field. However, when a magnetic field is applied, such as in the case of SRF cavities, it is possible for the material to remain in the superconducting state even above the (lower) thermodynamic critical field. This metastable “superheated” state of superconductivity can persist up to the superheating field,  $H_{sh}$ , which can be expressed in terms of the thermodynamic critical field and the Ginzburg-Landau parameter of the material [16]. For Type I superconductors,

$$H_{sh} = \frac{1}{\sqrt{\kappa}} H_C, \quad (2.34)$$

while for Type II superconductors,

$$H_{sh} = \frac{0.89}{\sqrt{\kappa}} H_C \quad \text{for } \kappa \ll 1, \quad (2.35)$$

$$H_{sh} = 1.2 H_C \quad \text{for } \kappa \approx 1, \quad (2.36)$$

$$H_{sh} = 0.75 H_C \quad \text{for } \kappa \gg 1. \quad (2.37)$$

## 2.3 Insulator-to-Metal Transitions

Just two years after the development of the London equations, interest arose in a completely different type of phase transition - insulator-to-metal transitions (IMTs)<sup>6</sup>. In 1937, it was noticed that nickel oxide did not obey the existing theory of metals and non-metals as discussed at the end of Section 2.1: it has a partially filled band, which should make it a metal, but it behaves as an insulator [23]. In the following years, as transitions of similar materials from an insulator to a metal were investigated further, two distinct possible causes of the transition were proposed [65, 66].

### 2.3.1 Peierls vs Mott Transitions

One explanation for the insulating behavior of materials that should be metals was put forth by R. Peierls in 1955 [65]. In the Peierls picture, as shown in Figure 2.5, evenly-spaced one-electron atoms (those with only a partially filled electronic band) will naturally shift into a more energetically-favorable arrangement by moving  $\pm\delta$ . This apparent “pairing” of the atoms opens an energy gap, making the material an insulator. By forcing the atoms apart again, e.g. by applying a given amount of energy to the material, it is then possible to move the atoms so that they are uniformly spaced again, collapsing the band gap and causing the material to behave as a metal. In this reversible transition, when that energy is removed, the atoms then re-form their pseudo-pairs, returning the material to its insulating state.

An alternative explanation, proposed by N. F. Mott in 1949, claims electron behavior, rather than a structural change, is the cause of the insulating state in these materials [66]. In the Mott picture, the positive ions of the lattice are fixed; when the screening potential

---

<sup>6</sup>As theory often begins with the metallic state, theoretical discussions of IMTs typically refer to them as metal-to-insulator transitions. This dissertation uses “insulator-to-metal” because, experimentally, the materials of interest here begin in their insulating state and are then transitioned into their metallic state.

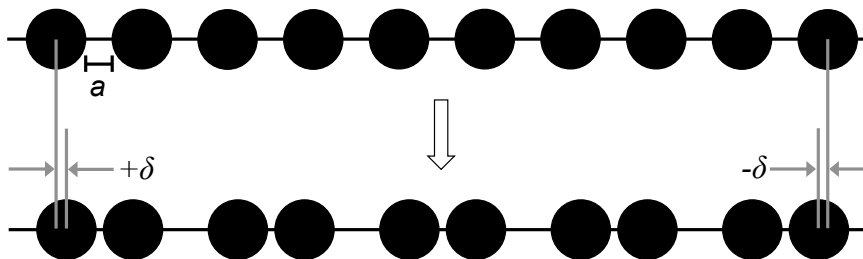


FIG. 2.5: Representation of the Peierls distortion in a lattice. The top arrangement is less energetically favorable than the bottom; as the atoms “pair” up, they cause a shift in the electronic structure of the material, opening a band gap that causes it to behave as an insulator.

of such an ion becomes large enough, it traps an electron, changing the electronic structure of the material and making it behave as an insulator. To transition the material to a metal, enough energy must be applied to “kick” the electrons away from the ions holding them in place. In the reversible transition, once the electrons are free, the electronic structure changes to again close the band gap.

Many materials that exhibit an IMT go through both a Peierls and a Mott transition; even after many decades of study, it is not yet clear which mechanism drives these transitions [11, 32, 41].

# CHAPTER 3

## Experimental Methods

This chapter details the primary experimental methods used to prepare and characterize the Nb, NbN, NbO<sub>2</sub>, and VO<sub>2</sub> thin films discussed in this thesis. The first section describes the thin film deposition techniques used to produce the films studied here, while the remaining sections outline the techniques used to characterize them. Section 3.2 discusses X-ray diffraction (XRD) and X-ray reflectometry (XRR), which were used to obtain structural information about all of the films. Section 3.3 covers the use of a superconducting quantum interference device (SQUID) magnetometer, which was used to determine the superconducting properties of the Nb and NbN films. Finally, Section 3.4 describes an ultrafast laser in a pump-probe configuration, such as was used to study the light-induced insulator-to-metal transition in the NbO<sub>2</sub> and, secondarily, VO<sub>2</sub> films. Other techniques used for only specific portions of this dissertation will be discussed with the resulting data.

### 3.1 Thin Film Deposition

As stated in Chapter 1, thin films are constrained in one physical dimension; this constraint, along with variations in the method used to create a film, can lead both to

useful material properties and the ability to control them. In order to understand how this is possible, it is necessary to explore the manner in which thin films grow, as well as the methods used to deposit them.

### 3.1.1 Thin Film Structure

Any thin film deposition proceeds in three main phases - nucleation, growth, and coalescence - although the transition from the first phase to the second (the end of nucleation into the beginning of growth) is not sharply defined. The early stages especially are heavily influenced by the choice of substrate, the material on which the film is deposited. If a film grows in a specific orientation relative to a crystalline substrate, it is referred to as an *epitaxial* film. *Homoepitaxy* occurs when the crystal lattice spacing of the substrate and the material being grown are the same (which is typically only the case when they are the same material); *heteroepitaxy* occurs when the lattice spacings are different. In the case of heteroepitaxial films, the lattice mismatch between substrate and film often causes some amount of strain in the film (see Figure 3.1), although this is typically relieved as the film thickness increases, e.g. as the film material is deposited farther away from the constraints of the substrate [67].

Strain and relaxation of course affect the overall crystal structure of the film [68], which in turn affects the film properties, including electronic behavior [69, 70]; the substrate can therefore be deliberately chosen to induce certain manifestations of strain that will result in desired film properties.

The evolution of thin film growth and the coalescence of the deposited material into a continuous film are governed by many factors; interested readers may consult Reference [67] for a full overview. The interplay of these factors yields film structures that can be divided into zones based on their structure, which are shown in Figure 3.2 [71].

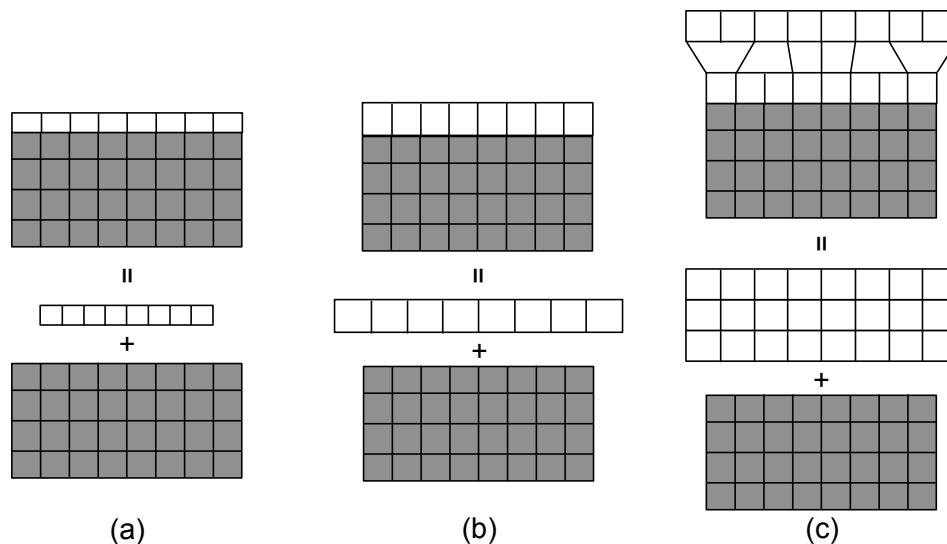


FIG. 3.1: Three possible types of heteroepitaxy: (a) tensile and (b) compressive strain, and (c) relaxed compressive strain.

### 3.1.2 Deposition Methods

The choice of deposition method (and the specific set of deposition conditions used) depends on the type of material being deposited, the size and shape of the substrate, and the desired film properties (i.e. density, grain size and shape, crystal orientation, etc.). There are a wide variety of methods available, but they can largely be grouped into two categories - chemical or physical vapor deposition (CVD or PVD, respectively).

CVD processes use gas flow along a substrate surface where, generally with the assistance of a chemical precursor, a chemical reaction occurs to produce the film. These methods, such as atomic layer deposition (ALD), give a high degree of control over the stoichiometry of the film, can grow films as thin as a single atomic layer, and can be used to conformally coat substrates with some shape to them; it is however often difficult to scale CVD methods to grow large films, and the precursors can be quite hazardous [67].

In PVD processes, a vapor of the material being deposited, created by either evapora-

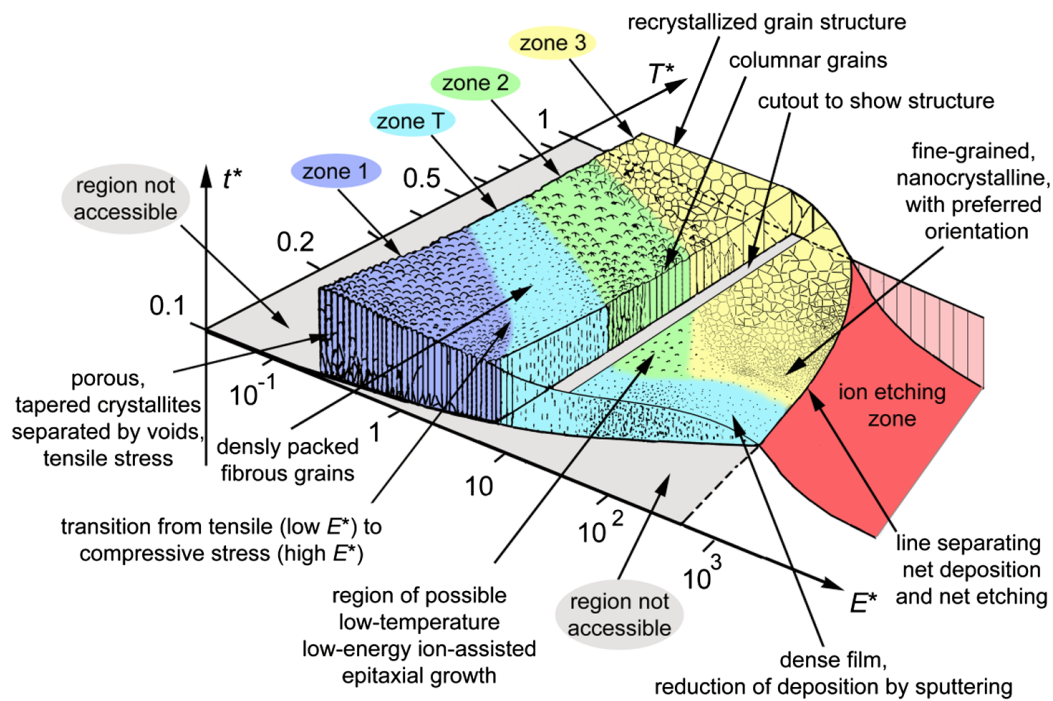


FIG. 3.2: Extended structure zone diagram showing the effect of film thickness  $t^*$ , growth temperature  $T^*$ , and deposition energy  $E^*$  on film structure. Reproduced with publisher permission from Reference [71].

tion or sputtering (ejection of the material from a solid “target”), travels from the target to the substrate. Evaporation techniques are often very fast, but produce low-density films; sputtering produces uniform, dense films, but is comparatively slower than evaporation [67]. In any sputtering technique, there will always be some inherent film defects - some substrate-induced, others introduced by the manner in which the films are grown (e.g. lattice site vacancies caused by the working gas taking the place of the target material in the film). Sputtering is still a popular method for depositing films, though, due to the uniformity and reproducibility of sputtered films, as well as the high degree of control it allows over the deposition conditions [67]. The films discussed in this dissertation were all produced via various sputtering techniques, which are described below.

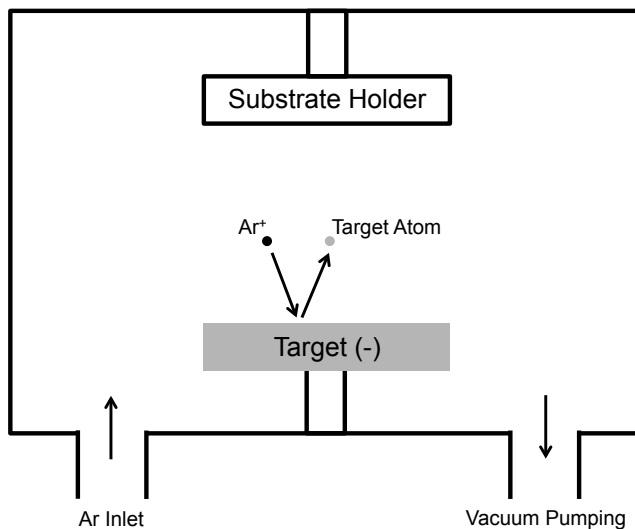


FIG. 3.3: Illustration of a magnetron sputtering system.

## DC and Reactive Magnetron Sputtering

In *DC magnetron sputtering*, depicted in Figure 3.3, a heavy, inert working gas such as argon (Ar) is leaked into a vacuum chamber; this gas, the sputtering plasma, is ionized and therefore accelerates towards the solid target material, which acts as a cathode. The inert ions impact with the target and some percentage of them eject target material atoms, which then travel to the substrate. Magnets are used to confine the plasma near the target, which increases the rate of collisions and therefore the sputtering rate [67].

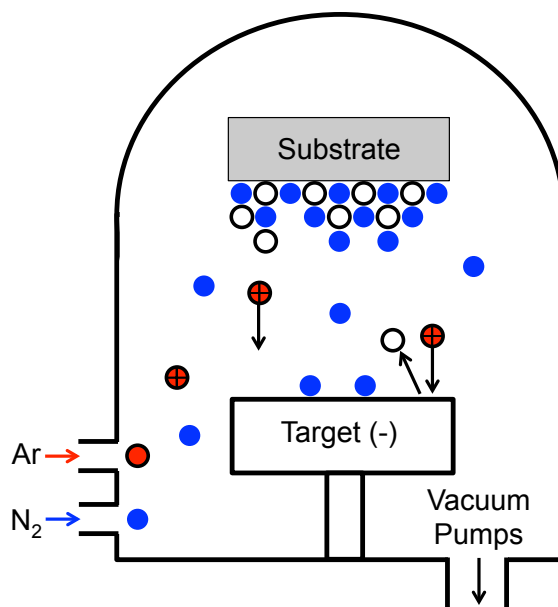


FIG. 3.4: Schematic illustrating a reactive magnetron sputtering process.

*Reactive magnetron sputtering*, shown in Figure 3.4, is a variation of DC sputtering in which the working gas is mixed with a reactive gas such as nitrogen or oxygen in order to produce compound films (e.g. nitrides or oxides, to use the previous examples) [67]. In reactive sputtering, the *partial pressure* - the relative amount of the reactive gas to the working gas - has a strong effect on the resulting film composition [72]. Reactive

sputtering was used in Dr. R. A. Lukaszew's laboratory at the College of William & Mary to grow the NbN films discussed in Sections 4.4 and 4.5.

### Other Sputtering Techniques

In recent years, several sputtering techniques have been developed that are more energetic than magnetron sputtering, allowing access to more zones in the film structure zone diagram (Figure 3.2) and often producing films with more desirable properties.

In the case of superconducting films, techniques that produce higher degrees of ionization of the sputtered material, such as *Electron Cyclotron Resonance* (ECR), have been shown to yield better-performing films [73–76]. The Nb films provided by Dr. A.-M. Valente-Feliciano of the SRF Institute at Thomas Jefferson National Accelerator Facility for the work included in this dissertation (Sections 4.1-4.3) were all grown via ECR.

When sputtering oxides, achieving single-phase films is often difficult due to the number of possible oxidation states of the target material. Dr. S. A. Wolf and Dr. J. Lu's group at the University of Virginia use a technique known as *Reactive Biased Target Ion Beam Deposition* (RBTIBD) to overcome this problem and produce high-quality oxide films such as the NbO<sub>2</sub> and VO<sub>2</sub> films discussed in Chapter 5 [77].

## 3.2 X-Ray Diffraction and Reflectometry

Once a film has been deposited, we must be able to characterize various of its properties, typically beginning with its microstructure. X-ray scattering techniques such as X-ray diffraction (XRD) and X-ray reflectometry (XRR) are among the most common methods used for such structural characterization.

### 3.2.1 X-Ray Diffraction (XRD)

XRD is a very powerful tool for *ex-situ* characterization of the microstructure of crystalline materials, particularly thin films. In the simplest sense, XRD produces observable interference patterns created when X-rays diffract off of a crystalline material (i.e. a material in which the constituent atoms are arranged periodically); these patterns can then be used to extract both qualitative and quantitative information about the material structure. The specific diffraction condition required - known as the Bragg condition, or Bragg's Law - is given by

$$n\lambda = 2 d \sin \theta, \quad (3.1)$$

where  $n$  is an integer known as the order of the diffraction and  $\lambda$  is the wavelength of the incident X-ray [51]. As shown in Figure 3.5,  $d$  is the distance between diffraction layers (atomic layers) and  $\theta$  is the angle between the incident X-ray and the sample.

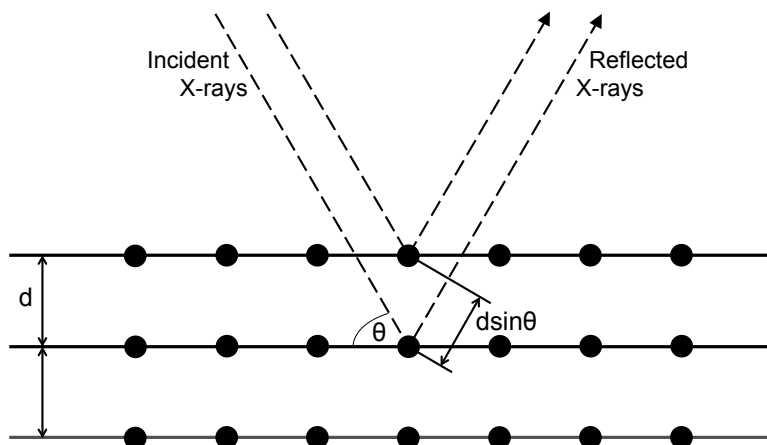


FIG. 3.5: Schematic of the simple X-ray scattering used in XRD.

Equation 3.1 is only valid when  $\lambda \leq 2d$ ; physically, this simply means that in order

to probe interference on the length scale of interatomic distances, the probe itself (here, the X-ray) must be of that same length scale or smaller. To generate such X-rays in laboratory XRD instruments, electrons ejected from a hot filament are accelerated toward a target material (e.g. Cu) with enough kinetic energy to remove electrons from its core shell; valence electrons then move to fill the core shell vacancies, emitting characteristic X-rays, which are optically focused into a quasi-parallel beam to illuminate the sample. In the work presented in this dissertation, the X-rays are the Cu  $K\alpha_1$  emission, with a wavelength of 0.15418 nm (well below the diffraction limit). Additional optics are used to block out other possible wavelengths.

Thin film XRD studies impose unique challenges on alignment and signal optimization. The signal from the film itself is usually much weaker than that from the bulk crystalline substrate, and there can also be a slight angular misalignment between the film and the substrate. To address these difficulties, thin film X-ray diffractometers must be equipped with a four-circle goniometer, such as the one shown in Figure 3.6; this provides access to additional angles of rotation in order to improve alignment and achieve a larger signal intensity from the film.

While XRD provides a great deal of structural information about the material being studied, this dissertation focuses on the out-of-plane lattice parameter, the average size of crystallites within the film, and the degree of ordering in the material. To obtain this type of information, two types of scans are used - high-angle  $\theta$ - $2\theta$  scans, and  $\omega$  scans, or rocking curves.

To identify the phases present in a thin film, the location of the Bragg diffraction peaks (i.e. the values of  $2\theta$  at which the peaks occur) from high-angle  $\theta$ - $2\theta$  scans are compared to a powder diffraction reference file. The diffraction peak angles can then be used with Equation 3.1 to determine the out-of-plane distance between lattice planes in the film.

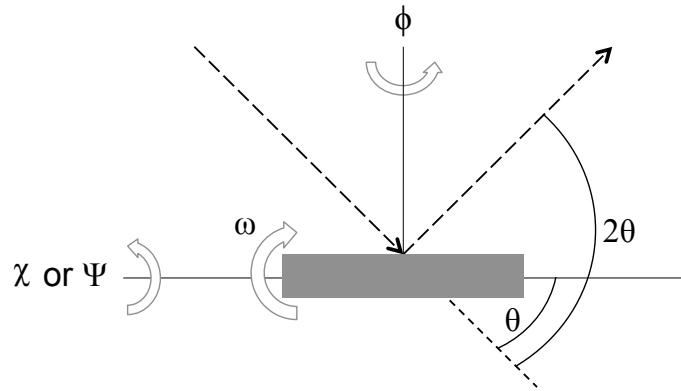


FIG. 3.6: Angles accessible with a four-circle goniometer.  $\theta$  (X-ray source) and  $2\theta$  (detector) can be set independently, while  $\omega$  rotates about an axis normal to the  $\theta$ - $2\theta$  plane.  $\phi$  rotates about the axis normal to the sample surface and provides  $360^\circ$  of azimuthal rotation.  $\chi$  (also referred to as  $\Psi$ ) rotates about an axis normal to the axes of rotation for  $\omega$  and  $\phi$  and helps overcome possible angular misalignment between diffraction planes in the film and the substrate.

High-angle  $\theta$ - $2\theta$  scans can also be used to calculate the approximate average crystallite or grain size,  $L$ , from the Scherrer equation

$$L = \frac{K\lambda}{\beta \cos \theta}, \quad (3.2)$$

where  $K$  is a dimensionless geometric constant, determined by the symmetries of the crystal lattice being considered, and  $\beta$  is the full-width half-maximum (FWHM) of the Bragg diffraction peak [78].

Because of the way thin films grow, as discussed in Section 3.1, there will always be boundaries between individual crystallite grains; the long-range order, or mosaicity, of these boundaries, and thus the grains, can be determined by fixing the incident angle  $\theta$  and “rocking” the sample about the  $\omega$  axis. Films with rocking curves that exhibit a narrow FWHM have a high degree of long-range order.

### 3.2.2 X-Ray Reflectometry (XRR)

XRR is XRD performed at grazing angles, rather than the higher angles discussed above, and provides information about film thickness, density, and roughness. In an XRR scan, the reflected intensity of the X-rays is plotted as a function of  $\theta$  over a shallow angular range (typically no more than  $5^\circ$ ; see Figure 3.7); these data are then fit to models by algorithmically varying the thickness, density, and roughness from known bulk values [79, 80].

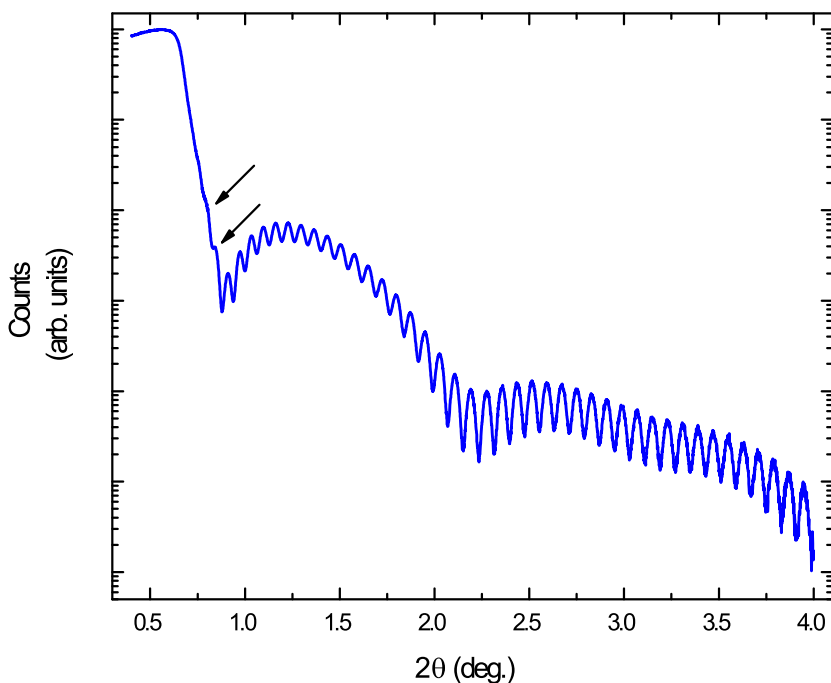


FIG. 3.7: Representative XRR scan. The first reflection fringe can be seen at  $\sim 0.6^\circ$ ; arrows indicate the second and third fringes. These three fringes correspond to a capping layer on the film, while the closely-spaced reflection fringes that begin around  $0.8^\circ$  are due to the comparatively thicker, more crystalline film.

### 3.3 SQUID Magnetometry

Many superconducting properties of a material can be determined by measuring its magnetic response (see Section 2.2) to varying temperature and magnetic fields. Such measurements are often performed via SQUID magnetometry.

Superconducting quantum interference devices (SQUIDs) are extremely sensitive magnetic sensors [81] based on Josephson junctions and the quantization of magnetic flux. A Josephson junction is composed of two pieces of superconducting material separated by a thin barrier - typically an insulating layer, but a non-superconducting metal or a physical constriction of the material itself may also be used [81] - through which Cooper pairs (see Chapter 2.2.3) can tunnel, creating a superconducting current; above some critical current  $I_C$  a voltage appears across the insulating layer [82]. A single Josephson junction is an RF SQUID, which was not used in this work and thus is not discussed here; information on the operation of RF SQUIDs can be found in Chapters 1 and (in greater detail) 6 of Reference [81]. Two Josephson junctions connected in parallel constitute a DC SQUID [81], shown in Figure 3.8, the operation of which is described below.

Because magnetic flux is quantized [83–85], the flux passing through a SQUID must be an integer multiple of the magnetic flux quantum  $\Phi_0$ . In a DC SQUID with no applied magnetic field, an applied superconducting current (below the critical current  $I_C$ ) is split evenly across the two Josephson junctions. When a field is then applied, the flux across the SQUID increases and a change in voltage is seen across the junctions. If the increase in flux is less than  $\Phi_0/2$ , a screening current is established in the SQUID equal and opposite to the increased flux to return the flux through the SQUID to zero; this decreases the current through one junction but increases the current through the other above  $I_C$ , resulting in a voltage change of  $+V$ . If the flux increase is larger than  $\Phi_0/2$ , however,  $\Phi_0$  is more energetically favorable, and the current must flow in the same direction as the increased

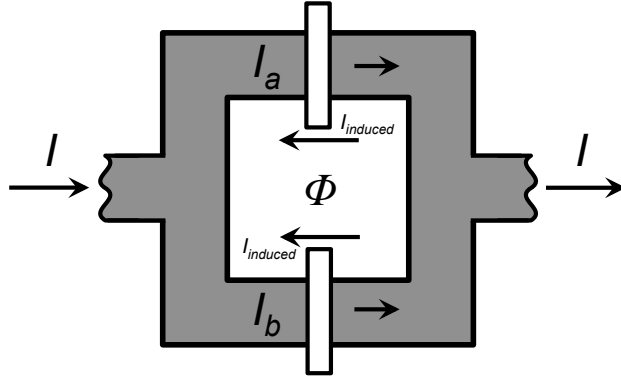


FIG. 3.8: DC SQUID.

flux in order to ensure that the flux through the SQUID is now  $\Phi_0$ , resulting in a voltage change of  $-V$ . Thus as the flux across the SQUID continues to increase, the voltage across the Josephson junctions oscillates with a period of  $\Phi_0/2$ ; the total change in flux due to the applied field can then be determined simply by counting the number of oscillations in the voltage [81].

In order to measure properties such as the critical temperature and critical field(s) of a sample, SQUIDS are combined with a temperature control system, a superconducting electromagnet, and a sample manipulator; liquid helium ( $L_{He}$ ) is used to both change the temperature of the sample during measurements and to cool the superconducting components of the measurement system itself. The superconducting measurements discussed in this dissertation were, unless otherwise noted, made using a Quantum Design MPMS<sup>®</sup> (Magnetic Property Measurement System) XL, which can apply fields from -7 to +7 T and resolve changes in magnetic flux on the order of  $10^{-15}$  T over a temperature range of 2-400 K [86].

During a SQUID MPMS measurement, the magnetic sample - which can be no wider

than 5 mm due to the cylindrical geometric constraints of the system - is vertically displaced by a stepper motor through superconducting pickup coils with an applied field in the direction of motion, as shown in Figure 3.9, thus changing the flux and inducing a current through them. As discussed above, the SQUID converts this current to a voltage, which is then programmatically fit in order to determine the magnetic moment of the sample [86].

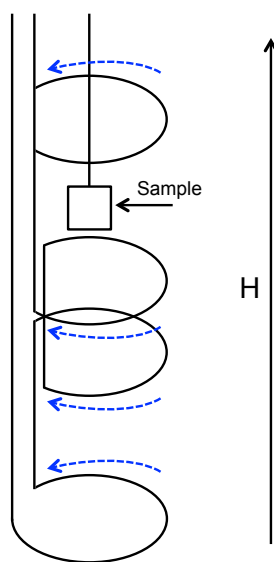


FIG. 3.9: Geometry of the SQUID MPMS pickup coils. As the sample of interest is moved vertically through the coils, the induced current is seen as a voltage change across the SQUID.

### 3.3.1 $T_C$ Measurements in Superconducting Thin Films

The first property we measure for any superconducting film is the critical temperature ( $T_C$ ), i.e. the temperature above which the superconducting state is lost. The sample is first cooled to a temperature well below the expected  $T_C$  value (which is assumed to be near that of the bulk material), typically 5 K, and a small magnetic field on the order of

10-25 Oe<sup>1</sup> is applied, resulting in a negative magnetic moment. The temperature is then increased in discrete steps without varying the magnetic field until the magnetic response of the sample returns to zero, as shown in the representative  $T_C$  measurement presented in Figure 3.10. While there are several ways to define  $T_C$  from such a plot [60, 87], for the purposes of this dissertation,  $T_C$  is defined to be the point at which the slope of the M-vs-T curve changes from concave upward to concave downward as determined by a second-derivative fit of the data.

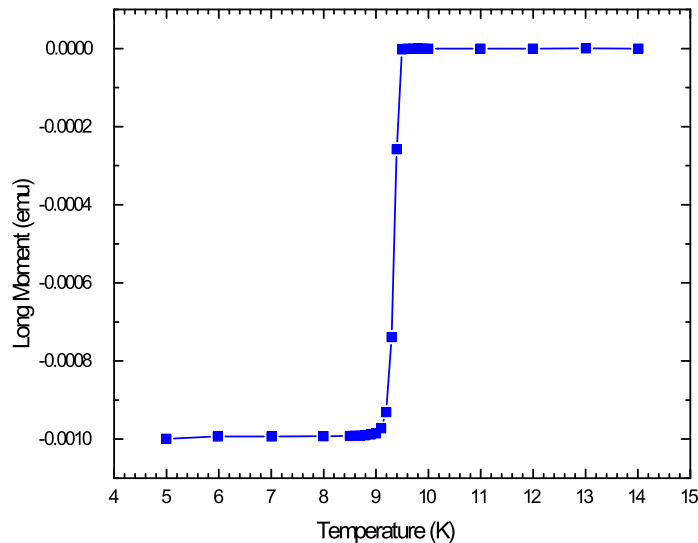


FIG. 3.10: Representative  $T_C$  measurement showing sample magnetization as a function of temperature.

### 3.3.2 Critical Field Measurements in Superconducting Thin Films

Two methods of measurement were used in order to determine the critical field values for each sample: (1) simple measurement of the magnetization (M, in emu) with respect to

<sup>1</sup>All measurements discussed in this dissertation use the unit Oersted (Oe), rather than Tesla (T), for magnetic fields. 1 Oe is equivalent to 0.1 mT.

applied field and (2) a more conservative method outlined in [88]. In this method, for each value of applied field, the sample is cooled to the specified temperature and a zero-field measurement of  $M$  is made. Then the given field is applied and another measurement of  $M$  is made (providing the typical M-H data), before the field is removed and a final zero-field measurement is taken and the sample is warmed above its  $T_C$ . The lower critical field is then determined by subtracting the first zero-field measurement from final measurement;  $H_{C1}$  is the applied field at which this difference deviates from zero, i.e. the first applied field at which there is a trapped field in the sample [5].

This method accounts for flux pinning in the sample, resulting in a slightly lower  $H_{C1}$  value than the traditional M-H method, in which  $H_{C1}$  is the field at which the M-H data deviates from the Meissner slope (e.g. is no longer linear). Even so, both methods give at least a slight underestimate of the true value of  $H_{C1}$ , as surface quality and sample alignment are crucial. The magnetic moment of a thin film is given by

$$m = \frac{VH}{4\pi} \left( \cos^2 \theta + \frac{1}{1-D} \sin^2 \theta \right), \quad (3.3)$$

where  $V$  is the volume of the film,  $H$  is the applied field,  $\theta$  is the angle between the applied field and the film surface, and  $D$  is the demagnetization factor [22]; any field not parallel to the film surface, e.g.  $\theta \neq 0$ , will introduce a perpendicular component to the applied field, making  $H_{C1}$  appear lower than it is. Additionally, the demagnetization factor  $D$  is proportional to the square of the RMS surface roughness of the films [89]; because thin films will never be perfectly smooth, there will therefore always be some non-parallel field components in these measurements. Careful alignment using an azimuthal rotation mechanism is performed before all measurements to ensure that these effects and thus the magnetic moment of the sample is minimized [5].

In some cases, further measurements were made to determine an approximate value

for the upper critical field  $H_{C2}$  [5]. In the traditional M-H method,  $H_{C2}$  is defined as the field at which the magnetic moment of the sample returns to zero; in the trapped field method from [88] described above,  $H_{C2}$  is the field at which the trapped field value reaches a plateau at its maximum value.

## 3.4 Ultrafast Lasers in Pump-Probe Configuration

Ultrafast pump-probe spectroscopy is a well-established method for studying relaxation dynamics in condensed matter systems, and has been used extensively to probe carrier relaxation processes in semiconductors [90]. Beginning in 1971, such laser systems have also been used to investigate the nature of the insulator-to-metal transition in VO<sub>2</sub> thin films [26], although it was not until 1994 that the time resolution in these measurements was short enough to resolve the electronic behavior of the material [40]. Because the time resolution depends on the duration, or pulsewidth, of the laser pulse [90], the generation of sub-picosecond ultrafast pulses is key to any experiment trying to resolve electron-electron interactions.

### 3.4.1 Generation of Ultrafast Pulses

The duration of a laser pulse is dependent on the bandwidth - the width of the spectrum around the central wavelength - of the pulse according to a relationship known as the *time-bandwidth product*; for a Gaussian pulse, this relationship is  $\Delta\nu\Delta t = 0.44$ , where  $\Delta\nu$  is the bandwidth of the pulse in Hz and  $\Delta t$  is the pulse duration [91]. In order to generate sufficiently short pulses, then, there must be a correspondingly large range of wavelengths enclosed in the pulse. It is for this reason that titanium:sapphire (Ti:sapph) crystals are often used in ultrafast laser systems - they can support a very wide bandwidth ranging from 680 nm to 1100 nm [91].

In any laser cavity, there are many possible “modes” (integer multiples of half wavelengths) that can exist, but that are not necessarily in phase with each other, as shown in Figure 3.11. *Modelocking*, then, is the process by which the phases of the modes are adjusted to bring them into phase with each other, creating well-defined laser pulses [92]. Modelocking can be either passive or active; in the laser system used for the work discussed in this dissertation, passive modelocking is used. The length of the laser cavity is rapidly changed by a solenoid-driven mirror at one end of the cavity, changing the modes that the cavity can support. When a large number of modes are in phase with other, the Ti:sapph crystal saturates and no longer supports modes that have a different phase; once this modelocking begins, it continues without the need for further driving [92].

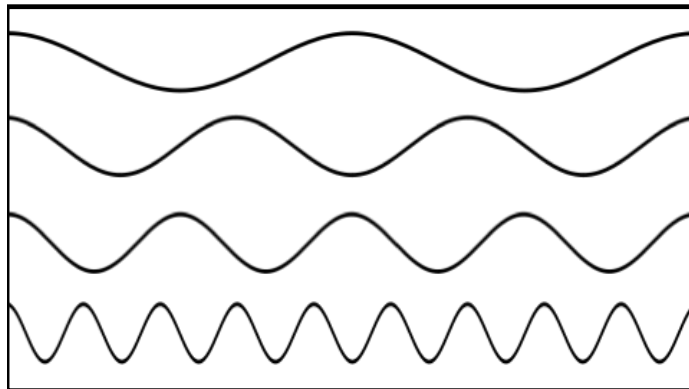


FIG. 3.11: Some possible modes that can exist in a laser cavity.

After the laser pulses have been generated by modelocking, their energy can be increased via a regenerative amplifier. Here again a Ti:sapph crystal is commonly used, as it can amplify pulse energy by approximately 6 orders of magnitude. Upon entering the regenerative amplifier, a pulse is first stretched by a grating that sends different frequency light over different path lengths (the stretcher) - the higher frequency components of the pulse travel a greater distance than the lower frequency components. The stretched pulse, which is now less energetic than the input pulse, then passes through the Ti:sapph crys-

tal multiple times and is amplified before traveling to another grating. This grating (the compressor) is set up in the opposite configuration as the stretcher and serves to compress the pulse back to nearly the same pulsewidth as the input pulse: here, the high-frequency portion of the pulse travels a shorter distance than the low-frequency portion [91].

### 3.4.2 Experimental Setup

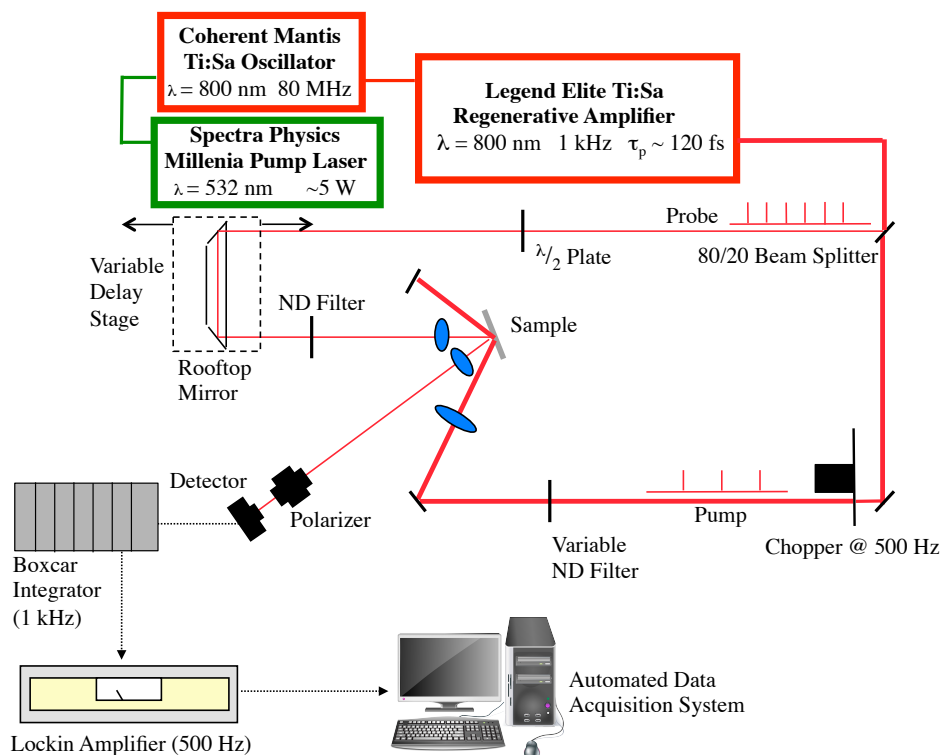


FIG. 3.12: Schematic of the ultrafast pump-probe setup used for the reflection studies contained in this dissertation. For the transmission studies, only the position of the polarizer and detector changed.

The ultrafast pump-probe setup used for this experiment is shown in Figure 3.12. The Ti:sapph laser system emits pulses of  $\sim 120$  fs at a center wavelength of 800 nm and

a repetition rate of 1 kHz. The laser output is attenuated and split into a pump beam and a weaker probe beam using an 80/20 beam splitter. The pump beam passes through an optical chopper with a frequency of 500 Hz (in order to modulate the excitation of the sample) and is further attenuated using a variable neutral-density (ND) filter in order to control the fluence before focusing to an  $\sim 80 \mu\text{m}$  diameter spot on the sample. The probe beam reflects off a rooftop mirror mounted on a variable delay stage to control the relative delay between the pump and probe beams by up to 4 ns. Following the delay stage, the probe beam is heavily attenuated to a fluence far below that of the pump beam (3-5 orders of magnitude weaker) and its polarization is rotated  $90^\circ$ , making it perpendicular to the polarization of the pump beam and allowing for rejection of scattered pump beam from the detector. The probe beam is focused onto the sample on the same spot as the pump beam but to a smaller diameter ( $\sim 40 \mu\text{m}$ ) using a shorter focal length lens to ensure probing of only the central region of the pumped region where the effects of the optical excitation can be considered one-dimensional in the direction perpendicular to the surface [11].

For reflection measurements, the probe beam reflects off the sample, passes through a polarizer set to pass only the probe polarization, and focuses onto a silicon photodetector; for transmission measurements, the polarizer and photodetector are moved so that the probe beam instead passes through the sample before reaching them. The photodetector signal is input to a boxcar integrator triggered by a 1 kHz reference from the pulse controller for the Legend. Using the boxcar integrator, the signal of the photodetector from each probe pulse is integrated over a window of 230 ns; the last sample output of the boxcar, which is a scaled DC voltage of the integrated signal, is updated at the 1 kHz repetition rate of the laser and provides the input to a lock-in amplifier. This measurement scheme eliminates the dead time between laser pulses and produces a very low noise floor and thus an improved signal-to-noise ratio. All data are reported as  $\Delta R/R$  (or  $\Delta T/T$ ), computed by dividing the change in the intensity of the reflected (transmitted) probe beam, the

magnitude of the lock-in signal with both pump and probe beams present, by the baseline reflectivity (transmissivity) of the sample, the lock-in signal from the probe beam only [11].

A LabView<sup>®</sup> program was used to control the delay stage position and acquire data from both the boxcar integrator and the lock-in amplifier for each position of the stage. The program moves the stage in steps as small as  $1.25 \mu\text{m}$ , corresponding to a relative delay of 8.34 fs, well below the time resolution of the measurement scheme. The smallest steps used here were  $2 \mu\text{m}$  (13.3 fs of delay) [11].

## CHAPTER 4

# Superconductivity in Niobium and Niobium Compound Thin Films

### 4.1 Temperature and Microstructural Effects on the Superconducting Properties of Niobium Thin Films

#### 4.1.1 Introduction

As discussed in Chapter 1, Nb thin films are very appealing for applications, but the effects of their microstructure on their superconducting properties are not yet well understood. Here, we present temperature-dependent DC studies on the critical temperature and critical fields of Nb thin films grown on r-plane sapphire ( $r\text{-Al}_2\text{O}_3$ ) and copper (Cu) surfaces and correlate the DC superconducting properties of these films with their microstructure, which allows for the possibility of tailoring future films for a specific application. This work was presented at the 2016 Applied Superconductivity Conference in Denver, CO, USA, and is published in Reference [5].

## 4.1.2 Experimental Methods and Results

### Film Growth

The Nb films studied here range from 1-2  $\mu\text{m}$  thick and were grown on r- $\text{Al}_2\text{O}_3$  and four types of Cu surfaces - single-crystal (110) and (111) and polycrystalline fine-grained and large-grained - via electron cyclotron resonance (ECR) [73, 74] at  $360^\circ\text{C}$ . The films on r- $\text{Al}_2\text{O}_3$  (nucleation at 124 eV) and polycrystalline Cu (nucleation at 184 eV) were grown with an ion energy of 64 eV; the films grown on single-crystal Cu were coated at an ion energy of 184 eV.

r- $\text{Al}_2\text{O}_3$  provides a high-quality surface for film growth, and other Nb-based superconducting films grown on r- $\text{Al}_2\text{O}_3$  have had very high thickness uniformity [93]. Additionally, Nb/r- $\text{Al}_2\text{O}_3$  films have been shown to have a residual resistance ratio (RRR) more than one-and-a-half times larger than bulk Nb [94].

Cu is a popular choice for Nb films due to its applicability in SRF cavity coatings (see Section 1.1.2), but because the structure of the chosen Cu surface affects the resulting Nb film, studying a variety of Cu surfaces is most useful. In general, films grown on single-crystal Cu(111) surfaces perform better than those grown on the other three Cu surfaces used [94], but growing on such a specific type of substrate may not always be feasible, hence the need for information on single-crystal Cu(110) and polycrystalline surfaces.

### Microstructure Via X-Ray Diffraction

Structural characterization via X-ray diffraction (XRD) was performed with a PANalytical Empyrean X-ray diffractometer. Representative high-angle  $2\theta$ - $\omega$  scans for a typical Nb film grown on polycrystalline Cu and one grown on r- $\text{Al}_2\text{O}_3$  are shown in Figure 4.1.

For the films grown on single-crystal Cu(110) and (111), the primary Cu reflections seen were Cu(022) and Cu(111), respectively, although small contributions from other

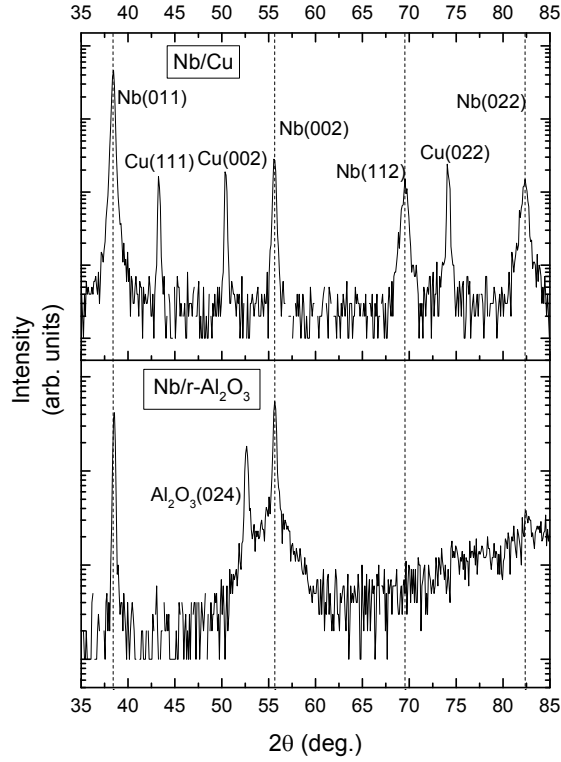


FIG. 4.1: High-angle  $2\theta$ - $\omega$  scans for Nb/Cu (top) and Nb/r-Al<sub>2</sub>O<sub>3</sub> (bottom) films. In the top scan, all three possible Cu reflections and all four possible Nb reflections are shown. The lower-order Al<sub>2</sub>O<sub>3</sub>(012) reflection was also seen at 25.6° in the Nb/r-Al<sub>2</sub>O<sub>3</sub> film.

orientations of Cu were also observed. Table 4.1 lists all substrate and film reflections seen in each sample, with the Sample ID indicating which type of substrate was used. The microstructural information obtained from the strongest Nb reflection in each sample (given in bold in Table 4.1) using the methods described in Section 3.2.1 is summarized in Table 4.2. The lattice parameter for bulk Nb [95] is also included for reference; it is important to note that all samples exhibited strain, indicated by a greater-than-bulk lattice parameter.

TABLE 4.1: Substrate and film reflections seen in high-angle  $2\theta$ - $\omega$  scans for each sample. The reflections given in bold for each sample are the strongest film and substrate reflections present in that sample.

Sample ID <sup>a</sup>	Film Reflections	Substrate Reflections
r-Al <sub>2</sub> O <sub>3</sub>	Nb (011), <b>(002)</b> , (022)	Al <sub>2</sub> O <sub>3</sub> (012), <b>(024)</b> , (306)
Cu-fg-124	Nb <b>(011)</b> , (002), (112), (022)	Cu (111), (002), <b>(022)</b>
Cu-LG-124	Nb (011), <b>(002)</b> , (022)	Cu (111), <b>(022)</b>
Cu-fg-141	Nb <b>(011)</b> , (112), (022)	Cu (111), (002), <b>(022)</b>
Cu-LG-141	Nb <b>(011)</b> , (112), (022)	Cu (111), <b>(022)</b>
Cu-110-108-5	Nb <b>(011)</b> , (002), (112), (022)	Cu (002), <b>(022)</b>
Cu-111-108-5	Nb <b>(011)</b> , (002), (112), (022)	Cu <b>(111)</b> , (002), (022)

<sup>a</sup> The Cu substrates used are polycrystalline fine-grained (Cu-fg), polycrystalline large-grained (Cu-LG), single-crystal (110) (Cu-110), or single-crystal (111) (Cu-111).

TABLE 4.2: Lattice parameters and lower critical field values for the Nb films studied here, as well as the corresponding bulk values. Bulk lattice information is from Reference [95], while superconducting properties are from Reference [3].

Sample ID	Sample Thickness ( $\mu\text{m}$ )	Lattice Parameter ( $\text{\AA}$ )	Avg. Out-of-Plane Grain Size (nm)	Mosaicity ( $^\circ$ )	$T_C$ (K)	$H_{C1}(0)$ (Oe)	$H_{C2}(0)$ (Oe)
r-Al <sub>2</sub> O <sub>3</sub>	1.2	3.301	36.156	0.326	9.25	1769 $\pm$ 21	7622 $\pm$ 341
Cu-fg-124	2	3.310	28.171	5.429	9.36	641 $\pm$ 31	7938 $\pm$ 195
Cu-LG-124	2	3.301	76.946	1.09	9.26	293 $\pm$ 19	10176 $\pm$ 158
Cu-fg-141	2	3.308	32.300	4.359	9.25	918 $\pm$ 59	8285 $\pm$ 372
Cu-LG-141	2	3.306	31.938	3.734	9.32	1349 $\pm$ 24	9651 $\pm$ 190
Cu-110-108-5	1	3.317	30.557	5.228	9.33	1521 $\pm$ 108	7634 $\pm$ 322
Cu-111-108-5	1	3.307	37.666	1.398	9.33	649 $\pm$ 37	9397 $\pm$ 583
<b>Bulk</b>	—	<b>3.300</b>	—	—	<b>9.23</b>	<b>1800</b>	<b>4000</b>

### Determination of $T_C$ and $H_{C1}$ Via SQUID Magnetometry

The Quantum Design MPMS SQUID magnetometer described in Section 3.3 was used to first measure  $T_C$  for each sample; these values are given in Table 4.2. Then measurements were made of  $H_{C1}$  for each sample at five different temperatures (2, 4, 6, 8, and 8.9 K), all below the  $T_C$  of the films, following the method outlined in Section 3.3.2 and Reference [88]. The  $H_{C1}$  data, plotted in Figure 4.2, were then fit with [96, 97]

$$H_{C1}(T) = H_{C1}(0) \left(1 - \frac{T}{T_C}\right)^2, \quad (4.1)$$

where all temperatures are given in Kelvin (K) and all fields are in Oe, in order to determine the zero-T value for  $H_{C1}$ ,  $H_{C1}(0)$ , given in Table 4.2. It is worth noting that while, in general, Nb films grown on large-grained Cu (such as sample LG-141) exhibit better superconducting properties (e.g. higher  $H_{C1}$  values) than those grown on fine-grained Cu, sample LG-124 exhibits a heavily-suppressed  $H_{C1}$ , likely due to substrate processing issues that are not detectable via XRD.

While the upper critical field,  $H_{C2}$ , of each film was not explicitly a value of interest, rough measurements were made at the same five temperatures given above and the resulting data were fit with [97, 98]

$$H_{C2}(T) = H_{C2}(0) \frac{\left(1 - \frac{T}{T_C}\right)^2}{\left(1 + \frac{T}{T_C}\right)^2}, \quad (4.2)$$

to provide an estimate of  $H_{C2}(0)$  to further quantify the superconducting qualities of the films. These values are all greater than the bulk value for Nb [96–98] and are included in Table 4.2.

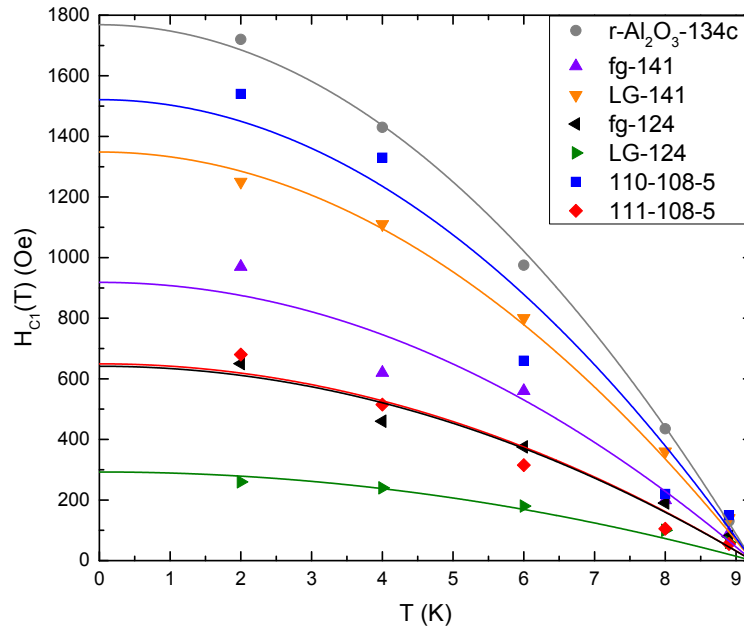


FIG. 4.2:  $H_{C1}$  values as a function of temperature for each Nb sample studied. Individual points are experimental data, while solid lines are fit using Equation 4.1.

## Structure-Property Correlations

All of the samples studied have a  $T_C$  greater than that of bulk Nb, showing that all types of substrate used produce viable superconducting films. Figure 4.3(a), (b), and (c) plot  $T_C$  against the lattice parameter, average out-of-plane grain size, and mosaicity, respectively, for each film studied. In Figure 4.3(a), there is a clear linear relationship between the lattice parameter and the  $T_C$  of a Nb film; this also suggests that a film with a lattice parameter slightly lower than bulk could still have a bulk or higher  $T_C$ . Note that the outlying data point (the film grown on single-crystal Cu (110)) has a significantly larger lattice parameter than any of the other films and as such was excluded from the linear fit of the data. Figure 4.3(b) and (c) further suggest that films with smaller grain sizes and larger mosaicity (higher degree of disorder) have higher  $T_C$  values. The outlying

data point in Figure 4.3(b) corresponds to sample LG-124, which, as noted above, suffers from decreased superconducting performance due to substrate processing issues and as such is excluded from the linear fit.

In Figure 4.4, we consider the effect of the same three microstructural properties on  $H_{C1}(0)$ , obtained from Equation 4.1. In Figure 4.4(a), we again see a linear relationship between the lattice parameter and the superconducting properties of the film, although here, films with more bulk-like lattice parameters have higher  $H_{C1}(0)$ . The two outlying data points correspond to samples 110-108-5 and LG-124 and are excluded from the linear fit for the reasons discussed above. There is no clear relationship between average grain size and  $H_{C1}(0)$  as plotted in Figure 4.4(b), although we see further evidence of the suppressed superconducting performance in sample LG-124. There is also no obvious trend in the mosaicity versus  $H_{C1}(0)$  data in Figure 4.4(c).

Figure 4.5 shows the effect of the microstructure on  $H_{C2}(0)$ . As mentioned above, the measurements of  $H_{C2}(T)$  were not as precise as those of  $H_{C1}(T)$ , leading to larger error in the determination of  $H_{C2}(0)$ . Even so, all calculated values for  $H_{C2}(0)$  are several thousand Oe above the bulk value of 4000 Oe, meaning that films of this quality will retain some improvement of conductivity (i.e. remain in the mixed state) at larger fields than bulk Nb. Figure 4.5(a) shows a similar trend in  $H_{C2}(0)$  as does Figure 4.4(a) - the more bulk-like the lattice parameter, the higher the  $H_{C2}(0)$  - although here the outlying data point corresponds to the sample grown on r-Al<sub>2</sub>O<sub>3</sub>; the linear fit therefore only considers those films grown on comparable (i.e. Cu) substrates. Interestingly, the results shown in Figure 4.5(b) indicate that the otherwise poorly-performing sample LG-124 has a higher  $H_{C2}$  value than the films with smaller grains. Figure 4.5(c) shows that, for films grown on Cu substrates, the more ordered the film, the higher the upper critical field; as in Figure 4.5(a), the outlying data point is the film grown on sapphire.

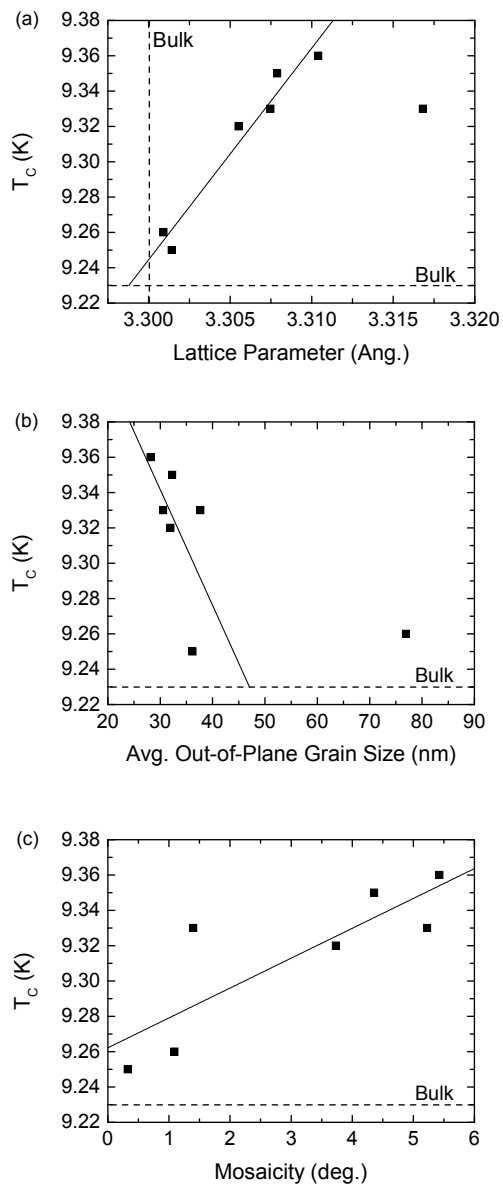


FIG. 4.3: Correlation between  $T_C$  and (a) lattice parameter, (b) average out-of-plane grain size, and (c) mosaicity. Dashed lines indicate bulk values, also given in Table 4.2; solid lines are linear fits of the data.

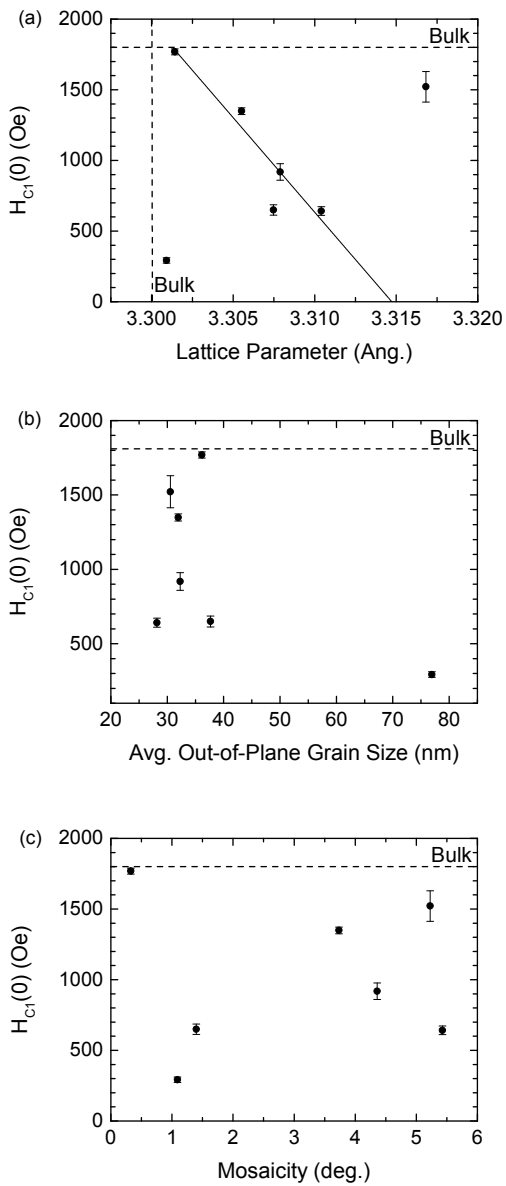


FIG. 4.4: Correlation between  $H_{C1}(0)$  and (a) lattice parameter, (b) average out-of-plane grain size, and (c) mosaicity. Dashed lines indicate bulk values, also given in Table 4.2; the solid line in (a) is a linear fit of the data.

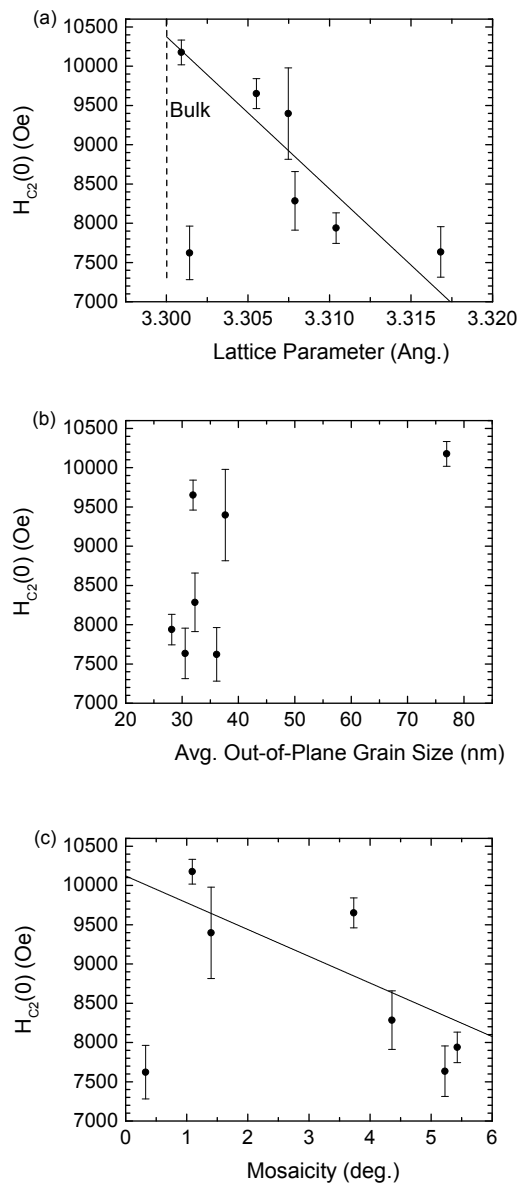


FIG. 4.5: Correlation between  $H_{C_2}(0)$  and (a) lattice parameter, (b) average out-of-plane grain size, and (c) mosaicity. The dashed line in (a) indicates the bulk lattice parameter given in Table 4.2, while the bulk value of  $H_{C_2}(0)$  itself, given in Table 4.2, is below the range of the plots; solid lines are linear fits of the data.

### 4.1.3 Conclusions

In this study, we correlate  $T_C$ ,  $H_{C1}(0)$ , and  $H_{C2}(0)$  with the lattice parameter, average out-of-plane grain size, and mosaicity of Nb films grown on r-Al<sub>2</sub>O<sub>3</sub> and a variety of Cu substrates. All of the films studied, regardless of the surface on which they were grown, had a  $T_C$  higher than that of bulk Nb; in order to enhance this further, Nb films need small, disordered grains, and slightly strained lattice parameters. For more bulk-like  $H_{C1}$  values, however, the films must have a lattice parameter close to bulk and relatively small, well-ordered grains. These trends, combined with studies further correlating these properties with RF superconducting behavior, can be used in future film growth to attempt to produce films with specific superconducting properties for applications such as detectors and SRF cavity coatings by balancing the need for a higher  $T_C$  or  $H_{C1}$ .

## 4.2 Correlation Between Microstructure and Electronic Properties of Niobium Thin Films

### 4.2.1 Introduction

As discussed in Section 2.2.3, when a superconductor enters the superconducting state, an energy gap of  $2\Delta$  opens around the Fermi energy; this superconducting gap is related to the critical temperature of the material through BCS theory (Equation 2.25), and is also related to the coherence length  $\xi$  of the Cooper pairs in a superconductor via the Ginzburg-Landau theory (Equation 2.29). It should thus be possible to extract information about these fundamental electronic properties of a superconductor from  $T_C$  measurements such as those performed in the study presented in Section 4.1. To that end, a series of SQUID measurements were carried out on a second set of Nb thin films provided by Dr. A.-M.

Valente-Feliciano; the superconducting gaps of these films have already been measured via point contact tunnelling (PCT) [99, 100], which provides a standard value for comparison [101].

### 4.2.2 Sample Characterization

Five of the films studied were grown on large-grained Cu substrates; one other film, which was included in the study in Section 4.1 (Sample Cu-fg-124), was grown on fine-grained Cu. All films were characterized via XRD and SQUID magnetometry as described in Section 4.1.2, although  $H_{C1}$  measurements on the five new films were taken at only 2, 4, and 8.9 K due to a limited liquid helium supply. All of the films displayed relatively poor  $H_{C1}$  values; atomic force microscopy (AFM) showed, however, that the surfaces of these films were generally rougher than the films considered in the previous study, and visual inspection of the surfaces indicated the possible presence of surface contamination, both of which will decrease the measured  $H_{C1}$  values.  $T_C$ , however, is a bulk property of a material and will not be as strongly affected by surface defects as  $H_{C1}$ , so those measurements are still valid and can be used to examine the superconducting gap of the films.

### 4.2.3 Superconducting Gap Calculations

Using the BCS-predicted relationship of  $\Delta = 1.76k_B T_C$ , we calculated the superconducting gap of each film at 25 Oe (the applied field used during the  $T_C$  measurements), but still needed to account for the effect of the applied field. To do so, we applied a result from Ginzburg-Landau theory that equates the superconducting gap at some field  $H$  to the zero-field gap [102]:

$$\frac{\Delta(H)}{\Delta(0)} = \sqrt{1 - \left(\frac{H}{H_C}\right)^2}. \quad (4.3)$$

Our corrected gap values had a percent error of between 8.1% and 17.1% from the previously-measured values [101], but this is not unexpected, as we used a theory developed for an ideal bulk superconductor, not for thin films with varying microstructure and inherent defects. In fact, we found that the percent error in our calculations increased linearly with both increasing lattice parameter above bulk and mosaicity, providing further evidence that the less bulk-like the film, the less agreement there is with the BCS calculation of  $\Delta(0)$ .

The fact that the BCS relationship between  $T_C$  and  $\Delta(0)$  does not hold for thin films does not necessarily imply that the two quantities cannot be equated; to see if it was still possible to do so, we calculated  $\Delta(0)/(k_B T_C)$  for each of the films, where  $\Delta(0)$  was the PCT-measured value and  $T_C$  was taken from our SQUID measurements. It was found that this ratio was close to 2 for all six films, with an average value of

$$\Delta(0) = 2.04k_B T_C . \quad (4.4)$$

This result is in excellent agreement with the value of 2.05 found by Pronin *et al.* for another Nb film [103].

We can extend this analysis by applying Equation 4.4 to the films examined in Section 4.1. The values calculated for these films were again adjusted to account for the 25 Oe field applied during the  $T_C$  measurement; the corrected values are presented in Table 4.3, along with the  $T_C$  and  $H_{C1}$  values from Table 4.2 used in the calculations.

#### 4.2.4 Structure-Property Correlations

We can correlate the electronic behavior of these films with their microstructure as we did in Section 4.1.2. The superconducting gap at 25 Oe of course follows exactly the same trends with microstructure as does  $T_C$  (Figure 4.3), but the zero-field gap displays slightly

TABLE 4.3: Zero-field superconducting gap values calculated using Equations 4.4 and 4.3.

Sample ID	$T_C$ (K)	$H_{C1}(0)$ (Oe)	$\Delta(0)$ (meV)
r-Al <sub>2</sub> O <sub>3</sub>	9.25	1769±21	1.626 ±(3.9×10 <sup>-6</sup> )
Cu-fg-124	9.36	641±31	1.646 ±(1.2×10 <sup>-4</sup> )
Cu-LG-124	9.26	293±19	1.634 ±(7.7×10 <sup>-4</sup> )
Cu-fg-141	9.25	918±59	1.645 ±(8.1×10 <sup>-5</sup> )
Cu-LG-141	9.32	1349±24	1.638 ±(9.8×10 <sup>-6</sup> )
Cu-110-108-5	9.33	1521±108	1.640 ±(3.1×10 <sup>-5</sup> )
Cu-111-108-5	9.33	649±37	1.641 ±(1.4×10 <sup>-4</sup> )

different correlations due to the effect of the  $H_{C1}$  of each film (Equation 4.3). These correlations, shown in Figure 4.6, are still linear, though, and do still indicate similar relationships between the microstructure and the zero-field, zero-T gap:  $\Delta(0)$  increases linearly as the lattice parameter and mosaicity of the films increase, and decreases with increasing out-of-plane grain size. The outlying data points in Figure 4.6(a) and (b) are the same as those in Figure 4.3(a) and (b) and are discussed in Section 4.1.2.

The coherence length of the Cooper pairs in a superconductor is inversely related to the superconducting gap, so the correlation of  $\xi$  and the microstructure follows the inverse of the relationships shown in Figure 4.6. We note that the relationship between grain size and the coherence length - decreasing coherence length with decreasing grain size - agrees with previous reports for Nb as well as other superconducting thin films [104, 105].

### 4.2.5 Conclusions

We have demonstrated that the BCS relationship between  $\Delta(0)$  and  $T_C$  does not exactly hold in superconducting thin films due to the non-bulk-like nature of the material. It is however still possible to relate those quantities, and our result of  $\Delta(0) = 2.04k_B T_C$  is in very good agreement with previous work on Nb films [103]. Using this relationship, we

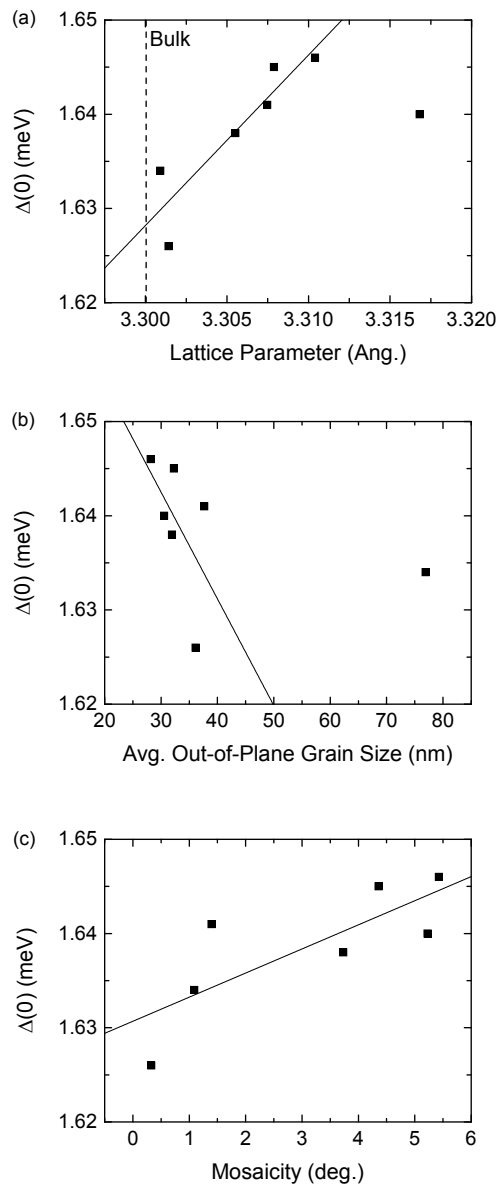


FIG. 4.6: Correlation between  $\Delta(0)$  with zero applied field and (a) lattice parameter, (b) average out-of-plane grain size, and (c) mosaicity. The dashed line in (a) indicates the bulk lattice parameter of Nb; solid lines are linear fits of the data.

are able to observe trends in the fundamental electronic properties of a superconductor - namely  $\Delta(0)$  and  $\xi$  - with changing microstructure, in good agreement with literature. This information, especially when combined with the results of the previous study on several of these films (Section 4.1), provides greater understanding of the effects of a superconducting thin film's microstructure on its superconducting behavior without necessarily having to directly measure every quantity of interest.

## 4.3 Comparison of $H_{C1}$ Measurements on Superconducting Niobium Thin Films

### 4.3.1 Introduction

The lower critical field in Type II superconductors is key to characterizing the behavior of devices using coatings made of well-known superconductors [15, 21, 106], as well as to obtaining bulk thermodynamic information of new high- $T_C$  superconductors [107–109].  $H_{C1}$  measurements made via SQUID (superconducting quantum interference device) magnetometry are extremely sensitive to both system geometry and sample alignment [110], and as such have not been considered reproducible across different systems. Here we present  $H_{C1}$  values for niobium thin films as determined by two distinct methods from SQUID magnetometry performed at the College of William & Mary and compare them to values also measured via SQUID at the University of Leuven as well as to a measurement via VSM/SQUID from the University of Geneva/CERN. We first show the importance of accounting for trapped magnetic flux and substrate effects in SQUID data and that the traditional method of determining  $H_{C1}$  from SQUID is in fact not the most accurate. We then proceed to show that, as long as proper care is taken to account for these effects,  $H_{C1}$  measurements are reproducible to within 10%, regardless of the instrumentation used.

### 4.3.2 Experimental Details and Methods

#### Sample Preparation

Both films studied were prepared at the SRF Institute at Thomas Jefferson National Accelerator Facility via electron cyclotron resonance (ECR) [73, 74]. Sample 134 is  $1.2 \mu\text{m}$  thick and grown on r-plane sapphire ( $\text{r-Al}_2\text{O}_3$ ) with nucleation at an ion energy of 124 eV and subsequent growth at 64 eV. Sample 124 is  $2 \mu\text{m}$  thick and grown on mechanically polished oxygen-free high thermal conductivity (OFHC) fine-grained copper (Cu) with nucleation and early growth at 184 eV and subsequent growth at 64 eV [74]; this sample was a witness sample for a coating which showed significantly improved SRF performance [111].

#### Superconducting Measurements

***William & Mary Measurements.*** A set of  $H_{C1}$  measurements at 2, 4, 6, 8, and 8.9 K were made on both samples at the College of William & Mary using a Quantum Design MPMS SQUID magnetometer. Two methods of measurement were used in order to allow for in-house confirmation of the  $H_{C1}$  values, as described in Section 3.3.2.

***University of Leuven Measurements.*** Measurements at the University of Leuven were also made using a Quantum Design MPMS SQUID magnetometer.  $H_{C1}$  values were determined using the standard M-H curve deviation method.

***University of Geneva Measurements.*** Measurements at the University of Geneva were made using a vibrating sample magnetometer with SQUID (VSM/SQUID) in parallel field configuration, in which the sample is vibrated about a fixed point in a direction parallel to the applied field. VSM/SQUID has the advantage of being able to separate the signal from the film from any magnetic effects in the substrate or sample mounting mechanism, as any field induced in those (if made from conducting materials) will be out

of phase with the signal from the sample itself.[112]

### 4.3.3 Results and Discussion

#### Comparison of SQUID Methods From a Single Instrument

At William & Mary, SQUID measurements on both samples were taken at five temperatures, all below the samples  $T_C$ , as measured there. The William & Mary M-H curves for Sample 134 ( $T_C = 9.25$  K) are shown in Figure 4.7(a); the corresponding  $H_{C1}$  values are given in Table 4.4, along with the values determined from the trapped field method described in Section 4.3.2 and the percent difference between them. Equivalent data for Sample 124 ( $T_C = 9.36$  K) are shown in Figure 4.7(b) and Table 4.5, respectively.

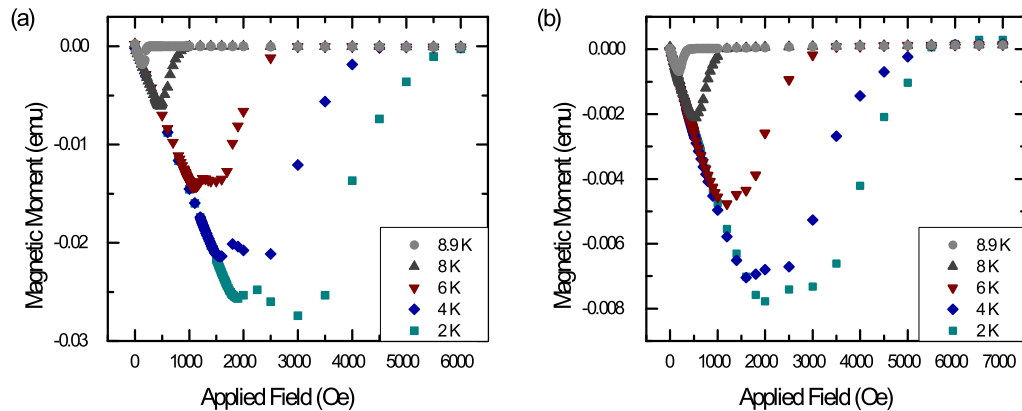


FIG. 4.7: M-H curves for (a) Sample 134 and (b) Sample 124 as measured at the College of William & Mary.

By only considering the data from Sample 134, it would appear that the two methods of determining  $H_{C1}$  are nearly equivalent - at temperatures just below  $T_C$ , the values from both the M-H and trapped field methods are identical, and at lower temperatures (2-6 K), they differ by less than 6%. However, when the data from Sample 124 is considered, we see that the values from the two methods have a much larger percent difference, with the

TABLE 4.4:  $H_{C1}$  values for Sample 134 as measured at the College of William & Mary.

Temperature	M-H Method	Trapped Field Method	Percent Difference
8.9 K	130 Oe	130 Oe	0%
8 K	435 Oe	435 Oe	0%
6 K	975 Oe	950 Oe	2.6%
4 K	1430 Oe	1350 Oe	5.8%
2 K	1720 Oe	1630 Oe	5.4%

TABLE 4.5:  $H_{C1}$  values for Sample 124 as measured at the College of William & Mary.

Temperature	M-H Method	Trapped Field Method	Percent Difference
8.9 K	80 Oe	70 Oe	11.7%
8 K	190 Oe	150 Oe	23.5%
6 K	375 Oe	300 Oe	22.2%
4 K	460 Oe	445 Oe	3.3%
2 K	650 Oe	530 Oe	20.3%

exception of the scans at 4 K, which will be discussed below. This can be attributed to the difference in the substrate used for each sample - Sample 134 was grown on sapphire, which is non-magnetic, but Sample 124 was grown on copper, which, while not magnetic itself, is susceptible to induced magnetic fields, especially at the higher fields applied. As discussed in Section 3.3.2, the trapped field method accounts for magnetic flux pinned in the superconducting film; the data presented here indicates that it also accounts for the magnetic field induced in the copper as the applied field increases. The closer agreement between the two methods at 4 K can likely be partially attributed to the time necessary to complete the measurement - cooling and warming the sample at 4 K took roughly twice as long as at other temperatures due to the cooling mechanism employed by the magnetometer, giving the magnetic field induced in the copper more time to dissipate after the applied field returned to zero.

### Comparison Between SQUID Data from Multiple Instruments

When comparing the William & Mary data for Sample 134 to the SQUID measurements made at the University of Leuven on the same sample, we primarily considered the M-H data, as that method was used at both locations. Private communication [113] about the Leuven data indicated agreement within 7.5%; most of the data in fact agreed to within less than 2%. Due to the non-magnetic nature of the substrate, we can also compare the trapped field method data to the M-H data from the University of Leuven; these data agree to within 10% [113]. While this agreement is not as close as the agreement between the two sets of  $H_{C1}$  values from William & Mary, it is important to remember that  $H_{C1}$  measurements are extremely sensitive to sample alignment; the William & Mary data for both methods were taken at the same time, removing any potential differences due to alignment.

### Comparison Between SQUID and VSM/SQUID Data

We compared the University of Geneva 2 K measurement on Sample 124 to William & Mary data from both the M-H method and the trapped field method, as shown in Figure 4.8 (a) and (b), respectively. There is a 20.3% difference between the  $H_{C1}$  value obtained at the University of Geneva (515 Oe) and the M-H William & Mary data (650 Oe), while the trapped field method (530 Oe) shows much better agreement - there is only a 2.9% difference between the two values. This further supports the above discussion regarding the use of the trapped field method in SQUID measurements, although the slightly higher  $H_{C1}$  value from the trapped field SQUID data may indicate that this method does not completely remove the effects of magnetic response from the substrate. Even so, by accounting for the effects of trapped flux in the thin film sample itself and the majority of the induced magnetic field in the substrate, it is possible to obtain an  $H_{C1}$  value that

is reproducible by a completely different measurement technique.

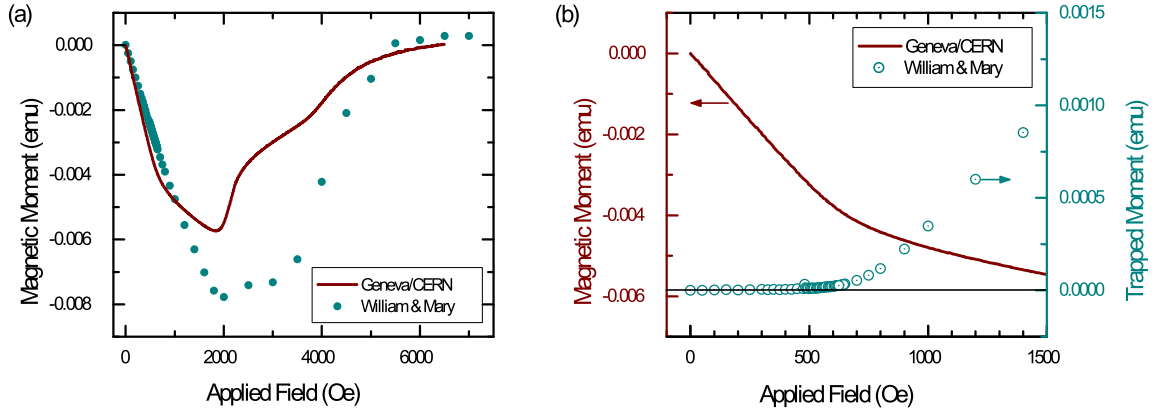


FIG. 4.8: Comparison of VSM/SQUID data from the University of Geneva (thick solid line) and SQUID data via the (a) traditional M-H method (solid dots) and (b) trapped field method (right axis, circles with centered dots) from the College of William & Mary. The thin horizontal line at 0 emu on the right axis in (b) indicates zero trapped field; deviation from this line occurs at  $H_{C1}$ .

#### 4.3.4 Conclusions

The SQUID data from William & Mary presented here shows that, particularly when a film is grown on a substrate with a magnetic response, the trapped field method for determining  $H_{C1}$  in thin films, as outlined in Bohmer *et al.* [88] is more accurate than the traditional M-H method. Simply looking for the point at which the magnetization deviates from the Meissner slope does not account for flux trapped within the film nor for any induced magnetic response in the substrate, even if it is itself not inherently magnetic. While we have shown that traditional M-H data can be reproduced on different SQUID instruments to within 10%, both trapped flux and substrate effects can falsely increase  $H_{C1}$ , making the measurements seem unreliable when comparing to measurements made using other instrumentation, such as VSM/SQUID. The reported agreement of only 2.9% difference between the VSM/SQUID data and the trapped field SQUID data again

indicates that use of the trapped field method - with careful sample alignment - gives a more accurate and highly reproducible  $H_{C1}$  value.

## 4.4 Stoichiometry and Thickness Dependence of Superconducting Properties of Niobium Nitride Thin Films

### 4.4.1 Introduction

As discussed in Section 1.1.1, the current technology used in linear particle accelerators is based on superconducting radio frequency (SRF) cavities fabricated from bulk Nb, which have smaller surface resistance and therefore dissipate less energy than traditional non-superconducting copper cavities. These cavities, however, have a material-dependent accelerating gradient limit (50 MV/m, due to the lower critical field of bulk Nb,  $H_{C1} = 1800$  Oe [3]); in order to overcome this fundamental limit, two types of cavity coatings discussed in Section 1.1.2 have been proposed [16, 19, 20]. The second of these methods uses the well-known critical field enhancement seen in superconducting films thinner than their London penetration depths in a parallel field geometry; this is relevant primarily because a thermodynamically stable vortex scenario with strong RF vortex dissipation exists for films thicker than the London penetration depth, which would compromise the proposed screening of the SIS coating. In such thin films,  $H_{C1}$  is given by

$$H_{C1} = \frac{2\Phi_0}{\pi d^2} \ln \left( \frac{d}{1.07\xi} \right), \quad (4.5)$$

where  $\Phi_0$  is the magnetic flux quantum,  $d$  is the film thickness, and  $\xi$  is the coherence length of the material; this relationship has recently been demonstrated experimentally in MgB<sub>2</sub> thin films [21].

Here, we consider NbN films for use in this type of coating and discuss the relationship between film stoichiometry and superconducting properties, as well as the thickness dependence of those properties. NbN is an ideal candidate for the SIS model - its critical field  $H_C$  (2300 Oe) is higher and its  $T_C$  (16.2 K) is nearly twice that of Nb [3] - and previous work [22] has demonstrated that such layered structures using NbN are in fact capable of shielding underlying bulk Nb [72]. A few studies have explored the relationship between stoichiometry and critical temperature  $T_C$  [114–118], but until this work was published in Reference [15], there had been no careful study of the correlation between stoichiometry and  $H_{C1}$  in NbN thin films.

#### 4.4.2 Film Growth and Characterization

NbN films were prepared using reactive DC magnetron sputtering in a high-vacuum system with base pressures in the range of  $10^{-7}$  Torr. Deposition was carried out using a 99.95%-purity Nb target; all films were grown on commercially-available MgO(100) substrates in order to emulate the insulating layers of the SIS model. We note that due to the favorable lattice matching between NbN and the chosen substrate, all of the films grew epitaxially with only the superconducting  $\delta$  phase present. We also note that one sample was capped with a thin (5 nm) gold overlayer to observe the effect of a protected and/or smoother surface on the DC superconducting properties of the film. After growth, the films were characterized *ex situ* with XRD and SQUID magnetometry.

### 4.4.3 Results and Discussion

Table 4.6 lists the lattice parameters, average grain size, and mosaicity measured for the NbN films as well as the corresponding  $T_C$  and  $H_{C1}$  values, ordered from smallest lattice parameter to largest. Highlighted rows are films that showed an enhanced  $H_{C1}$  compared to bulk; the films highlighted in light gray have a lattice parameter between 4.38 Å and 4.39 Å, which was considered an optimal range based on the bulk NbN lattice parameter (4.395 Å). A high-angle  $2\theta$ - $\omega$  scan for the 80 nm film, with lattice parameter 4.388 Å, is shown in Figure 4.9. This scan is representative of all films highlighted in light gray.

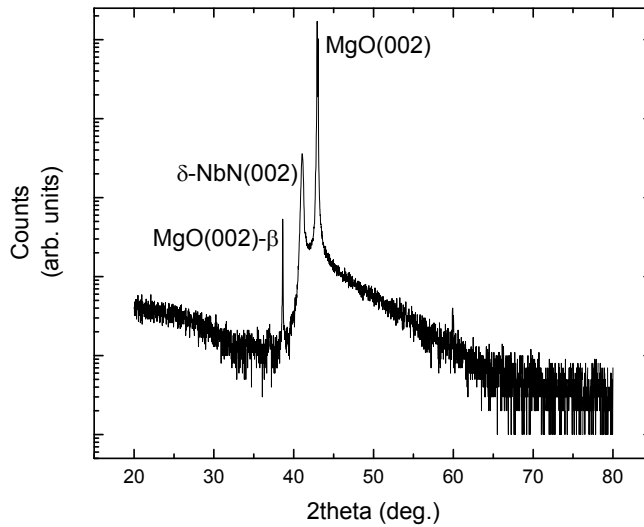


FIG. 4.9: High-angle  $2\theta$ - $\omega$  scan for the 80 nm NbN sample on MgO(100).

We note here that although the 378 nm film (denoted both in Table 4.6 and the following figures by a star) was grown to approximate bulk conditions with a thickness greater than the London penetration depth of NbN ( $\lambda_L = 200$  nm), it still showed a slight critical

TABLE 4.6: Thickness, microstructural information, and superconducting properties of the films studied here, as well as the corresponding bulk values. Bulk lattice information is from Reference [72], while superconducting properties are from Reference [3].

Sample Thickness (nm)	d (Å)	Grain Size (nm)	Mosaicity	$T_C$ (K)	$H_{C1}$ (Oe)
36	4.349	13.123	1.428	10.98	76
120	4.357	27.754	1.117	9.6	140
121 + 5 Au	4.361	23.829	0.981	13.2	1600
85	4.379	27.507	1.417	13.72	500
378★	4.382	32.979	0.702	10	230
150	4.385	27.710	0.946	14.55	270
100	4.387	33.877	0.790	14.24	350
120	4.388	32.126	0.868	14.75	950
80	4.388	32.128	0.868	14.63	1000
60	4.391	28.586	0.857	14.55	700
<b>Bulk</b>	<b>4.395</b>	–	–	<b>16.2</b>	<b>200</b>

field enhancement from the expected bulk value, perhaps due to some underlying remnant strain. The sample highlighted in dark gray showed the best field enhancement - an increase over bulk of 1400 Oe, 450 Oe more than an uncapped sample of comparable thickness - likely due to the gold overlayer. In addition to protecting the surface from further degradation after exposure to ambient conditions, such an overlayer has been predicted to smooth out surface roughness, which would lead to improved DC superconducting performance by minimizing magnetic field pinning sites [16]. This result is encouraging, although an alternative capping layer must be considered in order to also offer SRF advantages.

We can now explore the relationship between microstructure and the superconducting properties of films with comparable lattice parameter, i.e. between 4.38 Å and 4.39 Å, and consider the  $H_{C1}$  enhancement as a function of film thickness. Figure 4.10(a) shows the  $H_{C1}$  enhancement predicted by Equation 4.5 over the range of film thicknesses given in Table 4.6, with a coherence length of  $\xi = 4$  nm [3]. Figure 4.10(b) plots the measured  $H_{C1}$  for the films, with the theoretical curve shifted to show that, while the enhancement appears

reduced with respect to the theoretical prediction, it still roughly exhibits the expected trend. The measured  $H_{C1}$  values are lower than the calculated values because, while theory assumes perfect bulk-like material, epitaxial thin films exhibit strain and other defects due to lattice mismatch with the substrate and the specific growth mode that follows the early nucleation stage, as discussed in Section 3.1. Additionally, as mentioned in Section 3.3.2, the  $H_{C1}$  values measured are underestimates due to the geometric constraints of DC SQUID measurements, since perfect alignment of the film surface and the applied field is experimentally very difficult to achieve. In addition, these measurements are also very surface-sensitive, thus the use of a capping overlayer as discussed above improves DC performance as indeed we observed.

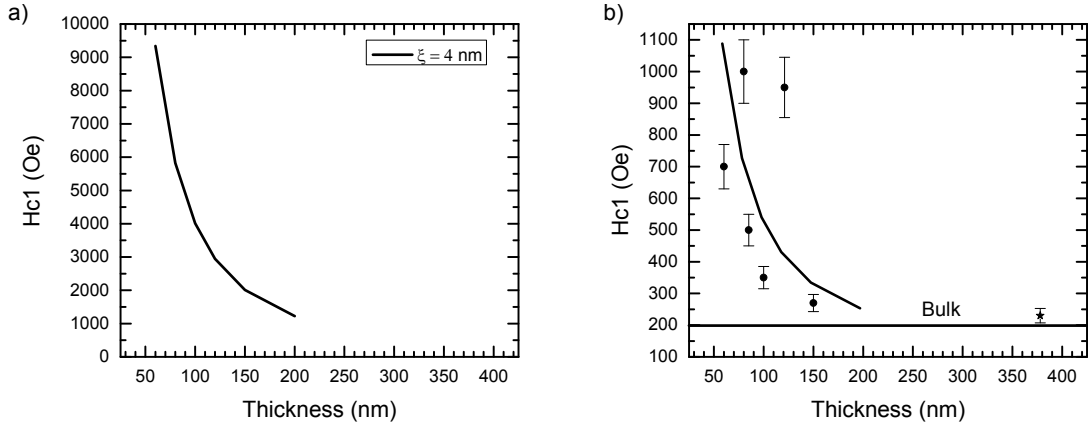


FIG. 4.10: (a) Calculated predicted lower critical field ( $H_{C1}$ ) enhancement for NbN thin films, with a coherence length of  $\xi = 4$  nm. (b) Actual  $H_{C1}$  values for the films considered here, with the theoretical curve shifted to show that the films fit the trend. The  $H_{C1}$  for bulk NbN, 200 Oe, is marked with a solid black line.

We can also look at the critical temperature,  $T_C$ , as a function of lattice parameter and film thickness. As seen in Figure 4.11(a), there is a linear relationship between  $T_C$  and the lattice parameter; this agrees well with the trend seen for the same range in lattice parameters as reported by Wang *et al.* and Wolf *et al.* [114, 115]. Figure 4.11(b) shows

that there is no clear relationship between  $T_C$  and film thickness; this is unsurprising, as  $T_C$  is a bulk property, i.e. for a given stoichiometry,  $T_C$  does not depend on the thickness of the sample, as demonstrated in Bacon *et al.* [118]. The large difference in the  $T_C$  of the 378 nm sample (again, denoted by a star) is likely due to increased strain-related film defects that have propagated throughout the entire thickness of the film. Similar effects were again seen by Bacon *et al.*, and this conclusion is further supported by the sample structure - although the lattice parameter in this sample is within the accepted range for this study, it is somewhat low for such a thick film, which should have achieved a lattice parameter closer to the bulk value [118].

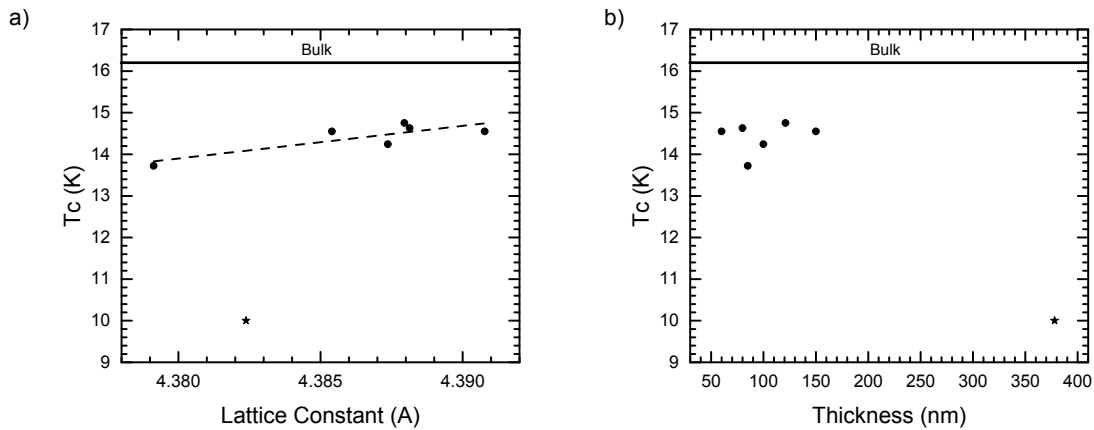


FIG. 4.11: Critical temperature,  $T_C$ , as a function of (a) lattice constant and (b) thickness. The bulk value,  $T_C = 16.2$  K, is shown as a solid black line. In (a), the linear trend is indicated by the dashed fit line.

Another microstructure property that can be correlated to  $H_{C1}$  and  $T_C$  is the grain size, as calculated from the full-width-half-maximum (FWHM) of the NbN  $2\theta-\omega$  XRD scans. This is plotted in Figure 4.12, with bulk values again shown as solid black lines. Both  $H_{C1}$  and  $T_C$  (Figures 4.12(a) and 4.12(b), respectively) increase linearly with increasing grain size, which is expected due to less electron scattering from inter-grain boundaries. As mentioned previously, the sample with  $T_C \approx 10$  K is fairly thick and potentially has

more structural defects, decreasing its superconducting performance.

We also considered the effects of the mosaicity, or amount of disorder in the crystal grains, of the films on their superconducting properties, but found no strong correlations. In this case, the size of the grains appears to be of greater importance than their ordering.

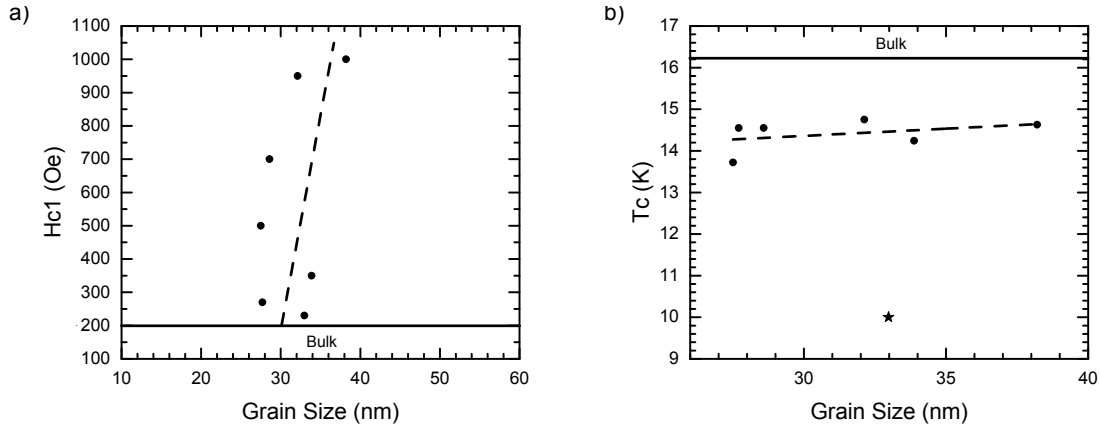


FIG. 4.12: (a) Critical field,  $H_{C1}$  and (b) critical temperature,  $T_C$  as a function of grain size.

#### 4.4.4 Conclusions

The results presented here agree with previous reports indicating that good stoichiometry in general yields a linear trend between lattice parameter of NbN thin films and DC superconducting properties. When the lattice parameter is controlled, the expected  $H_{C1}$  enhancement for films with thickness below the London penetration depth is also observed. This information enables the prediction of the quality of future NbN thin films grown under similar conditions and the tailoring of such films for their use in the proposed SIS multilayer structures.

## 4.5 Correlation Between Microstructure and Electronic Properties of Niobium Nitride Thin Films

### 4.5.1 Introduction

Section 2.2.2 discussed the importance of the surface resistance  $R_{surf}$  of superconducting films, and showed that it is in fact proportional to the normal-state conductivity (Equation 2.24) of the material. The previous study showed the effect of film thickness and microstructure on the DC superconducting properties of several NbN thin films, and here we extend that correlation to electronic properties, including the conductivity and therefore the surface resistance, of the films.

### 4.5.2 Four Point Probe Measurements and Calculations

Five NbN films covering a range of thicknesses - 60, 80, 100, 120, and 150 nm - were chosen from the samples studied in Section 4.4; information about their structural characterization can be found therein. Using a Veeco FPP 500 Four Point Probe, the sheet resistance  $R_S$  of each film was measured five times, each measurement in a different location on the film, in order to obtain an average value. A correction factor, calculated according to the method in [119], was then applied to each average to account for the size and shape of each film. It should be noted here that the film surfaces were assumed to be a uniform 1 cm  $\times$  0.5 cm, although each film has an actual surface area slightly less than that due to surface masking at one end during growth; this masking, though, has a negligible effect on the sheet resistance calculation, as even a 20% reduction in length only reduces the correction factor by 1%.

In the limit of a thin film, the resistivity  $\rho$  can be calculated by

$$\rho = R_{st}, \quad (4.6)$$

where  $t$  is the film thickness [120]; the conductivity  $\sigma$  (denoted as  $\sigma_n$  in Section 2.2.2) is then simply given by the standard equation  $\sigma = 1/\rho$ . The masking effect described above may have a slight effect on  $\rho$ , as we cannot be sure that the film is of a uniform thickness at the edge of the masked area, but the majority of the film will have thickness  $t$ .

### 4.5.3 Results and Discussion

The electrical properties measured for each film are summarized in Table 4.7. There is a clear thickness dependence for the sheet resistivity of the films that, interestingly, as shown in Figure 4.13, follows much the same trend as does the  $H_{C1}$  enhancement seen in thin superconducting films; such a trend is consistent with previous reports on the surface resistance of thin films [120]. The values for total resistivity are in good agreement with literature reports on similar NbN films [114, 121], but do not exhibit a similar trend with thickness (Figure 4.13 inset), contrary to previously-reported results [114]. Examination of the effects of the microstructure on the electrical properties of the films may, however, explain this discrepancy.

Figure 4.14 shows the conductivity (the inverse of resistivity) of the films with respect to their (a) average out-of-plane grain size and (b) mosaicity. In both cases, there is a clear linear relationship between the microstructure and the conductivity, highlighting the important role grain boundaries play in determining the electrical properties of a film. It is well-known that more grain boundaries leads to more electron scattering, making it harder for electrons to travel through a material [120], thus a film with many small grains will have a lower conductivity. The mosaicity of a film has an even stronger effect on conductivity

TABLE 4.7: Electronic properties for the five films studied here.

Sample Thickness (nm)	$R_S$ ( $\Omega/\square$ ) <sup>a</sup>	$\rho$ ( $\Omega$ m)	$\sigma$ (S/m) <sup>b</sup>
150	5.925	$8.888 \times 10^{-7}$	$1.125 \times 10^6$
120	6.937	$8.394 \times 10^{-7}$	$1.191 \times 10^6$
100	7.235	$7.235 \times 10^{-7}$	$1.382 \times 10^6$
80	9.086	$7.269 \times 10^{-7}$	$1.378 \times 10^6$
60	13.777	$8.266 \times 10^{-7}$	$1.210 \times 10^6$

<sup>a</sup> The unit  $\Omega/\square = \Omega/\text{square}$  is independent of length unit. It can also be written simply as  $\Omega$ , although convention dictates the use of  $\Omega/\square$ .

<sup>b</sup> The siemens (S) is the SI unit for conductance;  $1 \text{ S/m} = 1 \Omega^{-1} \text{ m}^{-1}$ .

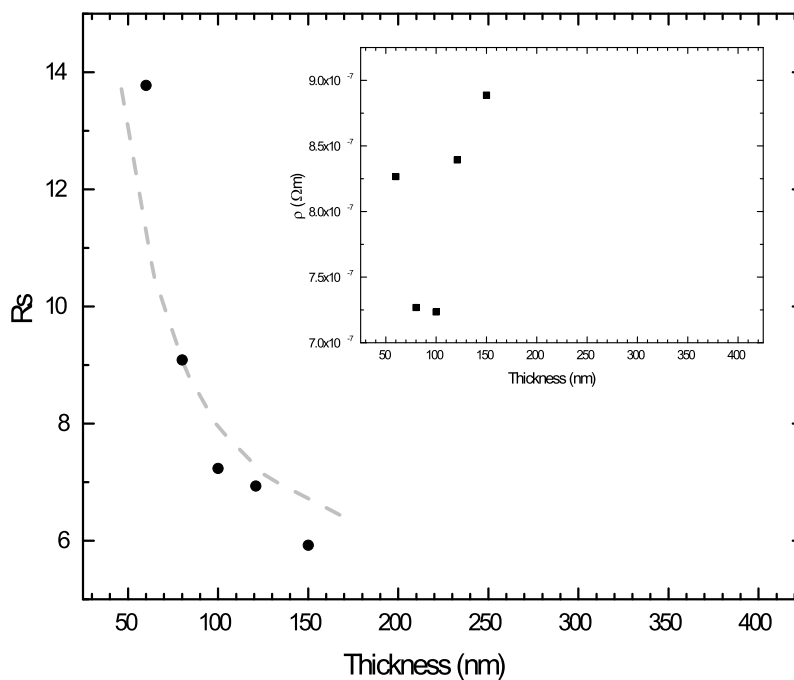


FIG. 4.13: Sheet resistance  $R_S$  of the five films studied here as a function of thickness. The light gray dashed line is the  $H_{C1}$  enhancement shown in Figure 4.10, shifted to indicate the similar trend appearing here. Inset: Resistivity  $\rho$  of the films as a function of thickness.

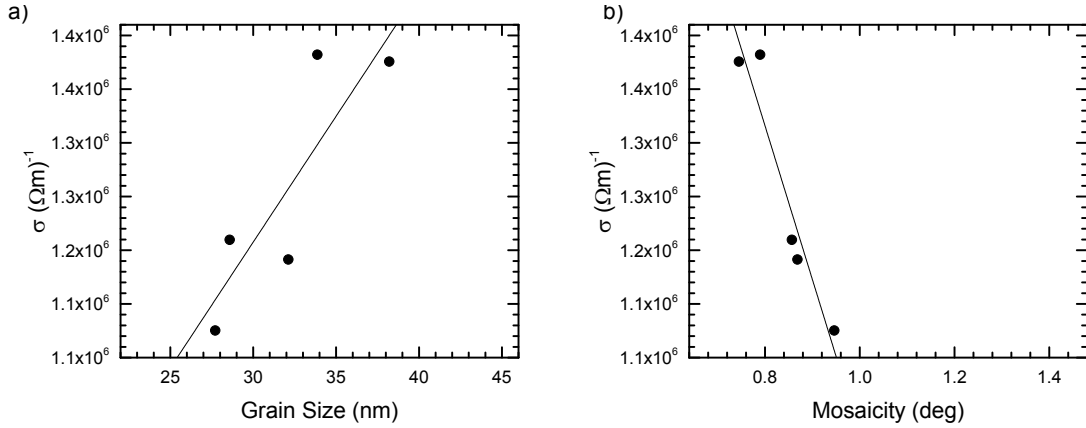


FIG. 4.14: Conductivity  $\sigma$  of the five films studied as a function of (a) grain size and (b) mosaicity.

than does grain size - the linear fit of the mosaicity data displays a correlation coefficient  $|r| = 0.96$ , as compared to 0.86 for the grain size data. By a similar grain boundary argument, more disorder among the grains in a film will increase the resistivity/decrease the conductivity.

#### 4.5.4 Conclusions

For superconducting films to exhibit the smallest superconducting surface resistance  $R_{surf}$  (Equation 2.24) possible, they need small, disordered grains, which goes against the trends seen between microstructure and DC superconducting performance in the previous study. There, it was observed that, while mosaicity has no strong effect on  $T_C$  or  $H_{C1}$  in NbN films, small grains resulted in a slightly lower  $T_C$  and a heavily-depressed (although still greater than bulk)  $H_{C1}$ . Selecting the ideal microstructure for NbN cavity coatings will therefore require a careful balance between the surface resistance and the desired lower critical field. For SIS multilayer structures, this could require the outer superconducting layer (the layer with its surface on the interior of the cavity) to have a completely different

microstructure than the lower superconducting layers (the layers closer to the bulk Nb cavity) - small disordered grains in the outermost layer to reduce the surface resistance, but larger grains on the inner layers to further enhance the lower critical field and better shield the bulk Nb cavity.

## CHAPTER 5

# Insulator-to-Metal Transitions in Niobium Compound Thin Films

## 5.1 Optically-Induced Insulator-to-Metal Transition in Niobium Dioxide and Vanadium Dioxide Thin Films

### 5.1.1 Introduction

There is a great deal of interest in light-material interactions for applications such as ultrafast optical switches for telecommunication [122], optical limiters [123, 124], and other optoelectronic devices [125]. Because constrained geometries have profound effects on many physical properties in materials, thin films are a popular choice for these types of applications. In particular, vanadium dioxide ( $\text{VO}_2$ ) thin films used as optical switches have garnered recent attention, due in part to their large change in optical conductivity - 2 orders of magnitude [126, 127] - and even larger change in DC conductivity - at least 4 to

5 orders of magnitude [128, 129]. Additionally, in 2004, Cavalleri *et al.* [34] demonstrated that the light-induced transition from the insulating to the metallic phase, initiated by hole photo-doping into the valence band with a visible laser, exhibited extremely fast switching speeds ( $<100$  fs) [29] at very low switching energies (on the order of  $1 \text{ pJ}/\mu\text{m}^2$ ) [130]. However, it was also observed that such films typically exhibited longer recovery time back to the insulating state ( $>20$  ns) [131], hindering applications requiring faster ON/OFF/ON transitions.

A related material, niobium dioxide ( $\text{NbO}_2$ ), may offer a solution. Both materials undergo an insulator-metal transition (IMT) at a material-dependent critical temperature, 340 K in  $\text{VO}_2$  and 1080 K in  $\text{NbO}_2$ . This large difference in critical temperature may indicate advantageous differences in  $\text{NbO}_2$ , but this material has not been studied nearly as extensively as  $\text{VO}_2$ . There is well-documented work on the electrically- and thermally-induced IMT in  $\text{NbO}_2$  [43–46], but, while some work has been done recently on the electronic and optical properties [9, 42], the optically-induced IMT had not been demonstrated in  $\text{NbO}_2$  until this work was published in Reference [11]. In what follows, we describe our ultrafast pump-probe studies on  $\text{NbO}_2$  thin films, which show that not only can the IMT in  $\text{NbO}_2$  be induced optically, but also that the fluence needed to drive the transition at room temperature is lower and the recovery time is much faster than for  $\text{VO}_2$ , thus enabling additional possibilities for ultrafast optical switching applications. Furthermore, the results presented here offer information that could help untangle the mystery of the mechanism behind the IMT in highly correlated materials such as  $\text{VO}_2$  and  $\text{NbO}_2$ .

## 5.1.2 Experimental Details

### Sample Structure

The thermally-induced IMT in  $\text{NbO}_2$ , like  $\text{VO}_2$ , is accompanied by a structural change in the lattice from a monoclinic structure at room temperature to a high-temperature rutile structure [31, 132]. The nature of this transition is the subject of significant study in both materials [133].

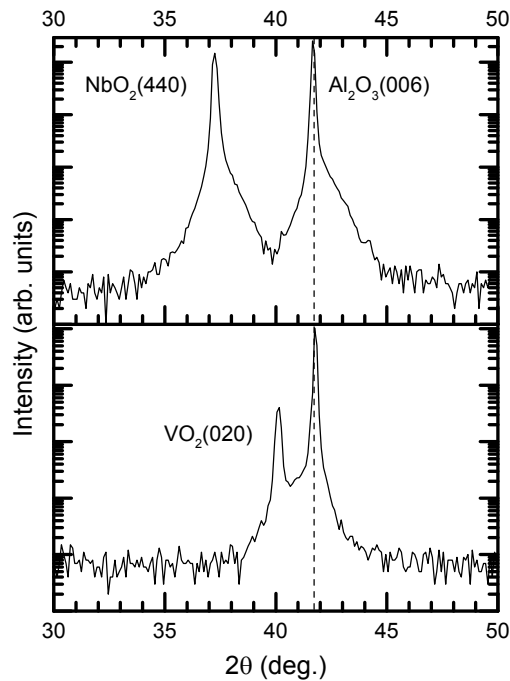


FIG. 5.1: High-angle  $2\theta$ - $\omega$  scans of the  $\text{NbO}_2$  (top) and  $\text{VO}_2$  (bottom) samples studied. The dashed line indicates the position of the bulk substrate reflection, centered at  $2\theta = 41.685^\circ$ . The  $\text{NbO}_2(440)$  peak is centered at  $2\theta = 37.223^\circ$ , while the  $\text{VO}_2(020)$  peak is centered at  $2\theta = 40.069^\circ$ .

Both the  $\text{NbO}_2$  and  $\text{VO}_2$  films studied were grown on c-plane sapphire substrates [134]. The  $\text{NbO}_2$  sample studied was 212 nm thick and covered by a 5.65 nm capping layer of  $\text{AlO}_x$  to prevent degradation [134]; the  $\text{VO}_2$  film considered was of comparable thickness

(101 nm) with no capping layer, since it was previously demonstrated that this material is robust against degradation. High-angle  $2\theta$ - $\omega$  XRD scans on the samples, shown in Figure 5.1, indicate good crystalline structure in the room-temperature monoclinic phase for both films [9, 135].

## Experimental Setup

The ultrafast laser used in these measurements is described in detail in Section 3.4.2 and shown in Figure 3.12.

## Measurements

Pump-probe measurements were made on both the NbO<sub>2</sub> and VO<sub>2</sub> samples for a relative delay of 0-2.87 ns with a fixed probe fluence of 3.2  $\mu\text{J}/\text{cm}^2$ ; full parameters for the measurements may be found in the appendix. The pump fluence was varied between scans over a range from 2.2 mJ/cm<sup>2</sup> to 422 mJ/cm<sup>2</sup> for the NbO<sub>2</sub> sample and 17.5 mJ/cm<sup>2</sup> to 422 mJ/cm<sup>2</sup> for the VO<sub>2</sub>. Higher fluences were attempted but the scans showed indications of sample damage and thus are not included here. At fluences lower than 2.2 mJ/cm<sup>2</sup>, no transition was observed in the NbO<sub>2</sub> film; in the VO<sub>2</sub> film, no transition was observed at fluences lower than 17.5 mJ/cm<sup>2</sup>, showing that a higher minimum fluence is needed to drive the transition in VO<sub>2</sub> than in NbO<sub>2</sub>.

## 5.1.3 Results and Discussion

### Experimental Results

The purely electronic component of the IMT that is photoinduced by an ultrashort optical excitation has been detected in VO<sub>2</sub> using time-resolved terahertz spectroscopy [136], IR transmittance measurements [137], and photoelectron spectroscopy (TR-ARPES) [138],

as well as in the thermally-induced IMT using electron and photoelectron spectroscopy and microscopy [139]. The detection of this metal-like monoclinic phase, indicative of an electronic IMT, enables isolation of the purely electronic response (i.e. Mott-Hubbard) from the response due to the structural IMT (i.e. Peierls) in  $\text{VO}_2$ . This same electronic component of the photoinduced IMT has been detected for the first time in  $\text{NbO}_2$ , as shown in Figure 5.2.

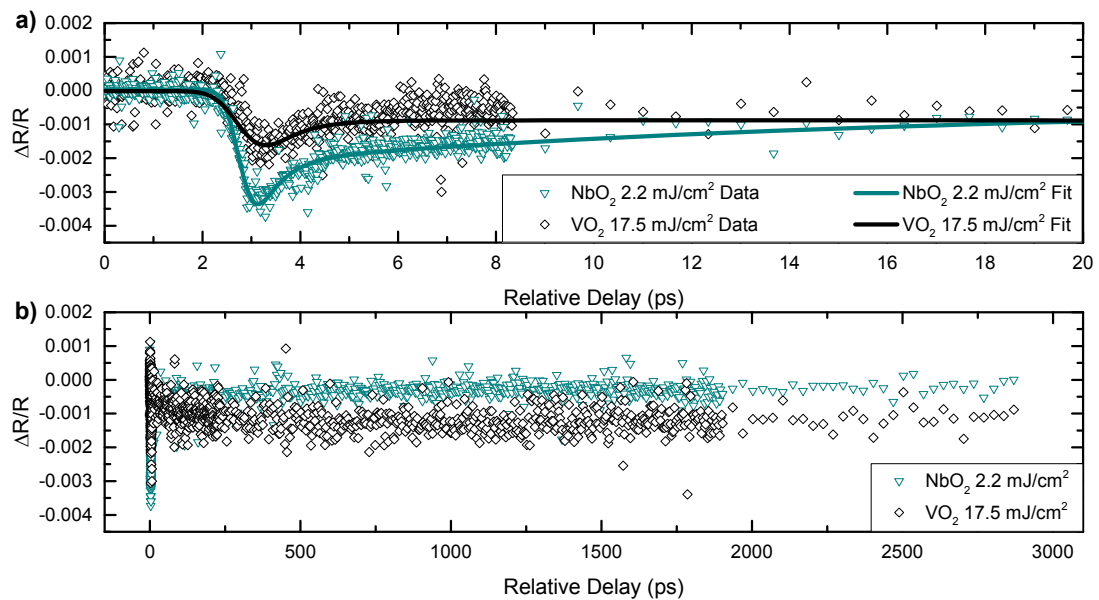


FIG. 5.2: Pump-probe measurements and fits for the lowest fluence at which the IMT was seen in each material. (a) Fitted data showing the initial response and recovery of the film. Data are plotted as disconnected points, while fits are solid lines. (b) Same as (a), but for the full 3000 ps delay.

It is important to note that the threshold for detecting the optically-induced electronic IMT, i.e. the fluence below which no change in reflectivity was seen, in  $\text{NbO}_2$  is lower (2.2 mJ/cm<sup>2</sup>) than in  $\text{VO}_2$  (17.5 mJ/cm<sup>2</sup>). Additionally, the initial fast transient response of the  $\text{NbO}_2$  is larger than that of the  $\text{VO}_2$  and remains so until a pump fluence of 70.0 mJ/cm<sup>2</sup> (Figure 5.3), at which point the thermal barrier to the structural transition in  $\text{VO}_2$  is overcome and the change in reflectance is dominated by the development of the

metallic rutile phase. This is consistent with previous studies of the ultrafast dynamics of VO<sub>2</sub> thin films that show the response of the film to varying fluences [70, 137, 140], as well as reports of chaotic behavior at the onset of the structural IMT [141], which can be seen in the non-uniform change in the VO<sub>2</sub> signal at times greater than 5 ps.

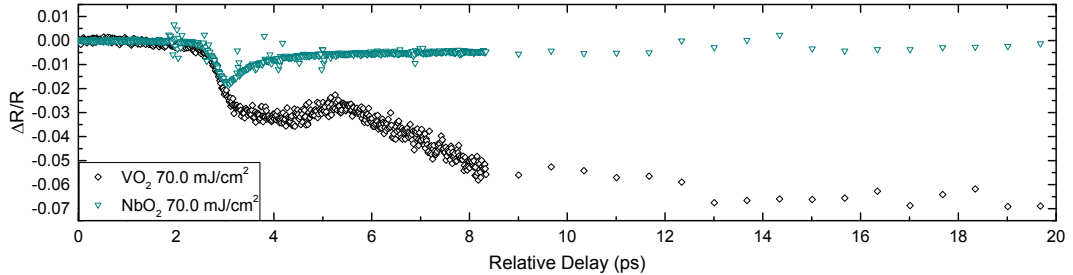


FIG. 5.3: Pump-probe measurements at a pump fluence of 70.0 mJ/cm<sup>2</sup>, when the structural transition begins in the VO<sub>2</sub> film, causing the signal to become larger than that of the NbO<sub>2</sub> film.

Four NbO<sub>2</sub> scans covering a range of pump fluences are presented in Figure 5.4 with the corresponding fit parameters listed in Table 5.1 and discussed below. In Figure 5.5, a scan at a fluence that fully transitions the VO<sub>2</sub> is presented; the associated fit parameters are also listed in Table 1. It is important to note that in VO<sub>2</sub>, the structural IMT completely dominates the response of the film such that it is not possible to detect either purely electronic processes or electron-phonon scattering processes ( $t_1$  and  $t_2$  respectively, described below). Figure 5.6 shows scans of both the NbO<sub>2</sub> and VO<sub>2</sub> films at 422 mJ/cm<sup>2</sup>, just below the damage threshold for both films, normalized to the lowest  $\Delta R/R$  for each sample. It is clear that the NbO<sub>2</sub> has a faster initial transient response ( $t_p$ ), or “turn-on” of the film’s response, than VO<sub>2</sub>. Further, the NbO<sub>2</sub> film exhibits a clear purely electronic response ( $t_1$ ) even at the highest fluence, while the response of the VO<sub>2</sub> is dominated by the optically-driven structural IMT, rendering the purely electronic IMT practically undetectable. This electronic response in the NbO<sub>2</sub> film shows a recovery of roughly 70%

within  $\sim 5$  ps at all fluences before the optically-driven structural IMT becomes evident.

While the electronic IMT has been detected at very low fluences in the optical response of  $\text{VO}_2$ , the results presented here show that a purely electronic IMT is more readily isolated from the structural IMT in  $\text{NbO}_2$  and can be detected optically. This is likely due to the higher thermal barrier to the structural IMT in  $\text{NbO}_2$ , which requires twice the fluence required in  $\text{VO}_2$  to initiate optically ( $140 \text{ mJ/cm}^2$  in  $\text{NbO}_2$ , as discussed below, compared to  $70 \text{ mJ/cm}^2$  in  $\text{VO}_2$ , as stated above).

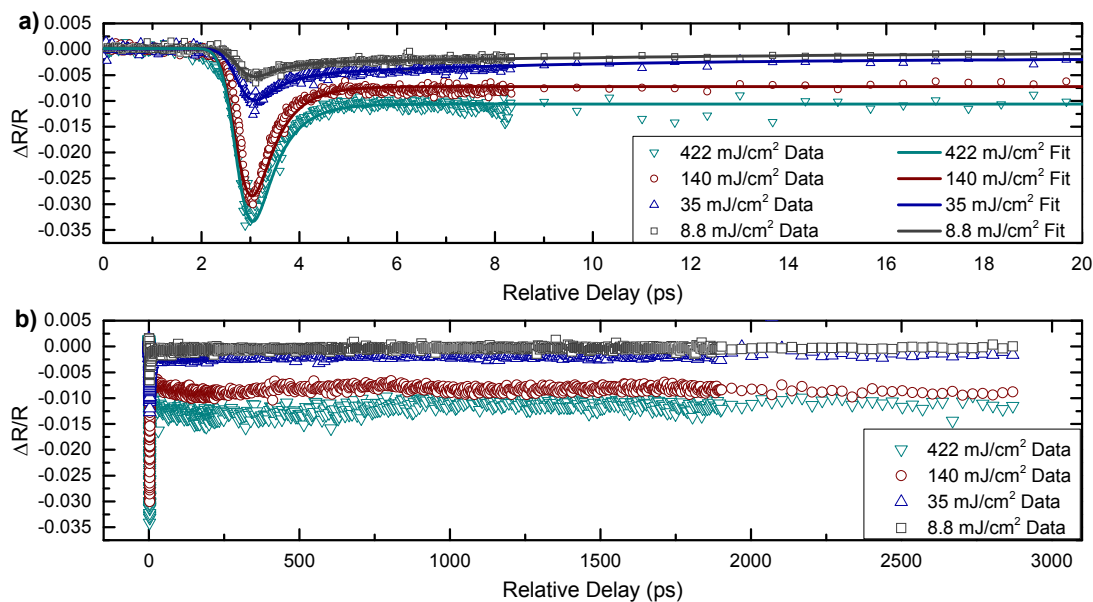


FIG. 5.4: Scans of  $\text{NbO}_2$  with pump fluences ranging from  $8.8 \text{ mJ/cm}^2$  to  $422 \text{ mJ/cm}^2$ . (a) Fitted data showing the initial response and recovery of the film. Data are plotted as disconnected points, while fits are solid lines. (b) Same as (a), but for the full 3000 ps delay.

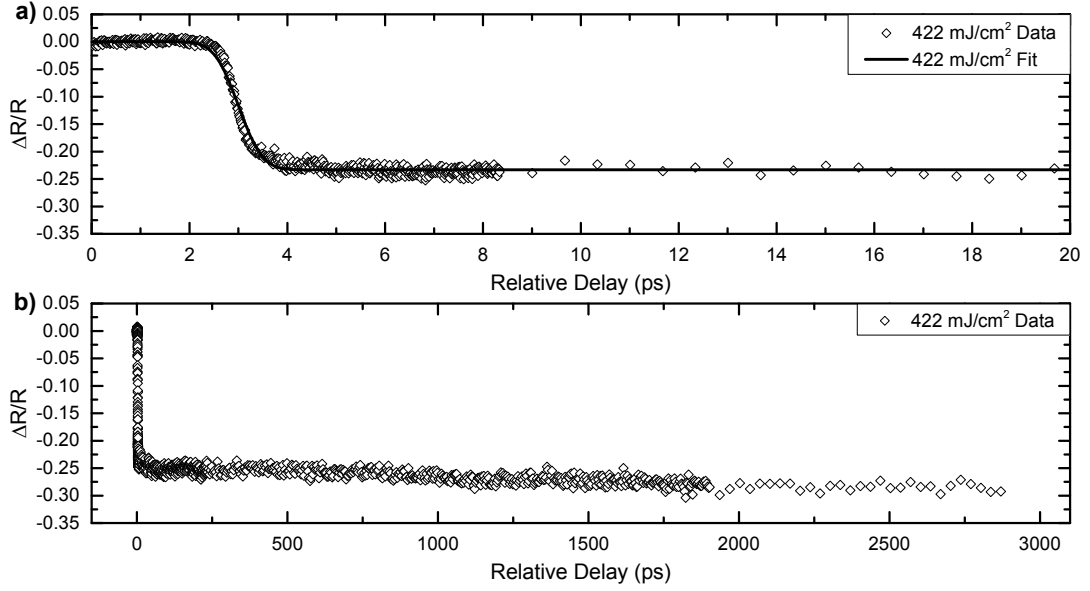


FIG. 5.5: Scan of fully-transitioned VO<sub>2</sub>. (a) Fitted data showing the initial response of the film. Data are plotted as disconnected points, while fits are solid lines. (b) Same as (a), but for the full 3000 ps delay.

TABLE 5.1: Fit parameters for the scans shown in Figures 5.2, 5.4, and 5.5. The two highlighted columns correspond to the plots shown in Figure 5.6.

	NbO <sub>2</sub> (Fig. 5.2)	VO <sub>2</sub> (Fig. 5.2)	NbO <sub>2</sub> (Fig. 5.4)			VO <sub>2</sub> (Fig. 5.5)	
Fluence	2.2 mJ/cm <sup>2</sup>	17.5 mJ/cm <sup>2</sup>	8.8 mJ/cm <sup>2</sup>	35 mJ/cm <sup>2</sup>	140 mJ/cm <sup>2</sup>	422 mJ/cm <sup>2</sup>	422 mJ/cm <sup>2</sup>
$A_0$	-0.22	-0.10	-0.42	-0.76	-3.00	-3.30	-6.30
$t_{off}$ (ps)	2.85	3.00	2.85	2.85	2.85	2.85	3.00
$t_p$ (ps)	0.35	0.55	0.35	0.35	0.35	0.35	0.55
$A_1$	0.0007	0.0004	0.0007	0.0007	0.0007	0.0007	0
$t_1$ (ps)	0.5	0.5	0.5	0.5	0.5	0.5	–
$A_2$	0.000375	0.0004	0.000275	0.000225	0	0	0
$t_2$ (ps)	14	0.7	11	6	–	–	–
$A_3$	0.0001	0.00035	0.000075	0.000012	0.000012	0.000016	0.0015
$t_3$ (ps)	8500	-20,000	8500	8500	-16,000	-20,000	-16,000
RMS	0.000504	0.000692	0.000610	0.001036	0.002508	0.003119	0.022419

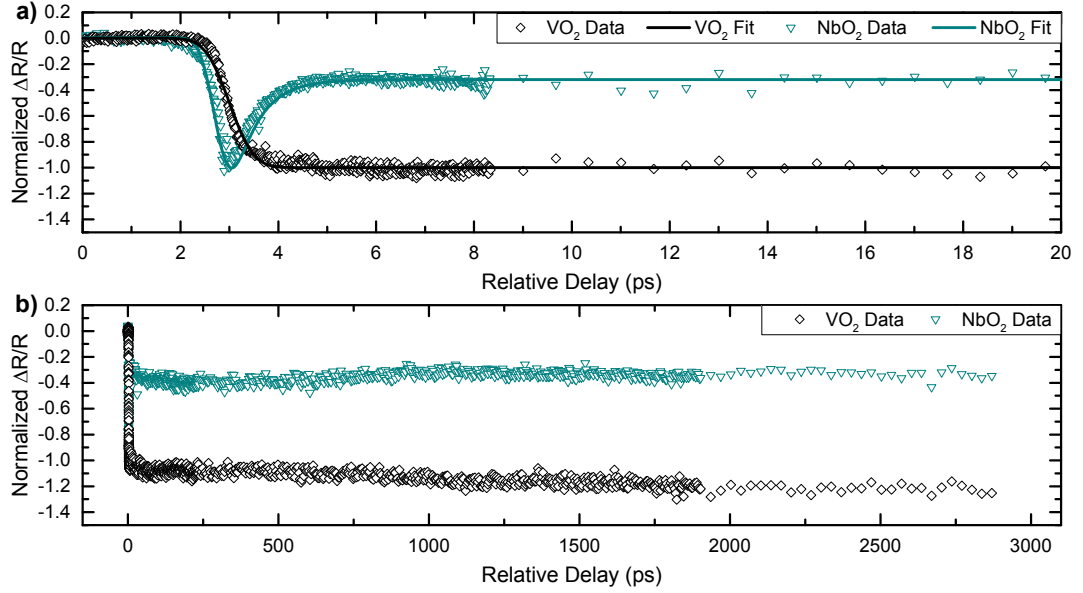


FIG. 5.6: Normalized scans of NbO<sub>2</sub> and VO<sub>2</sub> at 422 mJ/cm<sup>2</sup>, the highest fluence achieved without damaging the samples. (a) Fitted data showing the initial response of the films. Data are plotted as disconnected points, while fits are solid lines. (b) Same as (a), but for the full 3000 ps delay.

## Data Fitting and Analysis

Using an analysis typical of pump-probe studies [33], experimental time-resolved optical reflectivity data were analyzed using a three-time-constant fit given by:

$$\frac{\Delta R}{R} = A_0 * \frac{1}{2} \left( 1 + \text{Erf} \left( \frac{t - t_{off}}{t_p} \right) \right) * \left( A_1 e^{-\left( \frac{t - t_{off}}{t_1} \right)} + A_2 e^{-\left( \frac{t - t_{off}}{t_2} \right)} + A_3 e^{-\left( \frac{t - t_{off}}{t_3} \right)} \right), \quad (5.1)$$

where  $\text{Erf}$  is the standard error function, used here to model the initial fast transient response of the film. The time designated by  $t_{off}$  represents the delay from the start of the scan to the initial transient response, while the time constant  $t_p$  is related to both the laser pulse-width and the rate of the initial fast transient response of the film to the ultrashort laser pulse. While all of the parameters are initially free, both  $t_{off}$  and

$t_p$  are in fact constant for a given sample, as neither the offset nor the pulse-width are fluence-dependent. Therefore any changes in  $t_{off}$  and  $t_p$  are due to the different initial fast transient response of the two materials and, potentially, small changes in the position of the pump and probe beams from sample to sample. The time constants  $t_1$ ,  $t_2$ , and  $t_3$  are related to the scattering and relaxation processes following absorption of the ultrashort laser pulse [142, 143] and are described in more detail below. The constant  $A_0$  sets the overall scaling of the fit to the experimental data and increases with increasing fluence, while  $A_1$ ,  $A_2$ , and  $A_3$  allow for scaling of the effects from the different processes described below.

At 800 nm (1.55 eV), the laser pulse energy is absorbed by the electrons and produces a nonequilibrium between the effective temperature of the electrons and the lattice (phonons) of the material. The time constant  $t_1$  describes scattering processes only within the electronic system (i.e.  $e-e$  scattering) and results in a redistribution of energy within the electron system on a timescale of hundreds of femtoseconds. As is the case for  $t_{off}$  and  $t_p$ , the time constant  $t_1$  and its scaling factor  $A_1$  are constant for a given sample, since the relevant processes do not depend, or are weakly dependent, on the amount of energy deposited by the pump pulse. The exception to this is for the measurements on VO<sub>2</sub> at the highest fluence (Figure 5.5) where the structural IMT completely dominates the response. On a slightly longer timescale, the time constant  $t_2$  describes scattering between the electrons and phonons ( $e-p$  scattering) and the resulting transfer of energy to the lattice. As the fluence increases, both  $t_2$  and the associated scaling factor  $A_2$  decrease. These effects are likely caused by the new phonon spectrum due to the change of the lattice structure as the energy density becomes high enough to begin driving the structural IMT. The third time constant,  $t_3$ , describes slower processes that, at lower fluences, are dominated by the recovery of the excited film, with most of the NbO<sub>2</sub> remaining in the monoclinic structure and the hot carriers relaxing back to the nominal distribution

of the room temperature insulating phase. It is likely that the incomplete recovery of the transient reflectance response at lower fluences is indicative of microscopic regions of the metallic rutile phase of  $\text{NbO}_2$ . The formation and growth of microscopic regions of rutile phase within the insulating matrix has been studied previously in  $\text{VO}_2$  by nearfield [144, 145] and farfield [128] optical measurements, and is expected to also occur in the structural IMT of  $\text{NbO}_2$ . At fluences of  $140 \text{ mJ/cm}^2$  and above,  $A_2$  goes to zero and  $t_3$  becomes negative. While mathematically this would indicate that the  $A_3$  term diverges with increased delay time, physically this indicates the beginning of growth of the metallic rutile phase, i.e. that sufficient energy is transferred to the phonon system to drive the more complete structural transformation associated with the thermally-driven structural IMT. Note that each of the free parameters ( $t_2$ ,  $A_2$ ,  $t_3$ ,  $A_3$ ) was varied programmatically in an iterative process to minimize the RMS of the least square fit as listed in Table 5.1. To test the sensitivity of the fit, the RMS was computed for a  $\pm 10\%$  change from the optimal for each free parameter. The results of this sensitivity study are presented in Table 5.2, and indicate the reliability of the fit.

TABLE 5.2: Results of the sensitivity study on Equation 5.1, showing the percent change in the RMS value of the fit after changing the given parameter by  $\pm 10\%$ .

	$t_1$	$A_2$	$t_2$	$A_3$	$t_3$
+10%	0.51%	4.9%	0.12%	2.4%	0.08%
-10%	1.7%	4.0%	0.04%	5.3%	0.12%

#### 5.1.4 Conclusions

The ultrafast pump-probe studies presented here show for the first time that, as in  $\text{VO}_2$ , the IMT of  $\text{NbO}_2$  can be induced optically. More important is the existence of a

clear electronic response in the NbO<sub>2</sub> film that can be optically detected and that recovers within picoseconds at all fluences, showing a strong similarity to the recently-discovered monoclinic metallic phase in VO<sub>2</sub> [136–139]. NbO<sub>2</sub> films, however, show a significantly faster electronic recovery than VO<sub>2</sub> films, indicating that thin films of NbO<sub>2</sub> may be better suited for all-optical ultrafast switching applications. It is also important to note that the IMT of the NbO<sub>2</sub> films can be optically excited with a lower fluence (2.2 mJ/cm<sup>2</sup>) than VO<sub>2</sub> (17.5 mJ/cm<sup>2</sup>). This lower minimum fluence further indicates that the optical response of NbO<sub>2</sub> can be driven more efficiently in ultrafast switching applications where the higher fluence needed to transition the VO<sub>2</sub> could be damaging to other components. Our results show that the ultrafast electronic response in NbO<sub>2</sub> was evident all the way up to the damage threshold, indicating that this material could provide robust ultrafast switching over a large dynamic range of operation. In addition, the slightly faster initial response of the NbO<sub>2</sub> films could provide an advantage over VO<sub>2</sub> in devices requiring somewhat faster OFF/ON switching times. Of further interest is the combination of NbO<sub>2</sub> and VO<sub>2</sub> thin films in optoelectronic devices - the NbO<sub>2</sub> will switch off in less than 10 ps, while the VO<sub>2</sub> will still be metallic, not switching off for ~20 ps, offering the possibility of combining them in double-function optical switches or memory devices.

## 5.2 Reflection and Transmission of Niobium Dioxide Thin Films During the Insulator-to-Metal Transition

### 5.2.1 Introduction

When  $\text{VO}_2$  becomes metallic, it absorbs more light at 800 nm than in its insulating state [49]; because of the similarities discussed above between  $\text{VO}_2$  and  $\text{NbO}_2$ , we expect a similar change in absorption as the  $\text{NbO}_2$  begins to transition to its metallic state. While equipment limitations precluded simultaneous reflection and transmission studies to directly calculate the absorption of the  $\text{NbO}_2$ , transmission studies by themselves will provide evidence of any increased absorption. We therefore modified the experimental set-up used in the previous work (see Section 3.4.2 for details) to perform the first transmission studies on the IMT in  $\text{NbO}_2$  to further investigate the optically-induced IMT and explore potential advantages for its use in application.

### 5.2.2 Results and Discussion

Consistent with the results discussed in Section 5.1.3, the  $\text{NbO}_2$  film first exhibits an electronic transition at a lower fluence than  $\text{VO}_2$  and displays a larger initial fast transient response. In reflection, as the structural transition was induced in  $\text{VO}_2$ , its response became much larger than that of the  $\text{NbO}_2$ , but in transmission, as shown in Figure 5.7, the  $\text{NbO}_2$  continues to display a larger response than the  $\text{VO}_2$ , even when the  $\text{VO}_2$  is fully-transitioned to the metallic state. It is worth noting here, however, that the absolute percent change in transmission is still larger for  $\text{VO}_2$  than  $\text{NbO}_2$ ; the insulating state of  $\text{VO}_2$  is much more transmissive than that of the  $\text{NbO}_2$ , resulting in a smaller  $\Delta T/T$  signal.

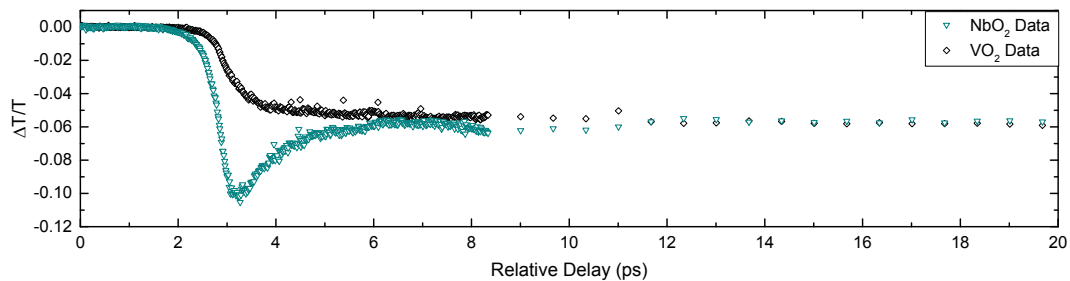


FIG. 5.7: Scans of NbO<sub>2</sub> and VO<sub>2</sub> at the highest fluence achieved without sample damage. At this fluence, the VO<sub>2</sub> is fully-transitioned to the metallic state.

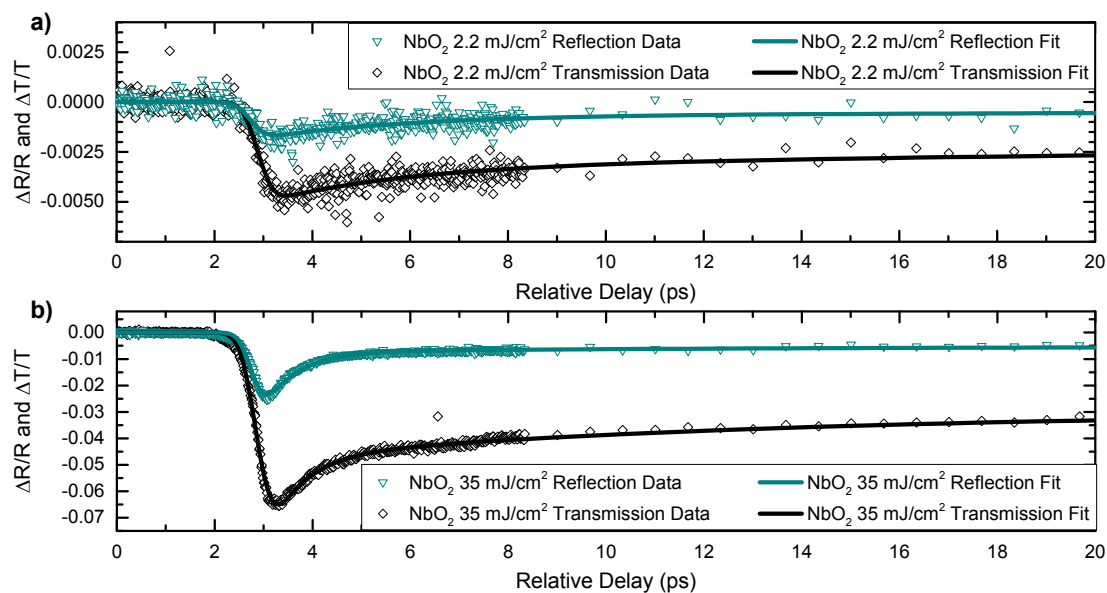


FIG. 5.8: Scans of NbO<sub>2</sub> in reflection (teal) and transmission (black) geometries at two fluences, (a) 2.2 mJ/cm<sup>2</sup> and (b) 35 mJ/cm<sup>2</sup>. Data are plotted as disconnected points, while fits are solid lines. It is clear that there is good agreement between the fit and both reflection and transmission data.

The NbO<sub>2</sub> transmission data were fit using Equation 5.1. As in the previous study on reflection data, all of the parameters are initially free, but  $t_p$  and  $t_{off}$  are the same for a given sample. Additionally, the time constants  $t_1$ ,  $t_2$ , and  $t_3$  are the same in reflection and in transmission for a given fluence, as one would expect for measurements made on the same sample, for all but the very highest fluence. Data and fits in both reflection and transmission from two representative fluences, 2.2 mJ/cm<sup>2</sup> and 35 mJ/cm<sup>2</sup>, are presented in Figure 5.8, showing the very good agreement between the data and the fit.

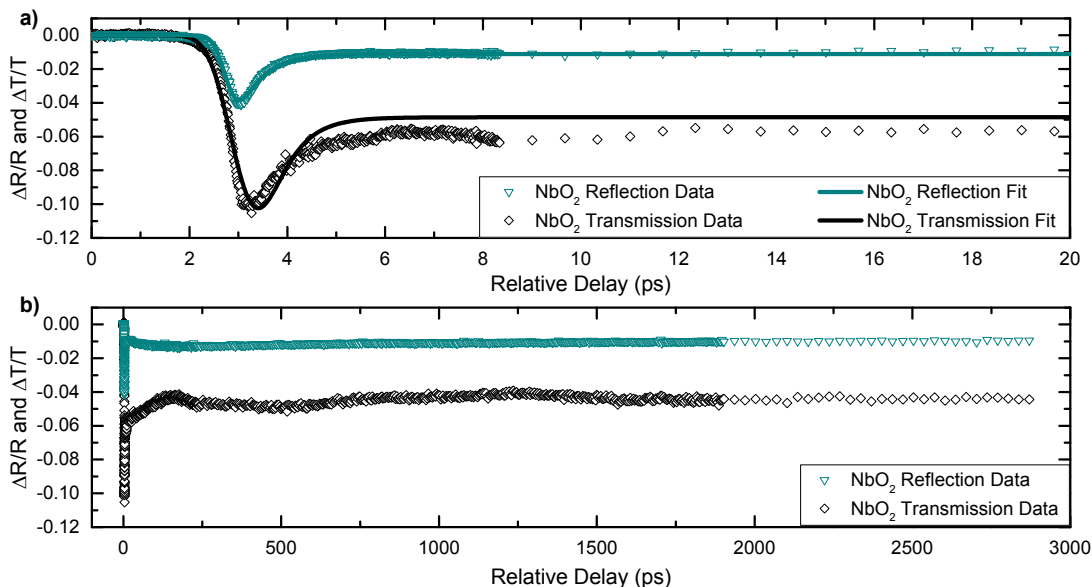


FIG. 5.9: Scans of NbO<sub>2</sub> at the highest fluence at which the transition was observed in both reflection and transmission geometries. (a) Fitted data showing the initial response of the film. Data are plotted as disconnected points, while fits are solid lines. (b) Same as (a), but for the full 3000 ps delay.

As noted above, the time constants for reflection and transmission were not found to be the same for the highest-fluence measurements on the NbO<sub>2</sub>; the data for these measurements are shown in Figure 5.9, with fits using the time constants from the reflection data plotted in Figure 5.9(a). It is clear that such time constants do not match the transmission data: the initial fast transient response fit (time constant  $t_p$ ) does not agree

with the data, and neither do the  $e-e$  and  $e-p$  scattering fits ( $t_1$  and  $t_2$ , respectively). The time scale on which this occurs - no more than a few picoseconds - indicates that there is an additional electronic process or processes taking place in the NbO<sub>2</sub> film that for which the existing model does not account, and the electronic recovery of only 50% in the transmission data (as compared to 70% in reflection) indicates electronic behavior not seen in the structurally-insulating state. The slight oscillation seen in the full-track data shown in Figure 5.9(b) is likely due to variations in the laser over time, as each measurement took approximately 7 hours to complete (see appendix for details).

### 5.2.3 Conclusions

In short, transmission studies on NbO<sub>2</sub> provide further evidence for an electronically-driven light-induced IMT in NbO<sub>2</sub>. Additionally, the fractional change in transmission in NbO<sub>2</sub> is larger at all fluences than that seen in VO<sub>2</sub>, indicating possible advantages for optical limiters and other applications. These results, combined with those from Section 5.1, show that ultrafast studies on NbO<sub>2</sub> thin films may contribute a great deal to the understanding of insulator-to-metal transitions.

## CHAPTER 6

# Conclusion and Outlook

The work presented in this dissertation has focused on developing a better understanding of electron correlations and the results thereof in Nb and Nb-based compound thin films. While the electron correlations themselves in bulk Nb and many of its bulk superconducting compounds are well-understood, there is less understanding of how the constraints inherent in all thin films affect the resulting properties of these materials. Similarly, there is very little work on the electron correlations in NbO<sub>2</sub>, much less the resulting properties.

There is a great deal of interest in enhancing the superconducting properties of thin films for many applications, including SRF cavity coatings. Our studies have shown that both Nb and NbN films exhibit the highest  $H_{C1}$  values when their out-of-plane lattice parameter is as close to bulk as possible; in fact, NbN films thinner than the London penetration depth with a bulk-like lattice parameter exhibit an  $H_{C1}$  greater than that of bulk NbN, in good agreement with existing theory. We have also shown that other superconducting properties such as the superconducting gap  $\Delta(0)$  in Nb and the superconducting surface resistance  $R_{surf}$  of NbN are strongly affected by the grains within a film - small,

disordered grains increase the gap and decrease the surface resistance.

While our work did not show a consistent route to enhanced  $T_C$  in different types superconducting thin films, there is recent work that has demonstrated the possibility of increasing  $T_C$  above bulk values in many superconductors by using stacked structures of superconducting-insulating layers, similar to those used in the SIS model discussed in Chapters 1 and 4, to modify the net dielectric constant of the structure [146, 147]. It is thus potentially possible to almost completely control the electronic and therefore superconducting properties in future thin films by careful control of their microstructure.

The ultrafast pump-probe studies discussed in Chapter 5 were the first of their kind on NbO<sub>2</sub> and showed that the insulator-to-metal transition can be optically induced in that material. Of even greater scientific import, these studies show that NbO<sub>2</sub> displays a fast ( $\sim 2$  ps) strong electronic recovery at all fluences, as compared to VO<sub>2</sub>, in which this electronic behavior is almost completely dominated by the effects of the structural transition. Such separation of the electronic and structural transition allows for independent investigation into the two components of the transition.

There are countless opportunities for further measurements on the light-induced IMT in NbO<sub>2</sub>: measurements at wavelengths other than the 800 nm used here and simultaneous reflection and transmission studies are among the most straightforward, and could provide an experimental understanding of the electronic properties of the high-temperature metallic state, which have not yet been studied. Ultrafast structural studies, similar to those already performed on VO<sub>2</sub> [33], would yield information about the dynamics of the light-induced transition in NbO<sub>2</sub>, and repeating any of the aforementioned measurements on NbO<sub>2</sub> films of different thicknesses or grown on different substrates would show the effects of film microstructure on the transition. Data from such studies would ultimately allow for a greater theoretical understanding of the mechanism behind the IMT, and could potentially help resolve the decades-long debate over the nature of such transitions.

# APPENDIX

## Pump-Probe Measurement Details

This appendix lists the settings and parameters used in the pump-probe measurements discussed in Chapter 5. Each measurement was divided into four sections of varying resolution; as the relative delay between pump and probe beams increased, the step size and averaging time per step was decreased to keep the total measurement time somewhat reasonable; even so, each measurement ran for approximately 7 hours. The sections of the scans are defined by the position on the delay stage, given in mm, where the start of the scan ( $t = 0$  ps) is 585.25 mm and the end of the scan is 0 mm. The time constant for the lock-in amplifier was 300 ms, although the sensitivity of the lock-in varied with fluence.

TABLE .1: Scan parameters for all pump-probe measurements discussed in Chapter 5.

Section Number	Section Start Position (mm)	Section End Position (mm)	Step Size $\mu\text{m}$	Averaging Time (s)
1	585.25	584	2	10
2	584	550	100	10
3	550	300	2000	12
4	300	0	5000	15

## BIBLIOGRAPHY

- [1] Encyclopædia Britannica, *Niobium processing* (2009), URL <https://www.britannica.com/technology/niobium-processing>.
- [2] T. Luhman and D. Dew-Hughes, *Metallurgy of Superconducting Materials: Treatise on Materials Science and Technology*, v. 14 (Elsevier Science, 2013), ISBN 9781483218236, URL <https://books.google.com/books?id=jkUvBQAAQBAJ>.
- [3] A.-M. Valente-Feliciano, *Beyond Niobium*, SRF2013 Conference Tutorial (2013), URL <https://indico.in2p3.fr/event/9782/session/2/contribution/12/material/slides/0.pdf>.
- [4] J. K. Hulm, C. K. Jones, R. A. Hein, and J. W. Gibson, *J. Low Temp. Phys.* **7**, 291 (1972), ISSN 1573-7357, <http://dx.doi.org/10.1007/BF00660068>.
- [5] M. R. Beebe, A. M. Valente-Feliciano, D. B. Beringer, J. A. Creeden, S. E. Madaras, Z. Li, K. Yang, L. Phillips, C. E. Reece, and R. A. Lukaszew, *IEEE Trans. Appl. Supercond.* **27**, 1 (2017), ISSN 1051-8223, <http://ieeexplore.ieee.org/document/7755793/>.
- [6] S. Posen and M. Liepe, *Proc. PAC2013*, Pasadena, CA USA pp. 754–758 (2013), URL <http://accelconf.web.cern.ch/accelconf/pac2013/papers/wezba1.pdf>.
- [7] D. Larbalestier, G. Fisk, B. Montgomery, and D. Hawksworth, *Phys. Today* **39**, 24 (1986), <http://physicstoday.scitation.org/doi/10.1063/1.881053>.

- [8] A.-M. Valente-Feliciano, *SRF Materials Other Than Bulk Niobium*, US-PAS2015 Course (2015), URL <http://uspas.fnal.gov/materials/15Rutgers/AMVF{ }NewMaterials.pdf>.
- [9] A. B. Posadas, A. OHara, S. Rangan, R. A. Bartynski, and A. A. Demkov, *Appl. Phys. Lett.* **104**, 092901 (2014), <http://aip.scitation.org/doi/10.1063/1.4867085>.
- [10] A. M. Okaz and P. H. Keesom, *Phys. Rev. B* **12**, 4917 (1975), <http://link.aps.org/doi/10.1103/PhysRevB.12.4917>.
- [11] M. R. Beebe, J. M. Klopff, Y. Wang, S. Kittiwatanakul, J. Lu, S. A. Wolf, and R. A. Lukaszew, *Opt. Mater. Express* **7**, 213 (2017), <https://doi.org/10.1364/OME.7.000213>.
- [12] X. Q. Jia, L. Kang, X. Y. Liu, Z. H. Wang, B. B. Jin, S. B. Mi, J. Chen, W. W. Xu, and P. H. Wu, *IEEE Trans. Appl. Supercond.* **23**, 2300704 (2013), ISSN 1051-8223, <https://doi.org/10.1109/TASC.2012.2235508>.
- [13] A. Casaburi, N. Zen, K. Suzuki, M. Ejrnaes, S. Pagano, R. Cristiano, and M. Ohkubo, *Appl. Phys. Lett.* **94**, 212502 (2009), <http://dx.doi.org/10.1063/1.3142419>.
- [14] D. Proch, *Reports on Progress in Physics* **61**, 431 (1998), <https://doi.org/10.1088/0034-4885/61/5/001>.
- [15] M. R. Beebe, D. B. Beringer, M. C. Burton, K. Yang, and R. A. Lukaszew, *J. Vac. Sci. Technol., A* **34**, 021510 (2016), <http://avs.scitation.org/doi/10.1116/1.4940132>.

- [16] H. Padamsee, J. Knobloch, and T. Hays, *RF Superconductivity for Accelerators* (Wiley, 2008), ISBN 9783527408429, URL <https://books.google.com/books?id=001AAQAAIAAJ>.
- [17] N. Valles, R. Eichhorn, F. Furuta, M. Gi, D. Gonnella, V. Ho, G. Hoffstaetter, M. Liepe, T. O'Connell, S. Posen, et al., Proc. SRF2013, Paris, France pp. 300–304 (2013), URL <http://accelconf.web.cern.ch/AccelConf/SRF2013/papers/mop071.pdf>.
- [18] M. C. Burton, M. R. Beebe, K. Yang, R. A. Lukaszew, A.-M. Valente-Feliciano, and C. Reece, *J. Vac. Sci. Technol., A* **34**, 021518 (2016), <http://dx.doi.org/10.1116/1.4941735>.
- [19] S. Calatroni, *J. Physica C* **441**, 95 (2006), <http://www.sciencedirect.com/science/article/pii/S0921453406001596>.
- [20] A. Gurevich, *Appl. Phys. Lett.* **88**, 012511 (2006), <http://dx.doi.org/10.1063/1.2162264>.
- [21] D. B. Beringer, C. Clavero, T. Tan, X. X. Xi, W. M. Roach, and R. A. Lukaszew, *IEEE Trans. Appl. Supercond.* **23**, 7500604 (2013), <https://doi.org/10.1109/TASC.2012.2234192>.
- [22] W. M. Roach, D. B. Beringer, Z. Li, C. Clavero, and R. A. Lukaszew, *IEEE Trans. Appl. Supercond.* **23**, 8600203 (2013), <https://doi.org/10.1109/TASC.2012.2234956>.
- [23] J. H. de Boer and E. J. W. Verwey, *Proc. Phys. Soc.* **49**, 59 (1937), <https://doi.org/10.1088/0959-5309/49/4S/307>.

- [24] R. Peierls, in *Proc. Phys. Soc. London* (1937), vol. 49, p. 72, <https://doi.org/10.1088/0959-5309/49/4S/308>.
- [25] F. J. Morin, *Phys. Rev. Lett.* **3**, 34 (1959), <http://link.aps.org/doi/10.1103/PhysRevLett.3.34>.
- [26] W. Roach and I. Balberg, *Solid State Commun.* **9**, 551 (1971), ISSN 0038-1098, URL <http://www.sciencedirect.com/science/article/pii/003810987190144X>.
- [27] A. O'Hara and A. A. Demkov, *Phys. Rev. B* **91**, 094305 (2015), URL <http://link.aps.org/doi/10.1103/PhysRevB.91.094305>.
- [28] C. G. Granqvist, *Sol. Energy Mater. Sol. Cells* **91**, 1529 (2007), ISSN 0927-0248, <http://www.sciencedirect.com/science/article/pii/S092702480700205X>.
- [29] S. Lysenko, A. Rúa, V. Vikhnin, F. Fernández, and H. Liu, *Phys. Rev. B* **76**, 035104 (2007), <http://link.aps.org/doi/10.1103/PhysRevB.76.035104>.
- [30] E. Strelcov, Y. Lilach, and A. Kolmakov, *Nano Letters* **9**, 2322 (2009), PMID: 19507888, <http://dx.doi.org/10.1021/nl900676n>.
- [31] V. Eyert, *Europhys. Lett.* **58**, 851 (2002), <http://stacks.iop.org/0295-5075/58/i=6/a=851>.
- [32] M. Imada, A. Fujimori, and Y. Tokura, *Rev. Mod. Phys.* **70**, 1039 (1998), <http://link.aps.org/doi/10.1103/RevModPhys.70.1039>.
- [33] A. Cavalleri, C. Tóth, C. W. Siders, J. A. Squier, F. Ráksi, P. Forget, and J. C. Kieffer, *Phys. Rev. Lett.* **87**, 237401 (2001), <http://link.aps.org/doi/10.1103/PhysRevLett.87.237401>.

- [34] A. Cavalleri, T. Dekorsy, H. H. W. Chong, J. C. Kieffer, and R. W. Schoenlein, *Phys. Rev. B* **70**, 161102 (2004), <http://link.aps.org/doi/10.1103/PhysRevB.70.161102>.
- [35] M. Hada, K. Okimura, and J. Matsuo, *Appl. Phys. Lett.* **99**, 051903 (2011), <http://dx.doi.org/10.1063/1.3621900>.
- [36] G. Seo, B.-J. Kim, Y. W. Lee, and H.-T. Kim, *Appl. Phys. Lett.* **100**, 011908 (2012), <http://dx.doi.org/10.1063/1.3672812>.
- [37] X.-Y. Peng, B. Wang, J. Teng, J. B. K. Kana, and X. Zhang, *J. Appl. Phys.* **114**, 163103 (2013), <http://dx.doi.org/10.1063/1.4827193>.
- [38] X. Xue, M. Jiang, G. Li, X. Lin, G. Ma, and P. Jin, *J. Appl. Phys.* **114**, 193506 (2013), <http://dx.doi.org/10.1063/1.4832776>.
- [39] B. T. O'Callahan, A. C. Jones, J. Hyung Park, D. H. Cobden, J. M. Atkin, and M. B. Raschke, *Nat. Commun.* **6**, 6849 (2015), <http://dx.doi.org/10.1038/ncomms7849>.
- [40] M. F. Becker, A. B. Buckman, R. M. Walser, T. Lpine, P. Georges, and A. Brun, *Appl. Phys. Lett.* **65**, 1507 (1994), <http://dx.doi.org/10.1063/1.112974>.
- [41] R. M. Wentzcovitch, W. W. Schulz, and P. B. Allen, *Phys. Rev. Lett.* **72**, 3389 (1994), <http://link.aps.org/doi/10.1103/PhysRevLett.72.3389>.
- [42] A. O'Hara, T. N. Nunley, A. B. Posadas, S. Zollner, and A. A. Demkov, *J. Appl. Phys.* **116**, 213705 (2014), <http://aip.scitation.org/doi/pdf/10.1063/1.4903067>.
- [43] G. C. Vezzoli, *J. Appl. Phys.* **50**, 6390 (1979), <http://aip.scitation.org/doi/10.1063/1.325730>.

- [44] G. C. Vezzoli, J. Appl. Phys. **51**, 2693 (1980), <http://aip.scitation.org/doi/10.1063/1.327929>.
- [45] S. K. Nandi, X. Liu, D. K. Venkatachalam, and R. G. Elliman, J. Phys. D: Appl. Phys. **48**, 195105 (2015), <http://stacks.iop.org/0022-3727/48/i=19/a=195105>.
- [46] T. Joshi, T. R. Senty, P. Borisov, A. D. Bristow, and D. Lederman, J. Phys. D: Appl. Phys. **48**, 335308 (2015), <http://stacks.iop.org/0022-3727/48/i=33/a=335308>.
- [47] D. B. Beringer, PhD in Physics, The College of William & Mary, Williamsburg, Virginia, USA (2017), ProQuest Number: 10238928.
- [48] W. M. Roach, PhD in Applied Science, The College of William & Mary, Williamsburg, Virginia, USA (2014), ProQuest Number: 3580414.
- [49] E. L. Radue, PhD in Physics, The College of William & Mary, Williamsburg, Virginia, USA (2016), ProQuest Number: 10168226.
- [50] J. J. Thomson, The London, Edinburgh, and Dublin Philosophical Magazine and Journal of Science **44**, 293 (1897), <http://dx.doi.org/10.1080/14786449708621070>.
- [51] N. Ashcroft and N. Mermin, *Solid State Physics*, HRW International Editions (Holt, Rinehart and Winston, 1976), ISBN 9780030839931, URL <https://books.google.com/books?id=oXIfAQAAAJ>.
- [52] P. Drude, Ann. Phys. (Berlin) **306**, 566 (1900), ISSN 1521-3889, <http://dx.doi.org/10.1002/andp.19003060312>.
- [53] P. Drude, Ann. Phys. (Berlin) **308**, 369 (1900), ISSN 1521-3889, <http://dx.doi.org/10.1002/andp.19003081102>.

- [54] W. H. Bragg and W. L. Bragg, *Phil. Trans. R. Soc. A* **88**, 428 (1913), ISSN 0950-1207, <http://rspa.royalsocietypublishing.org/content/88/605/428.full.pdf>.
- [55] W. Pauli, *Zeitschrift für Physik* **31**, 765 (1925), ISSN 0044-3328, <http://dx.doi.org/10.1007/BF02980631>.
- [56] A. Sommerfeld, *Zeitschrift für Physik* **47**, 1 (1928), ISSN 0044-3328, <http://dx.doi.org/10.1007/BF01391052>.
- [57] F. Bloch, *Zeitschrift für Physik* **52**, 555 (1929), ISSN 0044-3328, <http://dx.doi.org/10.1007/BF01339455>.
- [58] A. H. Wilson, *Phil. Trans. R. Soc. A* **133**, 458 (1931), ISSN 0950-1207, <http://rspa.royalsocietypublishing.org/content/133/822/458.full.pdf>.
- [59] N. Mott, *Metal-Insulator Transitions* (Taylor & Francis, 1990), ISBN 9780850667837, URL <https://books.google.com/books?id=Q0mJQgAACAAJ>.
- [60] H. K. Onnes, *Commun. Phys. Lab. Univ. Leiden* (1911).
- [61] W. Meissner and R. Ochsenfeld, *Naturwissenschaften* **21**, 787 (1933), ISSN 1432-1904, <http://dx.doi.org/10.1007/BF01504252>.
- [62] C. Kittel, *Introduction to Solid State Physics* (Wiley, 1996), ISBN 9780471111818, URL <https://books.google.com/books?id=1X8pAQAAMAAJ>.
- [63] J. Bardeen, L. N. Cooper, and J. R. Schrieffer, *Phys. Rev.* **106**, 162 (1957), <http://link.aps.org/doi/10.1103/PhysRev.106.162>.
- [64] J. Bardeen, L. N. Cooper, and J. R. Schrieffer, *Phys. Rev.* **108**, 1175 (1957), <http://link.aps.org/doi/10.1103/PhysRev.108.1175>.

- [65] R. Peierls, *Quantum Theory of Solids*, International Series of Monographs on Physics (Clarendon Press, 1996), ISBN 9780192670175, URL <https://books.google.com/books?id=GIrsImJvMgMC>.
- [66] N. F. Mott, Proc. Phys. Soc. A **62**, 416 (1949), <http://stacks.iop.org/0370-1298/62/i=7/a=303>.
- [67] M. Ohring, *The Materials Science of Thin Films*, Referex Engineering (Academic Press, 1992), ISBN 9780125249904, URL [https://books.google.com/books?id=\\_oC1zwLnoRwC](https://books.google.com/books?id=_oC1zwLnoRwC).
- [68] C. Clavero, D. B. Beringer, W. M. Roach, J. R. Skuza, K. C. Wong, A. D. Batchelor, C. E. Reece, and R. A. Lukaszew, Cryst. Growth Des. **12**, 2588 (2012), <http://pubs.acs.org/doi/abs/10.1021/cg3001834>.
- [69] E. Radue, E. Crisman, L. Wang, S. Kittiwatanakul, J. Lu, S. A. Wolf, R. Wincheski, R. A. Lukaszew, and I. Novikova, J. Appl. Phys. **113**, 233104 (2013), <http://dx.doi.org/10.1063/1.4811689>.
- [70] E. Radue, L. Wang, S. Kittiwatanakul, J. Lu, S. A. Wolf, E. Rossi, R. A. Lukaszew, and I. Novikova, J. Opt. **17**, 025503 (2015), <http://stacks.iop.org/2040-8986/17/i=2/a=025503>.
- [71] A. Anders, Thin Solid Films **518**, 4087 (2010), <http://dx.doi.org/10.1016/j.tsf.2009.10.145>.
- [72] W. M. Roach, J. R. Skuza, D. B. Beringer, Z. Li, C. Clavero, and R. A. Lukaszew, Supercond. Sci. and Technol. **25**, 125016 (2012), URL <http://stacks.iop.org/0953-2048/25/i=12/a=125016>.

- [73] A.-M. Valente-Feliciano, S. Aull, G. Ereemeev, T. Proslie, C. Reece, and J. Spradlin, in *Proc. SRF2015, Whistler, Canada* (2015), p. TUPB029, URL <http://inspirehep.net/record/1482076/files/tupb029.pdf>.
- [74] A.-M. Valente-Feliciano, Theses, Université Paris Sud - Paris XI (2014), URL <https://tel.archives-ouvertes.fr/tel-01126883>.
- [75] A. C. L. Fontaine and P. Louvet, *Plasma Sources Sci. Technol.* **8**, 125 (1999), <http://stacks.iop.org/0963-0252/8/i=1/a=015>.
- [76] U. Helmersson, M. Lattemann, J. Bohlmark, A. P. Ehiasarian, and J. T. Gudmundsson, *Thin Solid Films* **513**, 1 (2006), ISSN 0040-6090, <http://www.sciencedirect.com/science/article/pii/S0040609006004317>.
- [77] K. G. West, J. Lu, J. Yu, D. Kirkwood, W. Chen, Y. Pei, J. Claassen, and S. A. Wolf, *J. Vac. Sci. Technol., A* **26**, 133 (2008), <http://dx.doi.org/10.1116/1.2819268>.
- [78] B. Warren, *X-Ray Diffraction*, Dover Books on Physics (Dover Publications, 2012), ISBN 9780486141619, URL [https://books.google.com/books?id=cA\\_EAgAAQBAJ](https://books.google.com/books?id=cA_EAgAAQBAJ).
- [79] V. Holý, J. Kuběna, I. Ohlídal, K. Lischka, and W. Plotz, *Phys. Rev. B* **47**, 15896 (1993), <http://link.aps.org/doi/10.1103/PhysRevB.47.15896>.
- [80] U. Pietsch, V. Holy, and T. Baumbach, *High-Resolution X-Ray Scattering: From Thin Films to Lateral Nanostructures*, Advanced Texts in Physics (Springer New York, 2004), ISBN 9780387400921, URL <https://books.google.com/books?id=p8r9PpdpYrAC>.
- [81] H. Weinstock, *SQUID Sensors: Fundamentals, Fabrication, and Applications*, NATO ASI Series (Kluwer Academic Publishers, 1996), ISBN 9780792343509, URL [https://books.google.com/books?id=cFJ7eQGS\\_FEC](https://books.google.com/books?id=cFJ7eQGS_FEC).

- [82] B. Josephson, Phys. Lett. **1**, 251 (1962), ISSN 0031-9163, <http://www.sciencedirect.com/science/article/pii/0031916362913690>.
- [83] F. London, *Superfluids*, no. V. 1 in Structure of Matter Series (Wiley, 1950), URL <https://books.google.com/books?id=DtvvAAAAAAAJ>.
- [84] B. S. Deaver and W. M. Fairbank, Phys. Rev. Lett. **7**, 43 (1961), <http://link.aps.org/doi/10.1103/PhysRevLett.7.43>.
- [85] R. Doll and M. Näbauer, Phys. Rev. Lett. **7**, 51 (1961), <http://link.aps.org/doi/10.1103/PhysRevLett.7.51>.
- [86] Quantum Design, Inc., *Magnetic Property Measurement System MPMS XL Hardware Reference Manual* (2005), URL <https://www.qdusa.com>.
- [87] M. Putti, C. Ferdeghini, M. Monni, I. Pallecchi, C. Tarantini, P. Manfrinetti, A. Palenzona, D. Daghero, R. S. Gonnelli, and V. A. Stepanov, Phys. Rev. B **71**, 144505 (2005), <http://link.aps.org/doi/10.1103/PhysRevB.71.144505>.
- [88] C. Bohmer, G. Brandstatter, and H. W. Weber, Supercond. Sci. Technol. **10**, A1 (1997), <http://iopscience.iop.org/0953-2048/10/7A/002>.
- [89] Y.-P. Zhao, R. M. Gamache, G.-C. Wang, T.-M. Lu, G. Palasantzas, and J. T. M. D. Hosson, J. Appl. Phys. **89**, 1325 (2001), <http://dx.doi.org/10.1063/1.1331065>.
- [90] J. Shah, *Ultrafast Spectroscopy of Semiconductors and Semiconductor Nanostructures*, Springer Series in Solid-State Sciences (Springer Berlin Heidelberg, 2013), ISBN 9783662037706, URL <https://books.google.com/books?id=p-7tCAAQBAJ>.
- [91] *Operator's Manual Coherent Legend Elite Ultrafast Amplifier Laser Systems*, Coherent, Inc., 5100 Patrick Henry Drive, Santa Clara, CA USA 95054 (2010).

- [92] *Operator's Manual Mantis Modelocked Titanium:Sapphire Laser System*, Coherent, Inc., 5100 Patrick Henry Drive, Santa Clara, CA USA 95054 (2008).
- [93] J. C. Villegir, N. Hadacek, S. Monso, B. Delnet, A. Roussy, P. Febvre, G. Lamura, and J. Y. Laval, *IEEE Trans. on Appl. Supercond.* **11**, 68 (2001), ISSN 1051-8223, <https://doi.org/10.1109/77.919286>.
- [94] A.-M. Valente-Feliciano, in *Proc. SRF2011, Chicago, Illinois* (2011), p. TUIOB06, URL <https://accelconf.web.cern.ch/AccelConf/SRF2011/papers/tuiob06.pdf>.
- [95] Crystallography Open Database, *Niobium Crystal Structure*, URL <http://www.crystallography.net/cod/9008546.html>.
- [96] H. Weber, E. Seidl, M. Botlo, C. Laa, H. Wiesinger, and J. Rammer, *Physica C: Superconductivity* **161**, 287 (1989), ISSN 0921-4534, <http://www.sciencedirect.com/science/article/pii/0921453489903389>.
- [97] D. K. Finnemore, T. F. Stromberg, and C. A. Swenson, *Phys. Rev.* **149**, 231 (1966), <http://link.aps.org/doi/10.1103/PhysRev.149.231>.
- [98] S. Casalbuoni, E. Knabbe, J. Ktzler, L. Lilje, L. von Sawilski, P. Schmser, and B. Steffen, *Nucl. Instrum. Methods Phys. Res., Sect. A* **538**, 45 (2005), ISSN 0168-9002, <http://www.sciencedirect.com/science/article/pii/S0168900204020315>.
- [99] L. Ozyuzer, J. Zasadzinski, and K. Gray, *Cryogenics* **38**, 911 (1998), ISSN 0011-2275, <http://www.sciencedirect.com/science/article/pii/S0011227598000605>.
- [100] T. Proslie, J. Zasadzinski, J. Moore, M. Pellin, J. Elam, L. Cooley, C. Antoine,

- J. Norem, and K. E. Gray, *Appl. Phys. Lett.* **93**, 192504 (2008), <http://dx.doi.org/10.1063/1.2995996>.
- [101] A.-M. Valente-Feliciano, Private communication.
- [102] D. E. Morris and M. Tinkham, *Phys. Rev.* **134**, A1154 (1964), <http://link.aps.org/doi/10.1103/PhysRev.134.A1154>.
- [103] A. V. Pronin, M. Dressel, A. Pimenov, A. Loidl, I. V. Roshchin, and L. H. Greene, *Phys. Rev. B* **57**, 14416 (1998), <http://link.aps.org/doi/10.1103/PhysRevB.57.14416>.
- [104] J. J. Hauser and H. C. Theuerer, *Phys. Rev.* **134**, A198 (1964), <http://link.aps.org/doi/10.1103/PhysRev.134.A198>.
- [105] J. J. Hauser and H. C. Theuerer, *Rev. Mod. Phys.* **36**, 80 (1964), <http://link.aps.org/doi/10.1103/RevModPhys.36.80>.
- [106] X. Zhang, A. Engel, Q. Wang, A. Schilling, A. Semenov, M. Sidorova, H.-W. Hübers, I. Charaev, K. Ilin, and M. Siegel, *Phys. Rev. B* **94**, 174509 (2016), <http://link.aps.org/doi/10.1103/PhysRevB.94.174509>.
- [107] V. B. Verma, A. E. Lita, M. R. Vissers, F. Marsili, D. P. Pappas, R. P. Mirin, and S. W. Nam, *Appl. Phys. Lett.* **105**, 022602 (2014), <http://dx.doi.org/10.1063/1.4890277>.
- [108] M. Abdel-Hafez, J. Ge, A. N. Vasiliev, D. A. Chareev, J. Van de Vondel, V. V. Moshchalkov, and A. V. Silhanek, *Phys. Rev. B* **88**, 174512 (2013), <http://link.aps.org/doi/10.1103/PhysRevB.88.174512>.
- [109] U. Rauchschwalbe, F. Steglich, G. R. Stewart, A. L. Giorgi, P. Fulde, and K. Maki, *Europhys. Lett.* **3**, 751 (1987), <http://stacks.iop.org/0295-5075/3/i=6/a=016>.

- [110] T. Tajima, *DC and RF Measurements of Thin Film MgB<sub>2</sub>*, The 4th International Workshop on Thin Films and New Ideas for Pushing the Limits of RF Superconductivity, Padua, Italy (2010), URL <https://indico.in2p3.fr/event/9782/session/2/contribution/12/material/slides/0.pdf>.
- [111] S. Aull, T. Junginger, J. Knobloch, A. Sublet, A-M. Valente-Feliciano, W. Venturini Delsolaro, and P. Zhang, in *Proc. SRF2015, Whistler, Canada* (2015), p. TUBA03, URL <http://srf2015.vrws.de/papers/tuba03.pdf>.
- [112] A. Zieba and S. Foner, *Rev. Sci. Instrum.* **53**, 1344 (1982), <http://dx.doi.org/10.1063/1.1137182>.
- [113] V. Kozhevnikov and C. V. Haesendonck, Private communication.
- [114] Z. Wang, A. Kawakami, Y. Uzawa, and B. Komiyama, *J. Appl. Phys.* **79**, 7837 (1996), <http://aip.scitation.org/doi/pdf/10.1063/1.362392>.
- [115] S. A. Wolf, I. L. Singer, E. J. Cukauskas, T. L. Francavilla, and E. F. Skelton, *J. Vac. Sci. Technol.* **17**, 411 (1980), <http://avs.scitation.org/doi/10.1116/1.570469>.
- [116] Y. M. Shy, L. E. Toth, and R. Somasundaram, *J. Appl. Phys.* **44**, 5539 (1973), <http://aip.scitation.org/doi/10.1063/1.1662193>.
- [117] J. R. Gavaler, J. K. Hulm, M. A. Janocko, and C. K. Jones, *J. Vac. Sci. Technol.* **6**, 177 (1969), <http://avs.scitation.org/doi/10.1116/1.1492653>.
- [118] D. D. Bacon, A. T. English, S. Nakahara, F. G. Peters, H. Schreiber, W. R. Sinclair, and R. B. van Dover, *J. Appl. Phys.* **54**, 6509 (1983), <http://aip.scitation.org/doi/10.1063/1.331881>.
- [119] F. M. Smits, *Bell System Technical Journal* **37**, 711 (1958), ISSN 1538-7305, <http://dx.doi.org/10.1002/j.1538-7305.1958.tb03883.x>.

- [120] H.-D. Liu, Y.-P. Zhao, G. Ramanath, S. Murarka, and G.-C. Wang, *Thin Solid Films* **384**, 151 (2001), ISSN 0040-6090, <http://www.sciencedirect.com/science/article/pii/S0040609000018186>.
- [121] E. J. Cukauskas, W. L. Carter, and S. B. Qadri, *J. Appl. Phys.* **57**, 2538 (1985), <http://dx.doi.org/10.1063/1.335442>.
- [122] W. Yoshiki and T. Tanabe, *Opt. Express* **22**, 24332 (2014), <http://www.opticsexpress.org/abstract.cfm?URI=oe-22-20-24332>.
- [123] R. C. Hollins, *Curr. Opin. Solid State Mater. Sci.* **4**, 189 (1999), ISSN 1359-0286, <http://www.sciencedirect.com/science/article/pii/S1359028699000091>.
- [124] S. Perumbilavil, P. Sankar, T. P. Rose, and R. Philip, *Appl. Phys. Lett.* **107**, 051104 (2015), <http://aip.scitation.org/doi/10.1063/1.4928124>.
- [125] G. Steinmeyer, *J. Opt. A* **5**, R1 (2003), <http://stacks.iop.org/1464-4258/5/i=1/a=201>.
- [126] H. W. Verleur, A. S. Barker, and C. N. Berglund, *Phys. Rev.* **172**, 788 (1968), <http://link.aps.org/doi/10.1103/PhysRev.172.788>.
- [127] D. I. Khomskii, *Transition Metal Compounds* (Cambridge University Press, 2014), ISBN 9781139096782, URL <https://www.cambridge.org/core/books/transition-metal-compounds/037907D3274F602D84CFECA02A493395>.
- [128] L. Wang, I. Novikova, J. M. Klopff, S. Madaras, G. P. Williams, E. Madaras, J. Lu, S. A. Wolf, and R. A. Lukaszew, *Adv. Opt. Mater.* **2**, 29 (2014), ISSN 2195-1071, <http://dx.doi.org/10.1002/adom.201470004>.
- [129] A. Zylbersztein and N. F. Mott, *Phys. Rev. B* **11**, 4383 (1975), <http://link.aps.org/doi/10.1103/PhysRevB.11.4383>.

- [130] M. Rini, Z. Hao, R. W. Schoenlein, C. Giannetti, F. Parmigiani, S. Fourmaux, J. C. Kieffer, A. Fujimori, M. Onoda, S. Wall, et al., *Appl. Phys. Lett.* **92**, 181904 (2008), <http://aip.scitation.org/doi/10.1063/1.2921784>.
- [131] M. Rodriguez-Vega, M. T. Simons, E. Radue, S. Kittiwatanakul, J. Lu, S. A. Wolf, R. A. Lukaszew, I. Novikova, and E. Rossi, *Phys. Rev. B* **92**, 115420 (2015), <http://link.aps.org/doi/10.1103/PhysRevB.92.115420>.
- [132] A. A. Bolzan, C. Fong, B. J. Kennedy, and C. J. Howard, *J. Solid State Chem.* **113**, 9 (1994), ISSN 0022-4596, <http://www.sciencedirect.com/science/article/pii/S002245968471334X>.
- [133] N. B. Aetukuri, A. X. Gray, M. Drouard, M. Cossale, L. Gao, A. H. Reid, R. Kukreja, H. Ohldag, C. A. Jenkins, E. Arenholz, et al., *Nat. Phys.* **9**, 661 (2013), <http://dx.doi.org/10.1038/nphys2733>.
- [134] Y. Wang, R. B. Comes, S. Kittiwatanakul, S. A. Wolf, and J. Lu, *J. Vac. Sci. Technol., A* **33**, 021516 (2015), <http://avs.scitation.org/doi/10.1116/1.4906143>.
- [135] L. Wang, E. Radue, S. Kittiwatanakul, C. Clavero, J. Lu, S. A. Wolf, I. Novikova, and R. A. Lukaszew, *Opt. Lett.* **37**, 4335 (2012), <https://doi.org/10.1364/OL.37.004335>.
- [136] T. L. Cocker, L. V. Titova, S. Fourmaux, G. Holloway, H.-C. Bandulet, D. Brassard, J.-C. Kieffer, M. A. El Khakani, and F. A. Hegmann, *Phys. Rev. B* **85**, 155120 (2012), <http://link.aps.org/doi/10.1103/PhysRevB.85.155120>.
- [137] V. R. Morrison, R. P. Chatelain, K. L. Tiwari, A. Hendaoui, A. Bruhács, M. Chaker, and B. J. Siwick, *Science* **346**, 445 (2014), ISSN 0036-8075, <http://science.sciencemag.org/content/346/6208/445.full.pdf>.

- [138] D. Wegkamp, M. Herzog, L. Xian, M. Gatti, P. Cudazzo, C. L. McGahan, R. E. Marvel, R. F. Haglund, A. Rubio, M. Wolf, et al., Phys. Rev. Lett. **113**, 216401 (2014), <http://link.aps.org/doi/10.1103/PhysRevLett.113.216401>.
- [139] J. Laverock, S. Kittiwatanakul, A. A. Zakharov, Y. R. Niu, B. Chen, S. A. Wolf, J. W. Lu, and K. E. Smith, Phys. Rev. Lett. **113**, 216402 (2014), <http://link.aps.org/doi/10.1103/PhysRevLett.113.216402>.
- [140] D. J. Hilton, R. P. Prasankumar, S. Fourmaux, A. Cavalleri, D. Brassard, M. A. El Khakani, J. C. Kieffer, A. J. Taylor, and R. D. Averitt, Phys. Rev. Lett. **99**, 226401 (2007), <http://link.aps.org/doi/10.1103/PhysRevLett.99.226401>.
- [141] L. A. L. de Almeida, G. S. Deep, A. M. N. Lima, and H. Neff, Appl. Phys. Lett. **77**, 4365 (2000), <http://aip.scitation.org/doi/10.1063/1.1334917>.
- [142] J. Shah, *Hot Carriers in Semiconductor Nanostructures: Physics and Applications* (Elsevier Science, 2012), ISBN 9780080925707, URL <https://books.google.com/books?id=XVC3W6yPwAkC>.
- [143] J. Michael Klopff and P. M. Norris, Int. J. Thermophys. **26**, 127 (2005), ISSN 1572-9567, <http://dx.doi.org/10.1007/s10765-005-2358-y>.
- [144] M. M. Qazilbash, Z. Q. Li, V. Podzorov, M. Brehm, F. Keilmann, B. G. Chae, H. T. Kim, and D. N. Basov, Appl. Phys. Lett. **92**, 241906 (2008), <http://aip.scitation.org/doi/pdf/10.1063/1.2939434>.
- [145] M. M. Qazilbash, M. Brehm, B.-G. Chae, P.-C. Ho, G. O. Andreev, B.-J. Kim, S. J. Yun, A. V. Balatsky, M. B. Maple, F. Keilmann, et al., Science **318**, 1750 (2007), ISSN 0036-8075, <http://science.sciencemag.org/content/318/5857/1750.full.pdf>.

- [146] T. Shiino, S. Shiba, N. Sakai, T. Yamakura, L. Jiang, Y. Uzawa, H. Maezawa, and S. Yamamoto, *Supercond. Sci. Technol.* **23**, 045004 (2010), <https://doi.org/10.1088/0953-2048/23/4/045004>.
- [147] V. N. Smolyaninova, C. Jensen, W. Zimmerman, J. C. Prestigiacomo, M. S. Osofsky, H. Kim, N. Bassim, Z. Xing, M. M. Qazilbash, and I. I. Smolyaninov, *Sci. Rep.* **6**, 34140 EP (2016), <http://dx.doi.org/10.1038/srep34140>.